A PARAMETRIC STUDY ON THE BOUNDING SURFACE SANICLAY MODEL FOR CYCLIC BEHAVIOUR OF KAOLIN CLAY

Kancharla Varun Choudary

A PARAMETRIC STUDY ON THE BOUNDING SURFACE SANICLAY MODEL FOR CYCLIC BEHAVIOUR OF KAOLIN CLAY

Kancharla Varun Choudary

in partial fulfilment of the requirements for the degree of

Master of Science

In Civil Engineering

at the Delft University of Technology,

to be defended publicly on 17th October, 2019 at 9:00 AM.

Student Number	:	4690397
Thesis committee	:	Prof. Dr. Ir. Cristina Jommi
		Dr. Ir. Federico Pisanò
		Dr. Ir. Anne-Catherine Dieudonné

Acknowledgement

This thesis marks the end of my masters journey in Delft university of Technology. In this research endeavor I have observed a steep learning curve that has led to an overall growth in me both personally and professionally.

The successful completion of my master's thesis would have not been complete without the support of my graduation committee. Firstly, I would like to thank my chair supervisor Dr. Cristina Jommi for her invaluable guidance throughout the conduction of this research. I would like to thank her from the bottom of my heart for allocating considerable amount of time from her busy schedule and patiently helping me tackle roadblocks I encountered during the course of this research work. Secondly, my sincere thanks to Dr. Federico Pisanò and Dr. Anne-Catherine Dieudonné for consistently guiding me in the right direction throughout my thesis.

My gratitude also extends to Haoyuan Liu (PhD student) and Ali Golchin (PhD student) for being kind enough to help me on various occasions in getting a broader understanding of the critical mechanisms of constitutive models.

My journey in Delft would be incomplete without mentioning my fellow geo-engineering graduates and friends who have been like a family away from home, constantly supporting me and being there for me whenever I needed them the most. Getting to be a part of global community has instilled a feeling of togetherness and taught me to tackle situations patiently amongst other things.

Finally, I would like to thank my parents for giving me the freedom to follow my dream to pursue masters in geotechnical-engineering. Their consistent love and support has been a driving force throughout my academic career.

K. Varun Choudary

Delft, October 2019

Abstract

Cyclic loading tends to affect the strength and stiffness parameters of soils, degrade its structure and results in accumulation of the excess pore water pressure. Such behaviour often leads to premature failure of the soils. Over the past few decades, geotechnical research community has developed numerous constitutive models to predict the behaviour of soils with variable degrees of success. The constitutive models based on the concept of bounding surface plasticity have gained much attention owing to the simplicity in describing the development of stiffness. This thesis analyzes the performance of bounding surface SANICALY model in reproducing the stress path and stress-strain behaviour of kaolin clay under undrained cyclic loading conditions .

A driver was developed in MATLAB for the chosen constitutive model to simulate undrained triaxial loading conditions. The performance of the driver was verified against the data published from literature. Further, sensitivity analysis was carried out on chosen model parameters. This was followed by validating the model with the experimental data on kaolin clay. Particularly, model performance was examined with varying initial conditions such as change of over-consolidation ratio, change of initial anisotropy, variation of initial pressure and strain controlled loading.

The obtained results from sensitivity analysis have shown to increase the strength and stiffness response of the model with increase in model parameters such as the rate of evolution of the anisotropy, bound for evolution of the anisotropy and change of initial stress-induced anisotropy. In the context of calibrating the model parameters against the experimental data, it was initially noticed that the experimental stress path in monotonic loading was not being reproduced by the model with various combinations of the initial parameters. Owing to such performance the model was subsequently assessed qualitatively. When the model is subjected to different initial loading conditions, certain aspects of the experimental behaviour were qualitatively captured by the model. These include faster rate of accumulation of pore water pressure with increase in the amplitude of cyclic loading, reduction in the rate of development of strains with increase in OCR values, increase in the hysteretic damping with increase in the amplitude of strains. However, with change of OCR there were differences in the development of stress path. Also contrasting results were observed with regard to the development of the stress-strain response with change of amplitude of cyclic loading and initial pressure.

Analyzing the model formulations revealed that the chosen model did not take into consideration the fabric anisotropy and hence it explains the deviation of the stress path from the experimental stress path in monotonic conditions. In the chosen model, during the process of cyclic loading, stagnation in the evolution of stress path is observed whenever the plastic volumetric strains stop evolving. It is recommended to incorporate plastic deviatoric strains in the evolution of the bounding surface in order to stimulate the further development of stress path even when the plastic volumetric strains stop evolving. It is also suggested to validate the model against different clays since this thesis focused only on Kaolin clay**.**

Contents

List of Figures

List of Tables

Chapter 1 : Introduction

Soils undergo cyclic loading in various scenarios, for example, traffic loading, earthquakes, wave forces on offshore structures, and machine vibrations, to name a few. Compared to static loading conditions, the repeated application of smaller loads for large number of cycles on soil tend to deteriorate the structure of the soils and lead to cyclic degradation. This makes the understanding of engineering behaviour of soils complex. Hence the behaviour of soils under the influence of cyclic loading conditions has gained the attention of the geotechnical community in the past few decades.

The primary cause of certain catastrophic failures in the past was the inadequate performance of clays under cyclic and dynamic loads. Examples of such failures include the September 1985 Mexico earthquake (Mendoza and Prince 1986), the landslide in clay soils after the 1964 Niigata earthquake (Morimoto et al. 1967), and the large seafloor slide off the Mississippi River delta during the passage of hurricane Camille (Bea et al. 1983). Due to the low permeability of clays, earthquake and wave loading tend to induce undrained cyclic shear loading. Such loading conditions tend to affect the strength and stiffness parameters, degrade the structure of the clay and facilitates the accumulation of the excess pore water pressure (Vucetic 1988). The behaviour of clays in particular is the focus of this thesis. Figure 1.1 shows an example of degradation of the strength of soil after it has been subjected to cyclic loading followed by monotonic loading (Li et al., 2011).

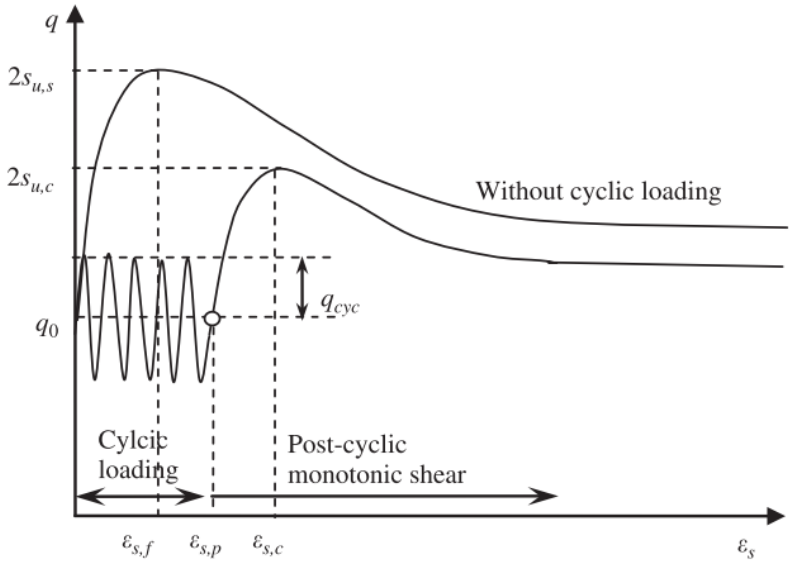

Figure 1.1 : Strength degradation of soils under the effect of cyclic loading (Li et al., 2011)

Behaviour of clays in general is also affected by anisotropy. The organization of particles in clay is termed as fabric. The orientation and arrangement of these particles depend upon the deposition and consequent consolidation of the deposits. The alignment of particles thus formed due to the aforementioned conditions is termed as inherent or fabric anisotropy. Once the soil undergoes plastic straining due to the influence of shear loading, the particles again tend to rearrange and induce a change in their alignment. This is called plastic strain induced anisotropy (Graham & Houlsby, 1983; Anandarajah & Kuganenthira, 1995; Lings et al., 2000; Wheeler et al., 2003; Karstunen & Koskinen, 2008).

Soil behaviour is numerically depicted using constitutive models. These models use the stress-strain relationships to describe soil behaviour. The ingredients of the constitutive modelling includes the definition of a yield surface which acts as the boundary for the development of elastic strains, a flow

rule to describe the development of plastic strains, a hardening rule to describe the change in the size of the yield surface to the plastic strains.

The first constitutive models developed to describe the clay behaviour under monotonic loading conditions were Cam-Clay model (Roscoe & Schofield, 1963), and modified Cam-Clay model (Roscoe, & Burland, 1968). These models work relatively well for monotonic loading conditions but have drawbacks in reproducing the behaviour of stress paths of soils under the cyclic loading conditions. Researchers developed on such shortcomings by improved definition of the development of shear strains inside the yield surface by introducing the concept of multiple surfaces (Mróz, 1967,1978; Prévost, 1977) and bounding surfaces (Dafalias & Popov, 1975; Dafalias, 1986; Gajo & Wood, 2001).

The concept of multiple surfaces have an intrinsic limitation in the definition of stiffness which is piecewise linear leading to a wrinkled evolution of stress-path. Bounding surface concept on the other hand improved upon such deficiencies by defining a continuous development of stiffness which gives a smoother evolution of stress path. The models developed (Liang & Ma 1992; Manzari & Nour 1997; Yu et al. 2007) within the scheme of bounding surface concept were able to reproduce the behaviour of clays with variable degree of success. However, these models have drawbacks in which the model response is either overdamped or elastic strains are developed during unloading phases. Taking these into consideration, Seidalinov (2012) enhanced the performance of bounding surface model by revising the development (definition) of stiffness with the evolution of the stress path. In this thesis, the model developed by Seidalinov (2012) is chosen for analysis.

The bounding surface SANICLAY (Simple ANIsotropic CLAY plasticity) model was developed by Seidalinov (2012) to reproduce the cyclic behaviour of clay. This model was validated for three different types of clays under cyclic loading conditions. However these validations did not take into consideration certain aspects of the clay behaviour such as the initial overconsolidation ratio (OCR), initial anisotropy of the clay. The behaviour of the model in these initial conditions is not clearly understood and has not been investigated in detail. Thus, there is a need for checking the extension of this model for its robust performance on different initial conditions of the clay. In this thesis, the bounding surface SANICLAY model developed by Seidalinov (2012) is validated against the experimental results reported in literature on Kaolin clay Wichtmann (2018). The Kaolin database Wichtmann (2018) was used to calibrate the model constants needed for the bounding surface SANICLAY model.

1.1 Research questions

- Can the bounding surface SANICLAY model demonstrate the behaviour of clay with initial anisotropy?
- How effective is the bounding surface SANICLAY model in reproducing the stress-path and stress strain response of soils under higher over consolidation ratio's (OCR) ?
- Can the model accurately predict the damping behaviour of the clays with different magnitude of strains?

1.2 Structure of thesis

In the context of achieving the aforementioned goals, the sequential approach has been followed.

Chapter 2 gives the brief review of current state of art from experimental observations and constitutive models.

Chapter 3 discusses the detailed formulations concerning the bounding surface SANICLAY model.

Chapter 4 conveys the strategy used in implementation of model in MATLAB, verification of the implemented code with the results published in Seidalinov (2012,2013) and performing sensitivity analysis on chosen model parameters.

Chapter 5 presents the validation of the model against the experimental results from kaolin database (Wichtmann 2018).

Chapter 6 reviews on the results obtained from the validation and gives the conclusions thus obtained. Further some recommendations are proposed for future work.

Chapter 2 : Literature review

Literature review in this thesis is subdivided into two parts. First part concerns a brief review on the behaviour of soft clays, specifically under the influence of cyclic loading. The parameters influencing their behaviour and the properties being affected due to them. The second part of literature review focuses on the general form of constitutive models. Wherein a brief description of elastoplastic models is followed by the background theory on bounding surface modelling.

2.1 Behaviour of clay under cyclic loading

Clays in their in-situ state are found to be less permeable in nature. This property facilitates an undrained behaviour in clays. Undrained behaviour tend to occur when the rate of applied loading is much higher than the rate of dissipation of the excess pore water pressure present in the clay. This in turn leads to development of pore pressures and necessitates an effective stress analysis. In case of an undrained analysis the total volume of the clay remains unchanged which means that the total change in volumetric strains is zero.

Numerous experimental studies have been carried out for studying the behaviour of clay under cyclic loading. The studies suggest several parameters namely: Over Consolidation Ratio (OCR), initial stress, Cyclic stress Ratio (CSR), frequency of loading, structure of the clay, anisotropy etc. and their influence on strength and stiffness properties of the clays, pore water pressure accumulation, stress path and stress-strain response of the clays (Idriss et al., 1978; Wilson & Greenwood; 1974; Andersen et al., 1980; Hyde & Ward, 1986; Lefebvre & LeBoeuf, 1987; Dobry & Vucetic, 1987; Vucetic & Dobry, 1988,1991; Ohara & Matsuda, 1988; Azzouz et al., 1989; Yasuhara et al., 1992; Zergoun & Vaid, 1994; Hyodo et al., 1994; Zhou and Gong, 2001; Boulanger & Idriss, 2006; Okur & Ansal, 2007; Li et al., 2011; Mortezaie and Vucetic, 2013). The influencing parameters and properties relevant to the thesis are discussed in the following sections.

2.1.1 Strength and stiffness

Cyclic loading of clays leads to development and significant accumulation of pore water pressure, resulting in degradation of the structure of clay which leads to decrease in the strength and stiffness of the clays (Idriss et al., 1978; Lefebvre, G., & LeBoeuf, D. ,1987; Vucetic and Dobry, 1988,1991; Kagawa, 1992; Zergoun & Vaid, 1994; Zhou and Gong, 2001, Okur & Ansal, 2007).

Vucetic & Dobry, (1991) studied about the importance of plasticity index on the behaviour of cyclic response of clays. They concluded that degradation of the shear modulus is higher with decrease in the plasticity index and that the clay exhibits a linear cyclic stress-strain response at higher plasticity. Also as seen from figure below (Figure 2.1, (a)), with the increase in number of loading cycles, degradation of shear modulus is increasing. Figure 2.1, (b) reveals the degradation of shear strength of the Broadback clay(Lefebvre, G., & LeBoeuf, D., 1987) with increase in the number of loading cycles.

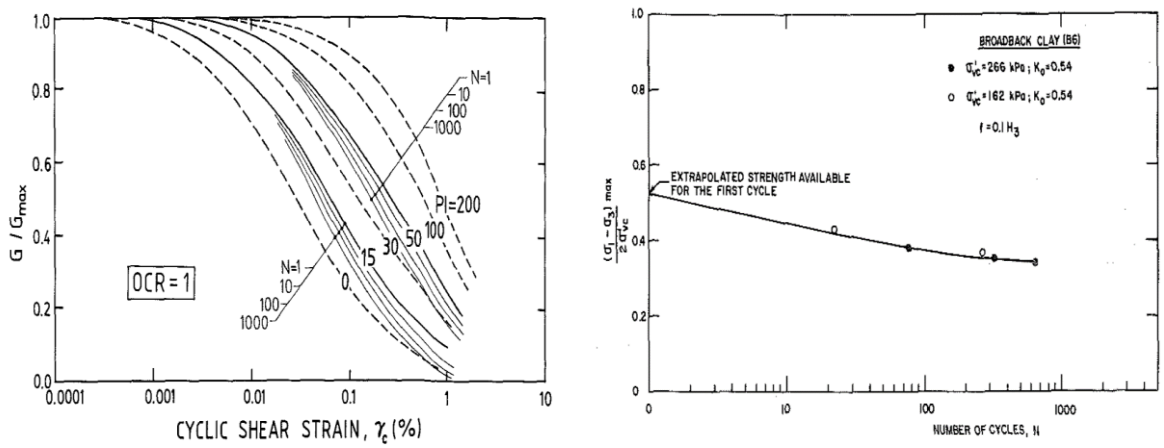

Figure 2.1 : (a) Stiffness degradation with cyclic shear strain as a function of plasticity index and number of loading cycles. (Vucetic & Dobry, 1991), (b) Strength degradation with increase in number is cycles of loading. (Lefebvre & LeBoeuf ,1987)

Reduction in strength after cyclic loading is greater in the case of normally consolidated clays than that of the over consolidated clays as reported by Hyde & Ward, (1986). The authors pointed out that the initially heavily over consolidated clays did not generate considerable changes in pore water pressures which thus resulted in less variation of the post cyclic monotonic strength. With the increase in the amplitude of cyclic loading, the undrained shear strength reduces (Yashuara et. al., 1992).

2.1.2 Cyclic softening

The significant loss of strength and strains in clays under the influence of cyclic loading is called cyclic softening (Boulanger & Idriss, 2006). At small strain ranges, Li et al., (2011) reported an increase in the degree of strain softening with increase in the amplitude of cyclic stress and number of cycles of loading which is accounted to the increasing destructuration and evolution of anisotropy during the process of cyclic loading. The reduction of the peak strength depends on the accumulative behaviour induced by the cyclic loads. Mortezaie and Vucetic, (2013) reported that the higher rate of softening is due to higher reduction of pore water pressure which leads to considerable decrement of the effective stress.

2.1.3 Pore Water Pressure (PWP) and shear strains

Cyclic loading could lead to clay failure as a result of excess pore pressure and cyclic-induced shear strain developments (Andersen et al., 1980; Yasuhara et al., 1992; Zhou and Gong, 2001). In normally consolidated clays under undrained cyclic loading conditions, due to the contractive nature of the clays, pore water pressure tends to increase (positive value) with the increasing level of shear strain. In the case of over consolidated clays, negative PWP builds up at the beginning of the test which tends to reverse its sign with the increase in the amount of cyclic straining. The response in over consolidated clays is attributed to the greater number of interparticle bonds and repulsive forces present in the clay. At the beginning of the cycling, these bonds are broken and the repulsive force cause a tendency for volume increase and development of negative PWP (Dobry and Vucetic 1987; Vucetic 1988; Ohara and Matsuda 1988).

Wilson & Greenwood, (1975) made observations into the development of recoverable (elastic) and irrecoverable (plastic) components of PWP and shear strains with increase in load cycles. They attributed the plastic components to the plastic deformation of the soil grain structure which can occur due to loss of contact between the soil grains under the influence of stress. One more noteworthy point is that the elastic components of PWP and shear strains tend to remain almost constant unlike plastic components which tend to increase with the loading cycles.

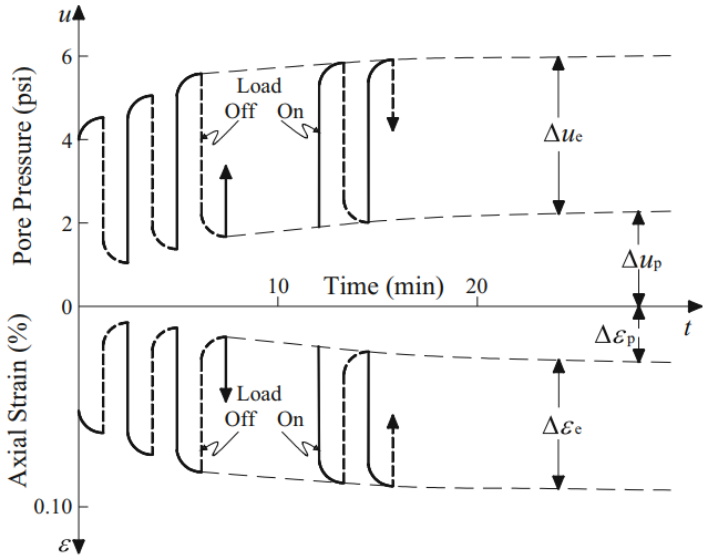

Figure 2.2 : Pore water pressure and strains generated over time by repeated loading (Wilson & Greenwood, 1975; taken from Yang, 2017)

At a lower frequency of loading, for a given number of cycles of loading, larger development of shear strains and pore water pressure was reported (Li et al., 2011; Mortezaie and Vucetic, 2013). Mortezaie and Vucetic, (2013) made an interesting observation with regard to the higher frequency of loading wherein higher frequency of loading causes larger deformation and smaller pore water pressures which is counterintuitive in nature, since smaller pore water pressure implies higher effective stress and a stiffer soil. Therefore, this trend indicates that the buildup of cyclic pore water pressure may not be a dominant contributor to cyclic degradation normal consolidated clay. One other similar counterintuitive feature reported by researchers says that in case of over consolidated clays with higher plasticity, despite a decrease in pore water pressure and increase of effective stress with the number of cycles, a significant cyclic degradation takes place (Andersen et al. 1980; Vucetic 1988). In terms of cyclic stress ratio, experimental observations by Zhou & Gong, (2001) revealed the degradation of pore water pressure and strain with decrease in cyclic stress ratio (Figure 2.3).

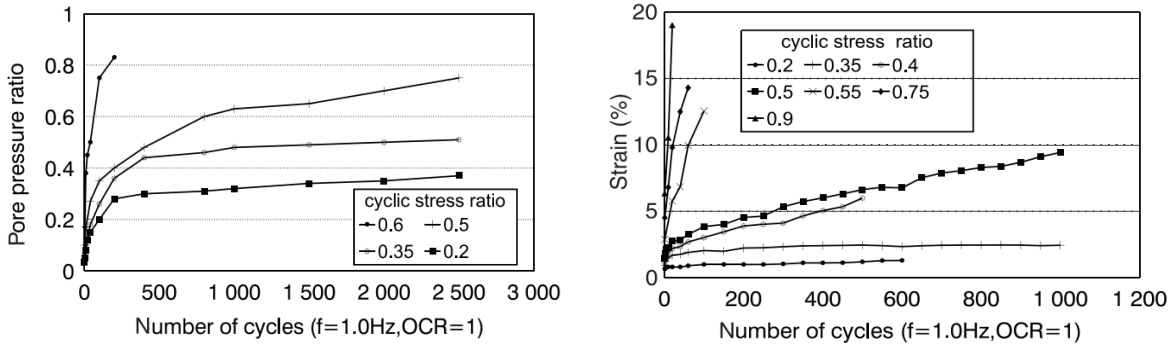

Figure 2.3 : (a) pore water pressure and (b) strain accumulation of clays with increase in number of loading cycles for varying values of cyclic stress ratio. (Zhou & Gong, 2001)

2.1.4 Stress path and stress strain response

The stress-strain response is relatively linear at small cyclic strains which is majorly controlled by the maximum value of shear modulus. While at large cyclic strains a significant amount of non-linearity, inelasticity, damping and degradation was observed (Dobry and Vucetic, 1987).

In the case of normally consolidated clays, effective stress reduces due to the generation of positive excess pore water pressures. The decrease in the effective stress is faster at the initial cycles of loading,

but with the increase in loading cycles, the effective stress path progresses slowly towards the origin. Failure occurs when the migrated effective stress path traces a steady loop in the vicinity of the failure envelopes. (Azzouz et al., 1989; Hyodo et al., 1994; Zergoun & Vaid, 1994). In the case of overconsolidated clays, in the initial cycles of loading, the developed excess pore pressures are negative meaning that the effective stress path migrates away from the origin, this effect is more vibrant in case of higher OCRs. But with increase in the cycles of loading, the pore water pressure reverses its sign and results in the failure of the soil (Azzouz et al., 1989).

As the cyclic stress ratio (CSR) increases, the failure of the soil occurs at a faster pace which is indicated by the number of cycles of loading leading to failure. This condition holds good even for the over consolidated clays where with increase in the CSR values, lesser number of cycles of loading were required to bring the clay to failure (Azzouz et al., 1989).

In terms of frequency of loading, Zergoun & Vaid (1994) reported that unreliable pore water pressures are measured during high frequency[1] of loading. They also stated that reliable measurement of pore water pressures is only possible by adapting slow undrained cyclic shear tests.

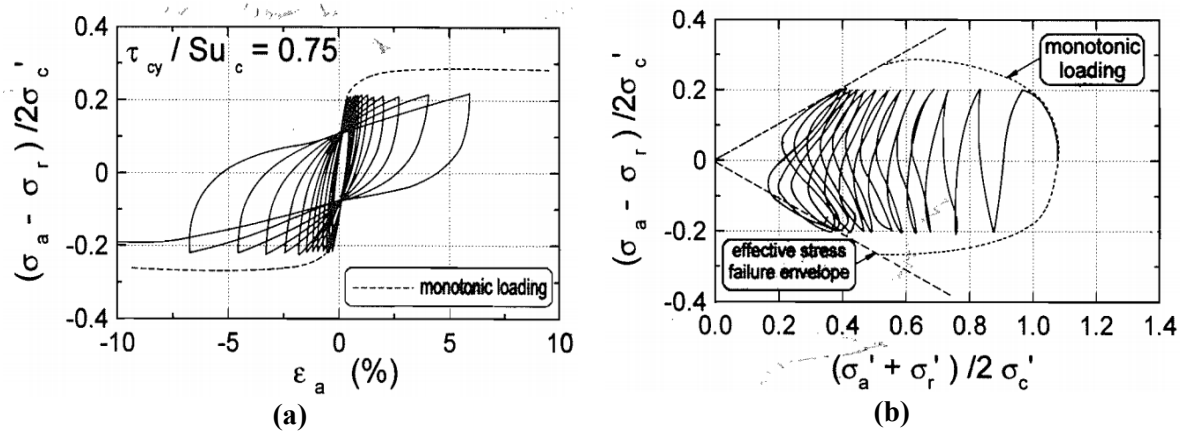

Figure 2.4 : (a) stress-strain response and (b) stress path comparison of monotonic versus cyclic loading tests for Cloverdale clay (Zergoun & Vaid, 1994)

2.2 Review of the constitutive models

Constitutive modelling is a numerical way to represent the behavior of soils by linking the change in stress to the change in strain. A brief overview of the elasto-plastic models followed by the need and development of bounding surface models are outlined in this section.

2.2.1 Elasto-plastic models

In soil mechanics generally the total strain increments are subdivided into elastic (recoverable) and plastic (irrecoverable) strain increments represented by,

$$\dot{\varepsilon} = \dot{\varepsilon}^e + \dot{\varepsilon}^p \tag{2.1}$$

where ε stands for strain, the superscript ‘e’ means elastic and superscript ‘p’ means plastic. Dot above the quantities represents increment in the values.

If the stress-strain curve is able to retrace back the same path during unloading then the response of the soil is considered to be elastic. Whereas if the stress-strain curve follows a completely different path during unloading then this leads to an elasto-plastic response where irrecoverable plastic strains are accumulated within the material. A simple illustration of the aforementioned theory is illustrated in Figure 2.5,

[1] In their research(Zergoun & Vaid, 1994), strain rate greater than 0.5% per hour are considered as fast cyclic tests..

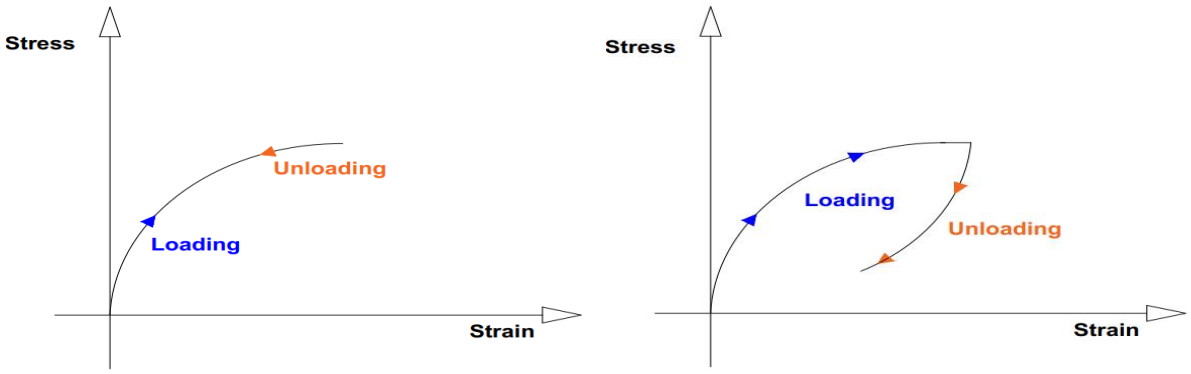

(a) (b)

Figure 2.5 : stress strain behaviour (a) elastic response, (b) elasto-plastic response (Brinkgreve, 2017).

Elastic relations : The general constitutive relation between the stress and strain increments can be represented as follows,

$$\dot{\sigma} = D^e \dot{\varepsilon}^e$$
$$\dot{\varepsilon}^e = C^e \dot{\sigma} \tag{2.2}$$

where $\dot{\sigma}$ is the stress increment, $\dot{\varepsilon}^e$ is the elastic strain increment, D^e is the elastic stiffness matrix and C^e is the elastic compliance matrix.

Yield function : Yield function is the function of the current stress state (σ) and the internal hardening variables (χ). The loci of the stress points from the yield function gives rise to yield surface. In the elasto-plastic models, yield surface defines the boundary for the elastic region.

$$f(\sigma, \chi) = 0 \tag{2.3}$$

Consistency condition : Consistency condition states that when the stress state is on the yield surface and continues to remain on the yield surface, plastic strains are produced. When the stress state is inside the yield surface, pure elastic strains are produced. It is impossible for the stress state to lie outside the yield surface.

$f < 0$,	Pure elastic behaviour	
$f = 0$ & $df < 0$,	Unloading from a plastic state (= elastic behaviour)	(2.4)
$f = 0$ & $df = 0$,	Elasto-plastic behaviour	

A graphical representation of the yield surface is shown in Figure 2.6.

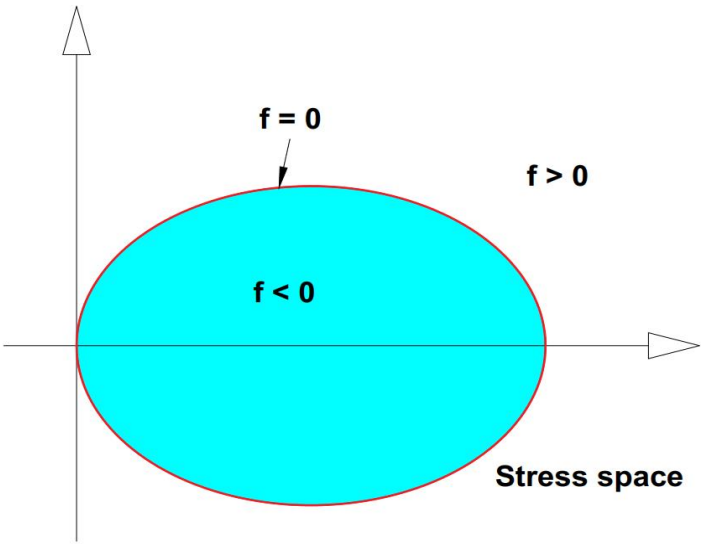

Figure 2.6 : Yield surface in the stress space.

Plastic potential function and flow rule : In order to compute the plastic strains at the current stress state on the yield surface, it is assumed that there exists a plastic potential function (Wood, 1991) which passes though the current stress state.

$$g(\sigma,\chi)=0 \tag{2.5}$$

Where g is the plastic potential function.

Flow rule on the other hand is a stress-dilatancy relationship which defines the rate of plastic deformations as,

$$\dot{\varepsilon}^p = \langle L \rangle \frac{\partial g}{\partial \sigma}, \quad \psi = \frac{\dot{\varepsilon}_v^p}{\dot{\varepsilon}_q^p} \tag{2.6}$$

where ψ is the dilatancy of the soil, σ is the current stress state, superscript 'p' means plastic, subscript 'v' means volumetric strain, subscript 'q' means deviatoric strain and L is the plastic multiplier or loading index. L is enclosed in Macauley brackets $\langle\ \rangle$ which render, $\langle L \rangle = L$ when $L > 0$ representing plastic loading and $\langle L \rangle = 0$ when $L \leq 0$ representing elastic unloading.

Magnitude of L gives the magnitude of the plastic strains and the gradient of the plastic potential with respect to the current stress state gives the direction of the plastic strains. In the definition of the flow rule, if the plastic potential is represented by the same function as the yield function, it is called as the associated flow rule and when the plastic potential takes a different form than the yield function then it is called as the non-associated flow rule.

$$\begin{aligned} f &= g, \quad \text{Associated flow rule} \\ f &\neq g, \quad Non-associated\ \text{flow rule} \end{aligned} \tag{2.7}$$

Hardening rule : It links the change in size of the yield surface with the magnitude of the plastic strains, i.e., a link between the internal hardening parameter (χ) and the loading index (L). To achieve this, consistency condition is used which takes the form as follows,

$$\frac{\partial f}{\partial \sigma}^T \dot{\sigma} + \frac{\partial f}{\partial \chi}^T \dot{\chi} = 0 \tag{2.8}$$

The internal hardening parameter is a function of the plastic strains. By substituting this idea in equation (8) leads to,

$$\frac{\partial f}{\partial \sigma}^T \dot{\sigma} + L \frac{\partial f}{\partial \chi}^T \frac{\partial \chi}{\partial \varepsilon^p} \frac{\partial g}{\partial \sigma} = 0 \tag{2.9}$$

By substituting equations (2.1),(2.2) and (2.6) into equation (2.9), loading index is obtained as,

$$L = \frac{\frac{\partial f}{\partial \sigma}^T D^e}{\frac{\partial f}{\partial \sigma} D^e \frac{\partial g}{\partial \sigma} + K_p} \dot{\varepsilon},\ K_p = -\frac{\partial f}{\partial \chi}^T \frac{\partial \chi}{\partial \varepsilon^p} \frac{\partial g}{\partial \sigma} \tag{2.10}$$

where K_p is called as the plastic modulus.

The constitutive equation in (2.2) can be reformulated by substituting the values of the loading index and plastic strains as follows,

$$\dot{\sigma} = \left[D^e - \frac{D^e \frac{\partial g}{\partial \sigma} \frac{\partial f}{\partial \sigma}^T D^e}{\frac{\partial f}{\partial \sigma}^T D^e \frac{\partial g}{\partial \sigma} + K_p} \right] \dot{\varepsilon} \tag{2.11}$$

where the elasto-plastic stiffness matrix can be represented as,

$$D^{ep} = D^e - \frac{D^e \frac{\partial g}{\partial \sigma} \frac{\partial f}{\partial \sigma}^T D^e}{\frac{\partial f}{\partial \sigma}^T D^e \frac{\partial g}{\partial \sigma} + K_p} \tag{2.12}$$

2.2.2 Existing elasto-plastic models and the emergence of bounding surface models

Before looking at the review of the constitutive models, it is important to reflect on a couple of important features of cyclic loading of clays from section 2.1 which are deemed important in the coming paragraphs. In the experimental observations reviewed in section 2.1, it was observed that under the influence of cyclic loading, PWP and the axial strains get accumulated with the increasing number of loading cycles. It has also been observed (reported) that thus accumulated values can be a combination of both elastic (recoverable) and plastic (irrecoverable) components. This plastic PWP leads to reduction of the effective volumetric stress with the loading-unloading-reloading cycles.

Critical state soil mechanics theory (Roscoe and Poorooshasb, 1963; Roscoe et al., 1963, 1958) is the base for the development of most of the constitutive models for soils. It states that plastic strains are associated with the reduction of mean effective stress (volumetric stress). Classical elasto-plastic models developed in the past such as Cam-Clay model (Roscoe & Schofield 1963), modified Cam-Clay model (Roscoe & Burland 1968), Soft-soil model (Brinkgreve & Vermeer 1997), Soft-soil creep model (Vermeer & Neher 1999), Hardening soil model (Schanz et al.1999) work relatively well in describing most features of the behaviour of clays in the monotonic loading conditions. However, these models have a major limitation in capturing the accumulative behaviour of stresses and strains in cyclic loading. The response in the unloading and reloading phases are effectively elastic in nature using the aforementioned models which implies that there is no evolution of volumetric stress. This results in no plastic strains generated during the unloading and reloading phases.

The necessity to model plastic strains during the course of unloading/reloading cycles led to the development of multi surface and bounding surface plasticity models. Multi surface plasticity models were first developed for metals based on the kinematic hardening rule (Iwan 1967; Mróz 1967). This theory was further extended to soils by Prévost, (1977). Basic concept behind the multi surface models is the enclosure of surfaces with constant stiffness. Any stress state inside the inner most surface renders purely elastic strains while the outer most surface acts as the conventional yield surface. In here a piecewise linear decrement in stiffness is encountered by the stress path be it loading/ unloading/ reloading. During the case of stress reversals there is a sudden increase in the stiffness. Introduction of the multiple surfaces with varying stiffness levels permits the development of plastic strains inside the yield surface. Figure 2.7 gives an impression of the multi surface concept where f_0, f_1 … f_p represent the nested yield surfaces in the stress space with sizes $k^{(0)} < k^{(1)} \ldots .< k^{(p)}$ defining the fields of constant shear modulus. The so defined yield surfaces are allowed to translate and change in size simultaneously but are not allowed to cross each other. These models have limitations in the sense that the so defined plastic modulus is piecewise linear, the numerical modelling of such models require ample memory to store the data pertaining to the sub-yield surfaces.

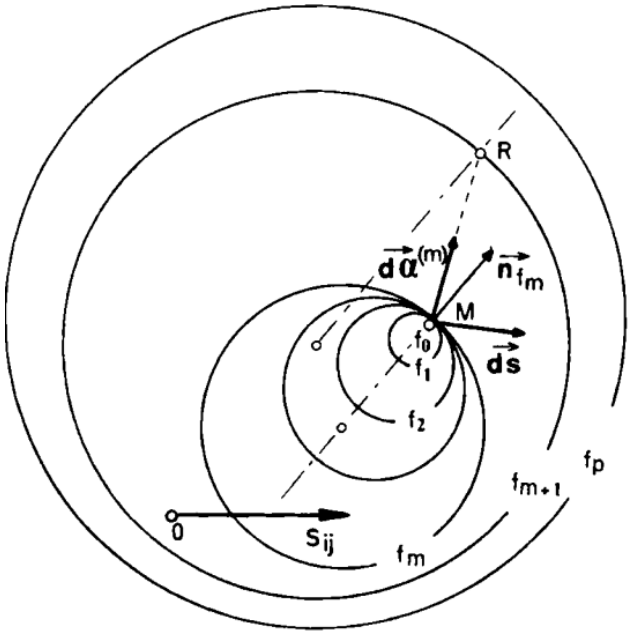

Figure 2.7 : Multi surface concept in stress space (Prévost 1977).

Bounding surface models on the other hand were also initially developed for metals based on kinematic hardening rule (Dafalias & Popov 1975; Krieg 1975). These models have been extended to soils by Dafalias (II,III) (1986). The main component of the bounding surface plasticity is the concept of a surface that encompasses all the possible stress states within the stress space. The plastic modulus is

defined based on the distance between the current stress point inside the bounding surface and its corresponding image on the bounding surface. Unlike multi surface models as discussed in the previous paragraph, bounding surface models adopt a smooth transition of the stiffness with the evolution of the stress path.

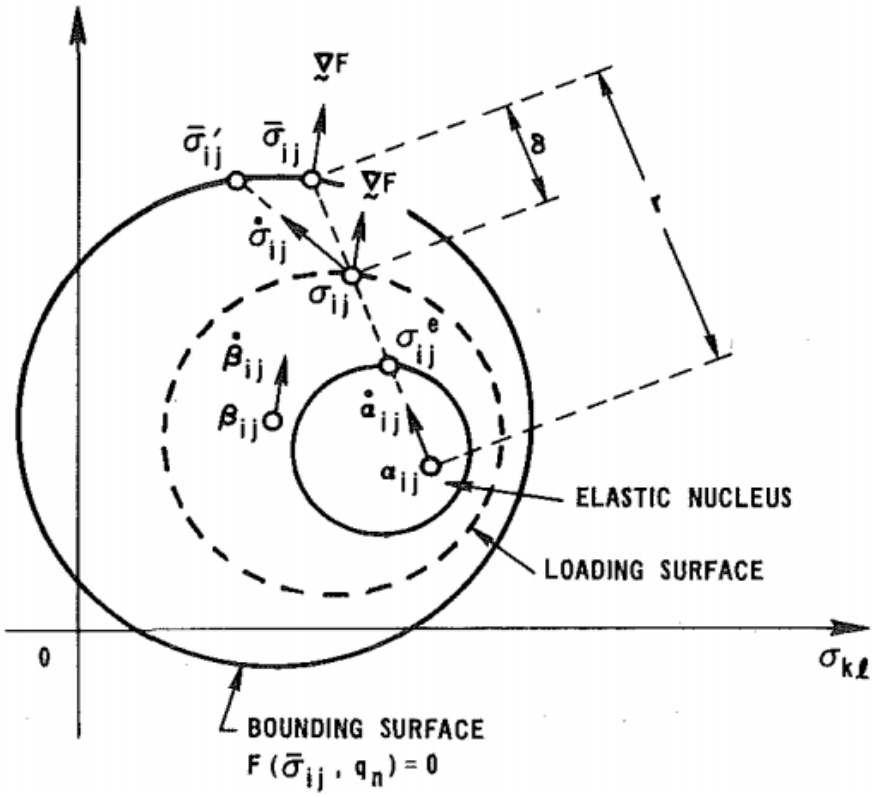

Figure 2.8 : Bounding surface representation in stress space (Dafalias(II), 1986)

Figure 2.8 gives a graphical representation of the bounding surface model in the stress space. In terms of constitutive relations, basic formulations of the yield surface as defined in section 2.2.1 still hold good for the bounding surface except for the change in plastic modulus formulations to account plastic strains. Loading surface (f = 0) is enclosed inside the bounding surface (F = 0) and is representative of the current stress state (σ). Image stress is calculated with the help of a mapping rule based upon the current stress state. The features of BS concept which facilitate the development of plastic strains inside the bounding surface are as follows,

- A well-defined mapping rule to define an image stress ($\bar{\sigma}$) for any stress state inside the BS. And $\partial f / \partial \sigma = \partial F / \partial \bar{\sigma}$ where $\partial f / \partial \sigma$ and $\partial F / \partial \bar{\sigma}$ are the gradients of loading and bounding surface respectively, for $\sigma = \bar{\sigma}$ to guarantee that the loading surface never intersects the BS. Mapping rule is non invertible such that image stress must not correspond to infinite values of stresses inside the bounding surface at the same time.
- To facilitate the development of plastic strains inside the BS, image stress must lie on the BS and the plastic modulus for a given image stress is found through the consistency condition $\dot{F} = 0$ as,

$$\bar{K}_p = -\frac{\partial F}{\partial \bar{\chi}}^T \dot{\bar{\chi}} \tag{2.13}$$

- Plastic modulus at the current stress state is related to the BS plastic modulus through a Euclidian distance:

$$\delta = \left[(\bar{\sigma} - \sigma)(\bar{\sigma} - \sigma) \right]^{1/2} \tag{2.14}$$

such that $K_p > \bar{K}_p$ for $\delta > 0$ and $K_p = \bar{K}_p$ for $\delta = 0$.

In the bounding surface framework, various models (Liang & Ma 1992; Manzari & Nour 1997; Yu et al. 2007) have been developed and implemented with variable degree of success. These models however have drawbacks wherein the response of the models are either overdamped or was developing elastic strains during unloading phases as seen in Figure 2.9.

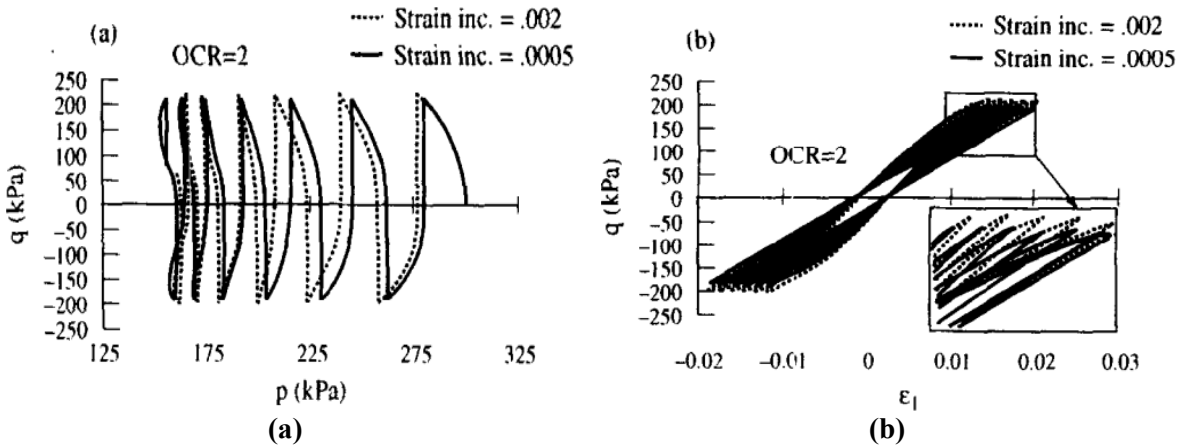

Figure 2.9 : Simulations of undrained cyclic triaxial tests with two different strain increments (Manzari & Nour 1997)

The bounding surface SANICLAY model developed by Seidalinov (2012) abated few of these shortcomings. Seidalinov (2012) identified the reason behind the shortcomings as the way in which the projection center[2] is defined in the previous models. Previous models either considered the projection center to be fixed at the origin or to be moving along the rotational variable[3] 'α'. Seidalinov (2012) defined a moving projection center which has a dual way of evolution. Firstly to maintain the relative position of projection center with evolving bounding surface, the projection center evolves with the stress path. Secondly it gets updated to the present stress state during the load reversals, this kind of updating resolves the problem of overdamping in the response of the model. Along with that a new damage parameter has been introduced to account for reduction of stiffness to simulate cyclic softening behaviour as observed in the experimental observations.

2.3 Summary

The first part of this chapter gave an overview of the experimental observations on the behaviour of clays under the influence of cyclic loading. Experimental evidence from the literature have shown the strength and stiffness degradation of the soils with increase in the number of cycles of loading which was accounted to degradation of the structure of the clay and accumulation of pore water pressure. The second part of this chapter discussed about the evolution of constitutive models leading to bounding surface modelling. Classical elasto-plastic models produced pure elastic stains within the yield surface which did not give a realistic representation of the observed experimental data. Bounding surface models allowed for the development of elasto-plastic strains within the bounding surface by defining a stiffness dependent upon the current stress state.

[2] Projection center is the point through which the current stress state is projected onto the bounding surface.
[3] will be explained in Chapter 3

Chapter 3 : Overview of bounding surface SANICLAY model

The constitutive equations related to the bounding surface SANICLAY(Simple ANIsotropic CLAY plasticity) model have been adopted from Seidalinov (2012). The stress and strain quantities used hereafter have the following notations,

$$p=\frac{1}{3}\left(\sigma_a+2\sigma_r\right), \qquad q=\left(\sigma_a-\sigma_r\right) \tag{3.1}$$

$$\varepsilon_v=\left(\varepsilon_a+2\varepsilon_r\right), \qquad \varepsilon_q=\frac{2}{3}\left(\varepsilon_a-\varepsilon_r\right) \tag{3.2}$$

Where p is the mean stress and q is the deviatoric stress. The subscripts a and r mean axial and radial directions, v and q mean the volumetric and the deviatoric components. The following sections detail the formulations of the bounding surface SANICLAY model in the triaxial space.

3.1 Elastic relations

The total rate of strains is decomposed into the elastic and plastic components as $\dot{\varepsilon}=\dot{\varepsilon}^e+\dot{\varepsilon}^p$. The calculation of elastic components of strains is based on the isotropic hypoelastic relations as shown in equation (3.3).

$$\dot{\varepsilon}_v^e=\frac{\dot{p}}{K}, \qquad \dot{\varepsilon}_p^e=\frac{\dot{q}}{3G} \tag{3.3}$$

K and G in the above equation represent the bulk and the shear moduli[4] which are expressed as

$$K=\frac{p\left(1+e\right)}{\kappa}, \quad G=\frac{3K\left(1-2\nu\right)}{2\left(1+\nu\right)} \tag{3.4}$$

Where e is the void ratio, κ is the slope of unloading-reloading line in the e-ln p space, ν is the Poisson's ratio.

3.2 Flow rule and plastic potential

Flow rule defines the volumetric and deviatoric components of strains as follows,

$$\dot{\varepsilon}_v^p=\left\langle L\right\rangle\frac{\partial g}{\partial \bar{p}}, \quad \dot{\varepsilon}_q^p=\left\langle L\right\rangle\frac{\partial g}{\partial \bar{q}} \tag{3.5}$$

where $\bar{p}$ and $\bar{q}$ are the volumetric and deviatoric components of the image stress on the bounding surface which shall be explained in section 3.3.

It is required that the plastic potential which is used for calculation of the plastic strains must pass through the image stress and is given by equation (3.6),

[4] The formulation for shear modulus is misprinted in Seidalinov (2012) where instead of (1-2ν) in the numerator of the shear modulus formulation (1+e) has been printed.

$$g=\left(\bar{q}-\bar{p}\alpha\right)^2-\left(M^2-\alpha^2\right)\bar{p}\left(p_\alpha-\bar{p}\right)=0 \tag{3.6}$$

Where M is the critical stress ratio, α represents the rotational hardening to be discussed in subsequent sections and p_α is the value of $\bar{p}$ at $\bar{q} = \bar{p}\alpha$. The critical stress ratio M = M_c when the image stress ratio $\bar{\eta}= \bar{q}/\bar{p} >= \alpha$ and M = M_e when the image stress ratio $\bar{\eta}= \bar{q}/\bar{p} < \alpha$. For real valued image stresses, M > α. M_c and M_e are the critical state ratios in compression and extension respectively. By substituting the value of equation (3.6) into equation (3.5), the flow rule is given by,

$$\dot{\varepsilon}_v^p=\langle L\rangle\bar{p}\left(M^2-\bar{\eta}^2\right), \qquad \dot{\varepsilon}_q^p=\langle L\rangle 2\bar{p}\left(\bar{\eta}-\alpha\right) \tag{3.7}$$

A noteworthy point would be that there will be no increment in plastic volumetric strains when $\bar{\eta} = M$ and no plastic deviatoric strains produced when $\bar{\eta} = \alpha$.

3.3 Image stress and bounding surface

The bounding surface equation is given by:

$$F=\left(\bar{q}-\bar{p}\alpha\right)^2-\left(N^2-\alpha^2\right)\bar{p}\left(p_0-\bar{p}\right)=0 \tag{3.8}$$

where p_0 is the isotropic or volumetric hardening and controls the size of the bounding surface and α is a non-dimensional rotational hardening variable accounting for anisotropy. N is the peak stress ratio on the bounding surface and serves as a bound for the evolution of the rotational variable α, it is assumed to have the same value in both compression and extension. $(\bar{p},\bar{q})$ are the image stresses on the bounding surface. For real valued image stresses, N > α. A representation of the bounding surface in triaxial space is given in Figure 3.1.

The loci of the current stresses (p,q) form a loading surface f =0, which is analogous to the bounding surface with the center of the homology as the projection center (PC). Analytical expression of the loading surface need not be defined explicitly as all the formulations that follow depend upon the image of the current stress on the bounding surface which is explained in the following paragraphs.

The bounding surface theory postulates that for any stress state (p,q), there exists a unique image stress $(\bar{p},\bar{q})$ lying on the bounding surface. The image stress is obtained by radially mapping the current stress (p,q) from a PC (p_c,q_c) onto the bounding surface as shown in Figure 3.1.

For a given PC and the current stress state (p,q), the image stress is defined as,

$$\bar{p}=p_c+b\left(p-p_c\right), \qquad \bar{q}=q_c+b\left(q-q_c\right) \tag{3.9}$$

Where b is the similarity ratio between the loading surface f = 0 and the bounding surface F = 0. The value of the similarity ratio is obtained by substituting the equation (3.9) in equation (3.8).

$$\left(\bar{q}-\bar{p}\alpha\right)^2-\left(N^2-\alpha^2\right)\bar{p}\left(p_0-\bar{p}\right)=Ab^2+Bb+C=0 \tag{3.10}$$

To simplify the calculations, equation (3.10) is solved in parts as follows,

$$\left(\bar{q}-\bar{p}\alpha\right)^2 = A_1 b^2 + B_1 b + C_1 = 0 \tag{3.11}$$

where[5],

$$\begin{aligned} A_1 &= \left[\left(q-\alpha p\right)-\left(q_c-\alpha p_c\right)\right]^2 \\ B_1 &= 2\left[\left(q-\alpha p\right)-\left(q_c-\alpha p_c\right)\right]\left(q_c-\alpha p_c\right) \\ C_1 &= \left(q_c-\alpha p_c\right)^2 \end{aligned} \tag{3.12}$$

and on the similar grounds,

$$\bar{p}\left(p_0-\bar{p}\right) = A_2 b^2 + B_2 b + C_2 = 0 \tag{3.13}$$

where,

$$\begin{aligned} A_2 &= (p-p_c)^2 \\ B_2 &= (2p_c-p_0)(p-p_c) \\ C_2 &= p_c(p_c-p_0) \end{aligned} \tag{3.14}$$

Substituting equations (3.12) and (3.14)into equation (3.10) gives rise to,

$$\begin{aligned} A &= \frac{A_1}{\left(N^2-\alpha^2\right)} + A_2 \\ B &= \frac{B_1}{\left(N^2-\alpha^2\right)} + B_2 \\ C &= \frac{C_1}{\left(N^2-\alpha^2\right)} + C_2 \end{aligned} \tag{3.15}$$

The value of the similarity ratio is given by the positive root of the above expression which is further used for computing the image stress. The value of b varies from one to infinity, where one represents that the current stress state is on the bounding surface and infinity represents that the stress state is within the elastic nucleus.

[5] The equation for B_1 has been misprinted in Seidalinov (2012) where an additional q has been multiplied to the B_1 as opposed to (3.12). A detailed elaboration and explanation of the same has been provided in Appendix I.

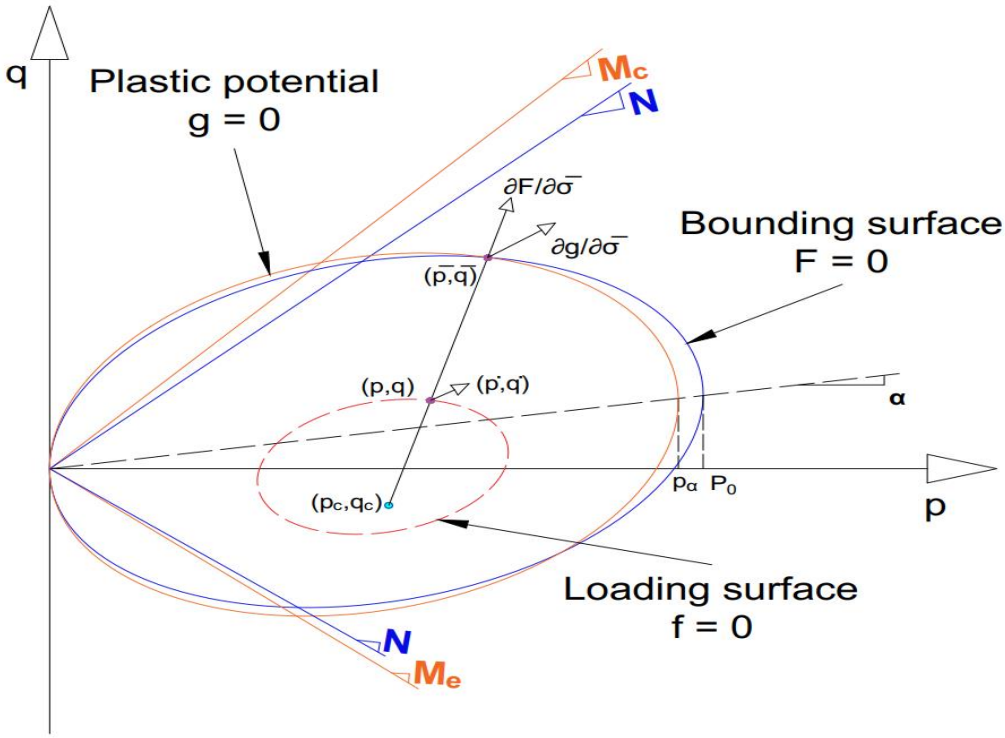

Figure 3.1 : Bounding surface SANICLAY model in the triaxial space.

3.4 Evolution of the hardening variables p_0 and α

The evolution of p_o is given by,

$$\dot{p}_0 = \langle L \rangle \overline{p_0} \tag{3.16}$$

Where $\bar{p}_0$ is defined to account for the destructuration mechanism as,

$$\overline{p_0} = S_i \overline{p_{0d}} + \overline{S_i} p_{0d} \tag{3.17}$$

Where p_{0d} is the destructured value of p_0 and is given by p_0/S_i, where $S_i \geq 1$ is the isotropic structuration factor.

p_{0d} and S_i are given by,

$$\overline{p_{0d}} = \left(\frac{1+e}{\lambda-\kappa}\right) p_{0d} \left(\frac{\partial g}{\partial \bar{p}}\right) \tag{3.18}$$

$$\overline{S_i} = \kappa_i \left(\frac{1+e}{\lambda-\kappa}\right)(S_i - 1)\bar{\varepsilon}_d^p \tag{3.19}$$

Where λ is the slope of the normal compression line in e- ln p plane, k_i is the rate of destructuration. Degradation of S_i is considered through destructuration plastic strain rate $\dot{\varepsilon}_d^p$ defined as,

$$\dot{\varepsilon}_d^p = \langle L \rangle \bar{\varepsilon}_d^p = \langle L \rangle \sqrt{(1-A)\left(\frac{\partial g}{\partial \bar{p}}\right)^2 + A\left(\frac{\partial g}{\partial \bar{q}}\right)^2} \tag{3.20}$$

A is a parameter distributing the destructuration between plastic volumetric strain and plastic deviatoric strain increments, by default A = 0.5.

The evolution of the rotational hardening is expressed as,

$$\dot{\alpha} = \langle L \rangle \bar{\alpha} = \langle L \rangle \left(\frac{1+e}{\lambda - \kappa} \right) C \left(\frac{\bar{p}}{p_0} \right)^2 \left| \frac{\partial g}{\partial \bar{p}} \right| \left| \bar{\eta} - x\alpha \right| \left(\alpha^b - \alpha \right) \tag{3.21}$$

Where e is the void ratio, λ and κ are the slopes of loading and unloading/reloading lines in the e- ln p plane, C is a model constant controlling the rate of rotational hardening, x is a model constant which regulates the degree of anisotropy that can evolve under a constant stress ratio $\bar{\eta}$ and α^b is the minimum value of (N,M) taken as,

$$\begin{aligned} (\bar{\eta} / x) \geq \alpha, \alpha^b &= \min(N, M_c) \\ (\bar{\eta} / x) < \alpha, \alpha^b &= \min(-N, -M_e) \end{aligned} \tag{3.22}$$

For the evolution of the rotational hardening variable, modulus value is the plastic volumetric strain because when the stress state lies on the dry side of the critical state line, negative plastic volumetric strains will be produced leading to rotation of the plastic potential in the opposite direction as opposed to the sign of stress ratio $\bar{\eta}$. In order to have real valued image stresses in equation (3.6), $|\alpha| < M$, and for this purpose the rate of evolution of the rotational hardening is dependent of the stress ratio distance $(\alpha^b - \alpha)$, where α^b is the bounding image on the bounding surface. This term also determines the direction of rotation of the bounding surface. The usage of absolute value of $\left| \bar{\eta} - x\alpha \right|$ is precisely done in order to avoid erroneous sign changes of $\dot{\alpha}$.

3.5 Loading index and plastic modulus

The loading index or the plastic multiplier is obtained by the consistency condition, $\dot{F} = 0$ giving rise to,

$$L = \frac{1}{K_p} \left[\left(\frac{\partial F}{\partial \bar{p}} \right) \dot{p} + \left(\frac{\partial F}{\partial \bar{q}} \right) \dot{q} \right] \tag{3.23}$$

Where K_p is the plastic modulus. the stress reversal is assumed to take place whenever L = 0.The loading index L is taken as zero whenever L < 0 instead of the negative value itself in order to update the projection center to the point of initiation of shearing preceded by unloading in isotropic consolidation.

Bounding surface concept requires that the plastic strains are produced inside the bounding surface. For this to happen, the plastic modulus must be defined for any stress state within the bounding surface as well. Plastic modulus(K_p) inside the bounding surface is related to the bounding surface plastic modulus ($\bar{K}_p$) through Euclidean distance δ (between $(\bar{p},\bar{q})$ and (p,q)) and r (between $(\bar{p},\bar{q})$ and (p_c,q_c)). When the stress state is on the bounding surface the δ is zero implying that $K_p = \bar{K}_p$, and when the stress state is within the bounding surface δ is greater than zero rendering $K_p > \bar{K}_p$, thereby producing plastic strains. A point to be noted is that when inside the bounding surface, since the plastic modulus increases, the amount of plastic strains being produced reduced, i.e higher the δ lesser the amount of plastic strains being produced. $\bar{K}_p$ is obtained by the use of consistency condition on the bounding surface as,

$$\overline{K_p} = -\left[\left(\frac{\partial F}{\partial p_0}\right)\overline{p_0} + \left(\frac{\partial F}{\partial \alpha}\right)\overline{\alpha}\right] \tag{3.24}$$

The corresponding plastic modulus K_p[6] for any stress state within the bounding surface is defined as,

$$K_p = \overline{K_p} + \frac{hp_0^3\delta}{\langle r - s\delta \rangle} = \overline{K_p} + \frac{hp_0^3}{\left\langle \frac{b}{(b-1)} - s \right\rangle} \tag{3.25}$$

Where h is the positive hardening function, $r/\delta = b/(b-1)$ with $1 \leq b \leq \infty$ where b is the similarity ratio as defined in 3.3, $s \geq 1$ is an indirect measure of the size of the elastic nucleus which is also a surface homologous to the bounding surface with the center of homology as PC. When the value of s is set to ∞, the elastic nucleus will coincide with the bounding surface rendering purely elastic strains inside the bounding surface. On the contrary, when the value of s is set to 1, the elastic nucleus is shrunk to a single point coinciding with the PC. In the present formulations, the value of s is set to 1 and numerically there are no pure elastic strains produced.

3.6 Hardening function and damage parameter

The shape hardening function h controls the plastic modulus and is assumed to be a decaying function of its initial value h_0 through the parameter d which is a state variable simulating damage effect,

$$h = \frac{h_0}{1+d} \tag{3.26}$$

The damage effect d evolves linearly with the increment in plastic deviatoric strains as follows,

$$\dot{d} = a_d \left|\dot{\varepsilon}_q^p\right| \tag{3.27}$$

Where a_d is a model constant which controls the rate of evolution of d.

3.7 Projection center

In the context of bounding surface SANICLAY, as per Seidalinov (2012), the PC evolves in a dual way. Firstly whenever there is stress reversal the PC gets updated to the point of stress reversal. This update of PC is necessary to better predict the plastic strains during the course of cyclic loading. The point of stress reversal is identified by the help of loading index (which is described in the section 3.5). Analytically whenever the loading index is less than or equal to zero stress reversal occurs.

[6] Plastic modulus must always be greater than or equal to zero.

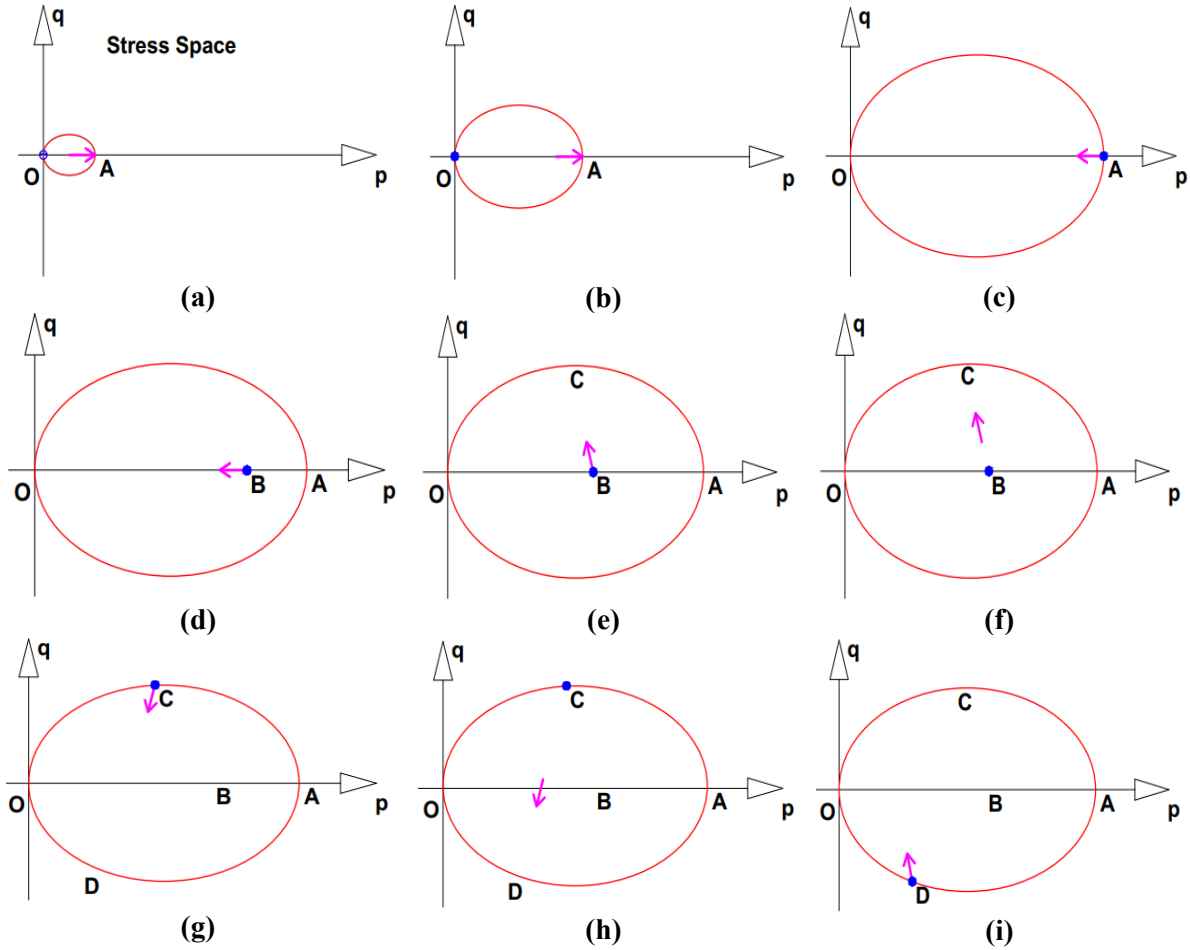

Figure 3.2 : Schematic representation of evolution of projection center with stress reversals.

A schematic representation of the evolution of the PC with stress reversals is presented in Figure 3.2. Where blue dot represents the projection center, pink arrow represents the direction of stress path, the red ellipse represents the bounding surface, x-axis represents mean effective stress/isotropic stress and y-axis represents the deviatoric stress. For the purpose of explanation, a case of stress controlled loading in triaxial setup is considered where axial stress increment is given as the input. In addition the gradient of bounding surface (F) with respect to the image stress is needed for better understanding the concept which is as follows,

$$\frac{\partial F}{\partial \bar{\sigma}} = \begin{bmatrix} \frac{\partial F}{\partial \bar{p}} & \frac{\partial F}{\partial \bar{q}} \end{bmatrix} = \begin{bmatrix} \bar{p}\left(N^2 - \bar{\eta}^2\right) & 2\bar{p}\left(\bar{\eta} - \alpha\right) \end{bmatrix} \tag{3.28}$$

Interpretation of the figures is as follows,

- PC at the start of loading is taken at origin as a default (Point ‘O’). When the soil element is isotropically consolidated (only in the case of isotropic consolidation volumetric stress increment is given as input), the stress path of the soil follows the isotropic stress axis as seen in (b) in Figure 3.2, but the PC still stays at the origin ‘O’, since during the isotropic consolidation loading as per equations (3.23) and (3.28), loading index is always greater than zero.

- When the soil is isotropically unloaded from point 'A' ((c) in Figure 3.2), the projection of the current stress onto the bounding surface ideally points towards the origin as a result of which the gradient of bounding surface (F) with respect to the current stress state becomes zero. This indeed results in zero loading index, as a result of this the PC gets updated to the point 'A'. From here it is quite evident that during the process of isotropic unloading the loading index always remains zero and hence PC follows the stress point on the isotropic stress axis.
- Now, if the soil element is sheared from point 'B' ((e) in Figure 3.2), the projection of the current stress onto the bounding surface points towards point 'C'. So the gradient of F with respect to the current stress becomes positive, also the stress increments are positive leading to a positive loading index. At this moment, PC gets updated to point 'B'. A point to be noted is that point 'B' is also representative of an over-consolidated state, so whenever a soil element is sheared from an over-consolidated state originating at the isotropic stress axis, the PC must be updated to the that point on the isotropic stress axis (in here the point is 'B').
- During the process of loading from point 'B' to point 'C', loading index continues to remain positive and PC stays at point B (at point B, PC evolves slightly only to remain inside the BS which will be explained later in this section). When the load increment is reversed at point 'C' ((g) in Figure 3.2), for a momentary instance the image stress is at point 'C' which leads to positive values for gradient of F with respect to the current stress state, but the stress increment is negative leading to a negative loading index, thereby the PC gets updated to point 'C'. During the process of unloading (point C to the isotropic stress axis) and reloading (isotropic stress axis to the point D), the image stress is pointed towards point 'D'[7] which ideally means a negative stress ratio η, this results in negative value of gradient of F with respect to deviatoric component of image stress. Also during the process of unloading-reloading from 'C' to 'D', since the input deviatoric stress increment is negative, the loading index becomes positive which means the PC continues to stay at point 'C'.

Similar procedure is followed for updating the PC at point 'D' as well. For the illustration purpose, points 'C' and 'D' are shown on the bounding surface but even if there is some kind of stress reversal occurring between point 'B' and 'C' or 'C' and 'D', PC will be updated accordingly.

Secondly, this updated PC evolves with the changing stress levels be it loading, unloading or reloading. The concept behind this evolution is to guarantee a unique image stress by positioning the PC always within the bounding surface. If the PC is kept fixed until the next point of stress reversal there is a high possibility of PC to fall outside the bounding surface when the latter expands, contracts or rotates with the alteration of the stress state.

The evolution of the PC with respect to alteration of the stress state depends upon the isotropic hardening p_0 and the rotational hardening α. The evolvement of PC with respect to p_0 is given by,

$$\dot{p}_c = \frac{p_c}{p_0}\,\dot{p}_0, \qquad \dot{q}_c = \frac{q_c}{p_0}\,\dot{p}_0 \tag{3.29}$$

On the other hand to account for the rotation of the bounding surface with respect to α, the distance along the q-axis is affected in such a way that a proportionality is maintained between the distance of PC from the α-axis as shown in Figure 3.3. By doing so p_0 and p_c will remain unchanged.

[7] Point to be noted is that throughout the process of unloading-reloading the image stress does not stay at point 'D' but might stay near its vicinity depending upon the amount of stress or strain increment given

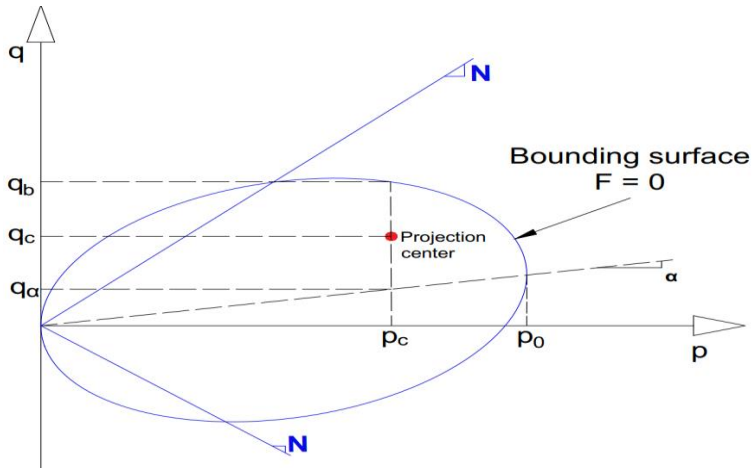

Figure 3.3 : Updating projection center with respect to rotational variable α

The proportionality of the distance of PC from α-axis to that of bounding surface is represented by X,

$$X = \frac{q_c - q_\alpha}{q_b - q_\alpha} \tag{3.30}$$

Where $q_\alpha = \alpha p_c$ and the denominator of the equation is obtained by equation F = 0,

$$(q_b - q_\alpha) = \left[\left(N^2 - \alpha^2\right) p_c \left(p_0 - p_c\right)\right]^{\frac{1}{2}} \tag{3.31}$$

On the basis of which the corresponding change of PC with respect to α is given by,

$$\dot{q}_c = \left[p_c - X \frac{p_c \left(p_0 - p_c\right)\alpha}{\left[\left(N^2 - \alpha^2\right) p_c \left(p_0 - p_c\right)\right]^{\frac{1}{2}}} \right] \dot{\alpha} \tag{3.32}$$

By combining equations (3.29) and (3.32), the total effect of change in PC with regard to both isotropic and rotational hardening is given by,

$$\dot{q}_c = \frac{q_c}{p_0} \dot{p}_0 + \left[p_c - X \frac{p_c \left(p_0 - p_c\right)\alpha}{\left[\left(N^2 - \alpha^2\right) p_c \left(p_0 - p_c\right)\right]^{\frac{1}{2}}} \right] \dot{\alpha} \tag{3.33}$$

3.8 Summary

This chapter has presented the formulation of bounding surface SANICLAY model in triaxial space. Importance must be given in the way the stiffness is defined which depends upon the distance between the current stress point and its corresponding image on the bounding surface. Also the projection center which acts as center of homology for the bounding surface and the loading surface (which represents the current stress state) tends to evolve in dual ways. Firstly whenever there is stress reversal the PC gets updated to the point of stress reversal. This update of PC is necessary to better predict the plastic strains during the course of cyclic loading. Secondly, this updated PC evolves with the changing stress levels be it loading, unloading or reloading. The concept behind this evolution is to guarantee a unique image stress by positioning the PC always within the bounding surface.

Chapter 4 : Implementation and verification of model

4.1 Implementation of the model in MATLAB

This section deals with the implementation of the bounding surface SANICLAY model in MATLAB. In this thesis, computations are focused on simulation of undrained triaxial monotonic and undrained triaxial cyclic loading conditions. With the help of constraints provided by Bardet, (1991) an explicit stress controlled technique has been employed to numerically implement the bounding surface SANICLAY model in MATLAB.

4.1.1 General procedure for integration of the constitutive model

The mixed constraints as suggested by Bardet, (1991) for the case of undrained triaxial loading leads to,

$$\dot{\sigma} = D^{ep}\,\dot{\varepsilon}$$
$$\begin{Bmatrix} \dot{p} \\ \dot{q} \end{Bmatrix} = \begin{bmatrix} D_{pp} & D_{pq} \\ D_{qp} & D_{qq} \end{bmatrix} \begin{Bmatrix} \dot{\varepsilon}_v \\ \dot{\varepsilon}_q \end{Bmatrix} \tag{4.1}$$

Where D^{ep} is an elastoplastic stiffness matrix or the tangent stiffness matrix. In equation (4.1) the deviatoric stress increment $\dot{q}$ (in triaxial space it is also called as the axial stress increment) is given as input. The volumetric strain $\dot{\varepsilon}_v$ is zero since the simulated test is undrained. By imposing the aforementioned conditions and rearranging the above equation, the volumetric stress increment and deviatoric strain increment can be computed by,

$$\dot{p} = D_{pq} D_{qq}^{-1} \dot{q}$$
$$\dot{\varepsilon}_q = D_{qq}^{-1} \dot{q} \tag{4.2}$$

Primarily the elastoplastic stiffness matrix is computed in case of the plastic loading conditions as the tangent to the current values of stress. To know if the current values of the stresses correspond to loading or unloading conditions a trial stress is computed with the elastic stiffness matrix (D^e) as follows,

$$\dot{\sigma} = D^e \dot{\varepsilon}^e$$
$$\begin{Bmatrix} \dot{p} \\ \dot{q} \end{Bmatrix} = \begin{bmatrix} K & 0 \\ 0 & 3G \end{bmatrix} \begin{Bmatrix} \dot{\varepsilon}_v^e \\ \dot{\varepsilon}_q^e \end{Bmatrix} \tag{4.3}$$

If the scalar product between the trial stress increment and the normal to the yield[8] surface is positive, then the trial stress increment corresponds to plastic loading. Otherwise, it is found to be elastic unloading which can be mathematically represented as,

(4.4)

[8] Here the terminology “yield surface” has been used but in case of bounding surface models, this yield surface is replaced by the bounding surface which shall be explained in the next section.

$$\{\dot{p} \quad \dot{q}\}\begin{Bmatrix}\frac{\partial f}{\partial p}\\ \frac{\partial f}{\partial q}\end{Bmatrix}=\begin{cases}>0 & \Rightarrow \quad \textit{Loading}\\ <0 & \Rightarrow \quad \textit{Unloading}\end{cases}$$

If the trail stress results in unloading condition, then the computed stress itself will be the final stress and the integration proceeds into the next substep. Otherwise, the increment in stress and strain, as in equation (4.2), have to be recomputed based on the elasto-plastic stiffness matrix as follows,

$$D^{ep}=\left[D^{e}-\frac{D^{e}\frac{\partial g}{\partial \sigma}\frac{\partial F}{\partial \sigma}D^{e}}{K_{p}+\frac{\partial F}{\partial \sigma}D^{e}\frac{\partial g}{\partial \sigma}}\right] \tag{4.5}$$

where f is the yield surface, g is the plastic potential and K_p is the plastic modulus defined as,

$$K_{p}=-\frac{\partial f}{\partial \chi}\dot{\chi} \tag{4.6}$$

where χ represents the hardening variables in the constitutive model.

Provided that the increments of total stress and total strain quantities are evaluated by now, the elastic strain increments can be computed as,

$$\begin{Bmatrix}\dot{\varepsilon}_{v}^{e}\\ \dot{\varepsilon}_{q}^{e}\end{Bmatrix}=\begin{bmatrix}K & 0\\ 0 & 3G\end{bmatrix}^{-1}\begin{Bmatrix}\dot{p}\\ \dot{q}\end{Bmatrix} \tag{4.7}$$

In equation (4.7), the stress quantities thus used must be the true stress quantities finalized after checking the loading conditions based on equation (4.4). Since the elastic strains are known, plastic strains can now be computed by subtracting the elastic strains from the total strains as $\dot{\varepsilon}^{p}=\dot{\varepsilon}-\dot{\varepsilon}^{e}$. On another note, the fact that the volumetric strain is zero does not necessarily mean that both elastic and plastic volumetric strains are also zero. However, they would be of equal magnitude despite having opposite signs.

4.1.2 Incorporation of bounding surface Saniclay features into the integration procedure

This section deals with the changes need to be made in order to implement the integration technique employed in section 4.1.1 for a bounding surface model. As mentioned earlier, for any stress state on or inside the bounding surface, there exists a unique image stress lying on the bounding surface (section 3.3). So, ideally the loading or unloading condition is checked based on the equation of bounding surface comprising of the image stresses and is represented in the following way,

(4.8)

$$\{\dot{p} \qquad \dot{q}\}\begin{Bmatrix}\dfrac{\partial F}{\partial \bar{p}}\\ \dfrac{\partial F}{\partial \bar{q}}\end{Bmatrix}=\begin{cases}>0 & \Rightarrow \quad \textit{Loading}\\ <0 & \Rightarrow \quad \textit{Unloading}\end{cases}$$

Since the plastic modulus is always positive or equal to zero, in a way the scalar multiplier in equation (4.8) resembles the loading index in section 3.5 and can be rightly used in the case of bounding surface to find the stress reversal. Whenever there is an unloading condition as per equation (4.8) a stress reversal is detected. At the instance of stress reversal, the projection center gets updated to the point of stress reversal. In addition, the image stress must also be updated to the opposite side of the bounding surface at this instance. Failure to implement this step, will result in inadequate calculations of bounding surface's gradients, plastic potential etc. These inadequacies will mean that the scalar multiplier will always point at the unloading conditions or there might also be a possibility that the plastic modulus is calculated wrongly. The way of updating the image stress[9] at the instance of stress reversal is given by,

$$\bar{q}=\pm\sqrt{\left(N^2-\alpha^2\right)\bar{p}\left(p_0-\bar{p}\right)}+\bar{p}\alpha \tag{4.9}$$

For the chosen specific cyclic loading condition, the volumetric image stress remains unchanged in both loading and unloading conditions. However, the deviatoric image stress must change its direction in accordance with the change of the projection center in the triaxial plane.

Another change in implementation, as opposed to the method followed in section 4.1.1, is the way plastic modulus is defined for bounding surface. The plastic modulus is the sum of the plastic modulus calculated on the bounding surface plus the distance dependent modulus value between the current stress point and the image point. So, in this case first the computations of the plastic modulus are made on the bounding surface and then the additive term corresponding to the distance between the stress point and the image point is computed.

A skeletal diagram for the flow of code is presented in Figure 4.1.

[9] Note that the way of updating the image stress presented in this thesis is applicable only for a specific case of cyclic loading condition.

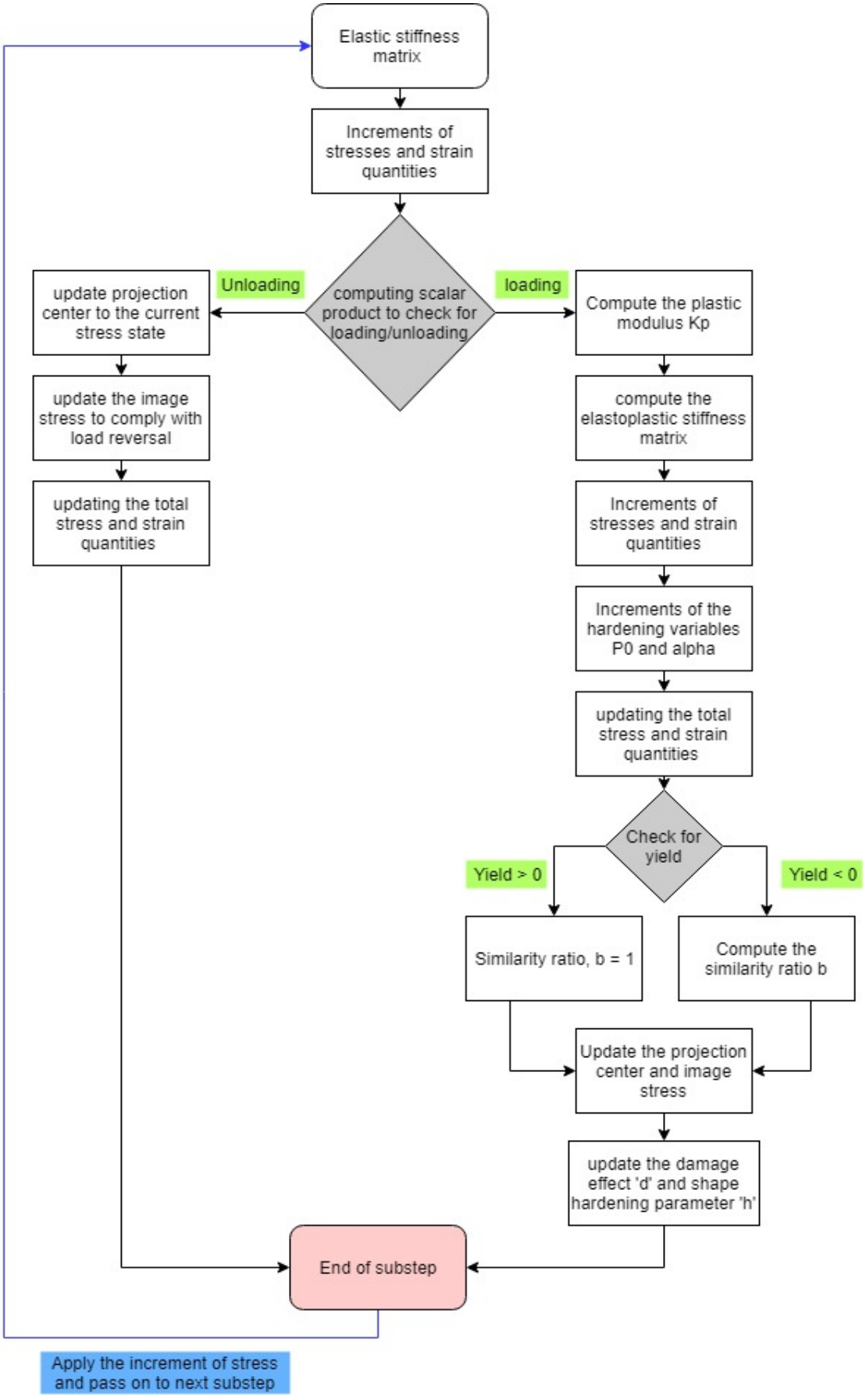

Figure 4.1 : Flow of code in MATLAB for the implementation of bounding surface SANICLAY model.

4.2 Verification and sensitivity analysis of the implementation

Prior to verifying the implementation of the code. Sensitivity of the integration is checked by varying the timestep of the stress increment in the range of 10^{-2} to 10^{-5}. With a stress increment of the order of 10^{-3} the values of the plots obtained have shown a reasonable match with that of the results obtained from a stress increment of the order of 10^{-5}. Considering that the time taken with a lower stress increment (10^{-5}) is really high compared to that with higher time increment (10^{-3}), a stress increment value of the order of 10^{-3} has been chosen for the computations here after.

4.2.1 Verification of the model

To check if the implemented code is working and rightly in order, simulations have been run and compared with the results from Seidalinov (2012,2013). The pertaining model constants and initial conditions used to run the simulations are presented in Table 4.1 and Table 4.2.

Table 4.1 : model constants used for running the verification analysis.

Category	Model constant	Symbol	value	Units
Elasticity	Swelling index	κ	0.03	-
	Poisson's ratio	ν	0.2	-
Critical state	Compression index	λ	0.15	-
	Critical state ratio in triaxial compression	M_c	1	-
	Critical state ratio in triaxial extension	M_e	1	-
Bounding surface	Peak stress ratio on bounding surface / Shape of bounding surface	N	1	-
	Initial hardening parameter	h_0	varied	$(kPa)^{-2}$
	Rate of damage evolution	a_d	varied	-
Rotational hardening	Rate of evolution of anisotropy	C	5	-
	Saturation limit of anisotropy	x	1.7	-
Destructuration	Rate of destructuration	k_i	0	-

Table 4.2 : initial conditions use for running the verification analysis.

Model variable	Symbol	Value	Units
Initial void ratio	e	0.7	-
Initial size of the bounding surface	P_0	200	kPa
Initial orientation of the bounding surface	α	0	-
Initial isotropic structuration factor	S_i	1	-
Initial damage parameter	d	0	-

All the simulations in this chapter use the same set of data provided in the aforementioned tables, if there is any change with respect to the parameters or constants used, it will be mentioned explicitly.

4.2.1.1 Verification for the monotonic tests

In the case of monotonic loading, undrained triaxial simulations have been carried out at two different over consolidation ratios (OCR), 1.5 and 3 respectively. The stress path and the stress-strain responses have been plot and the obtained results were verified against the digitized values of the plots in Seidalinov (2012) by using "webplotdigitizer"[10]. Thus obtained results have been tabulated below the respective figures[11]. In the process of carrying out simulations, sensitivity analysis is also performed on

[10] An online tool to digitize the graphs and images, WebPlotDigitizer (2019)
[11] The plots have been normalized using $p_{0,in}$ which is the initial size of the bounding surface.

'h_0' by keeping $a_d = 0$. When $a_d = 0$, 'h' becomes a constant (equation (3.26) and (3.27)) throughout the loading path. A point to be noted is that the influence of 'h' comes into picture only when the stress state is inside the bounding surface, since when the stress state is on the bounding surface, the similarity ratio will become unity and the term containing 'h' in equation (3.25) will vanish altogether as the denominator will tend to infinity.

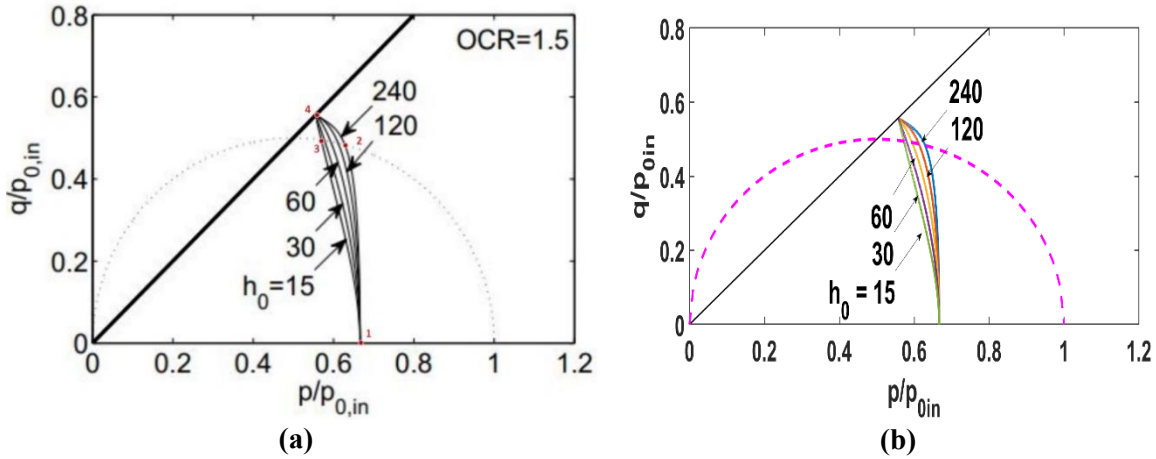

Figure 4.2 : Normalized stress path a) results from Seidalinov (2012); b) results from computations for varying h_0 values and OCR = 1.5.

Table 4.3 : Comparison of digitized values vs computational values for varying h_0 values and OCR = 1.5.

s.no	q/ $p_{0,in}$	p/ $p_{0,in}$ (Seidalinov 2012)	p/ $p_{0,in}$ (computations)	% difference
1	0.0	0.667	0.667	0.00
2	0.484	0.631	0.629	0.32
3	0.495	0.571	0.572	-0.18
4	0.559	0.559	0.556	0.54

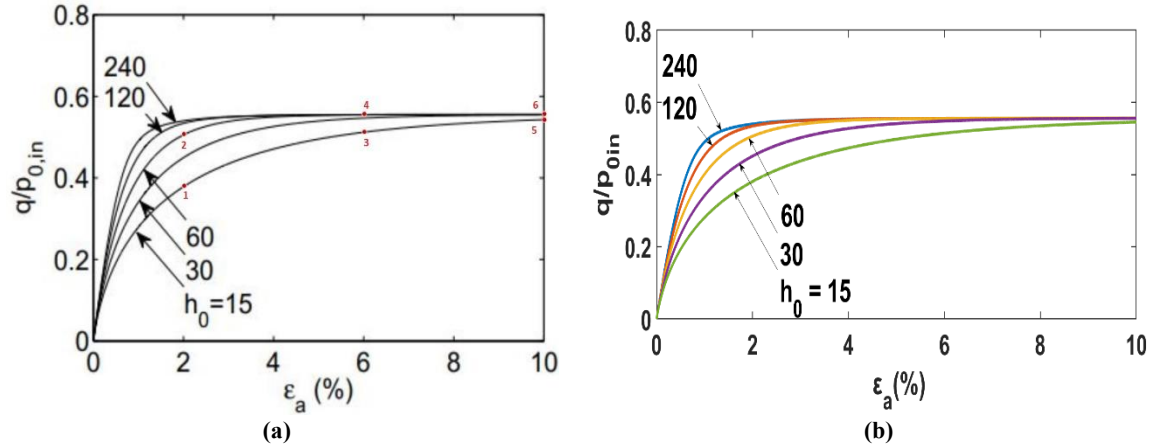

Figure 4.3 : Normalized stress-strain curve a) results from Seidalinov (2012); b) results from computations for varying h0 values and OCR = 1.5.

Table 4.4 : Comparison of digitized values vs computational values for varying h_0 values and OCR = 1.5.

s.no	q/$p_{0,in}$	ε_a(%) (Seidalinov 2012)	ε_a(%) (computations)	% difference
1	2	0.381	0.382	-0.26
2	2	0.508	0.507	0.20
3	6	0.514	0.515	-0.19
4	6	0.558	0.556	0.36
5	10	0.543	0.545	-0.37
6	10	0.558	0.556	0.36

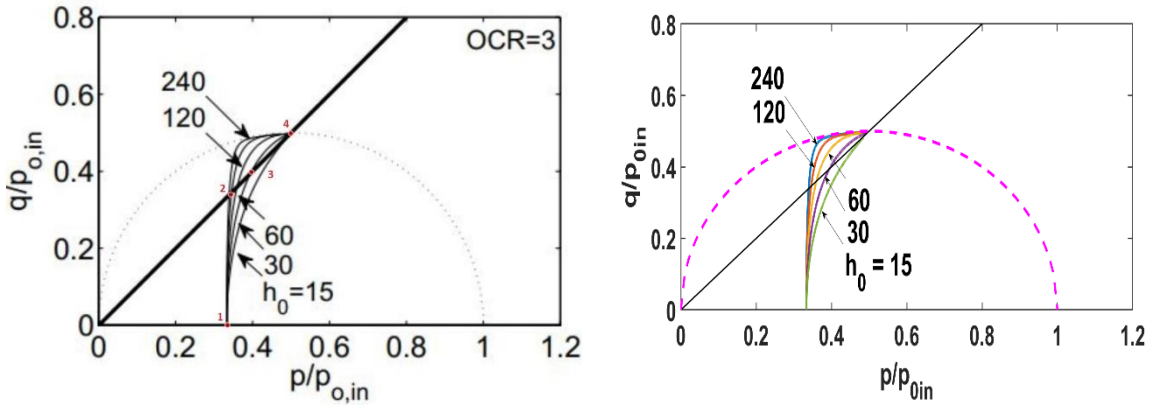

Figure 4.4 : Normalized stress path a) results from Seidalinov (2012); b) results from computations for varying h_0 values and OCR = 3.

Table 4.5 : Comparison of digitized values vs computational values for varying h_0 values and OCR = 3.

s.no	q/ $p_{0,in}$	p/ $p_{0,in}$ (Seidalinov 2012)	p/ $p_{0,in}$ (computations)	% difference
1	0	0.333	0.333	0.00
2	0.339	0.342	0.341	0.29
3	0.397	0.396	0.394	0.51
4	0.498	0.498	0.496	0.40

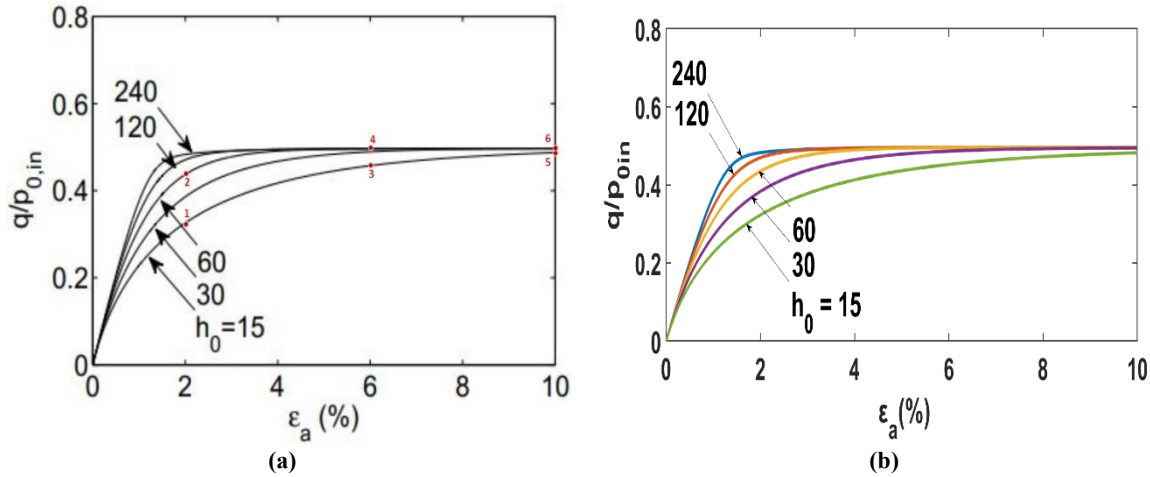

Figure 4.5 : Normalized stress-strain curve a) results from Seidalinov (2012); b) results from computations for varying h_0 values and OCR = 3.

Table 4.6 : Comparison of digitized values vs computational values for varying h_0 values and OCR = 3.

s.no	q/ $p_{0,in}$	ε_a(%) (Seidalinov 2012)	ε_a(%) (computations)	% difference
1	2	0.323	0.324	-0.31
2	2	0.44	0.436	0.91
3	6	0.46	0.453	1.52
4	6	0.50	0.495	1.00
5	10	0.489	0.482	1.43
6	10	0.50	0.496	0.80

Interpretation of the results reveal a contractive response when OCR = 1.5 and a dilative response when OCR = 3. When the OCR = 3, image stress will lie above the critical state line leading to a stress ratio

greater than critical stress ratio thereby the value of rate of plastic volumetric strains as per equation (3.7) will be negative which leads to increase in the volumetric stress which explains the dilative response. Similarly when the OCR = 1.5, image stress will lie below the critical state line leading to contractive behaviour. The stiffer response with increase in 'h_0' values can be explained from the plastic modulus (K_p) formulation in equation (3.25) where higher values of 'h' lead to higher K_p and lower loading index (L) which means lower plastic strains and higher stiffness.

As seen from Figure 4.2 to Figure 4.5, qualitatively there has been a good match between the results for both the stress path and stress-strain curves. It is quite evident from Table 4.3 to Table 4.6 that quantitatively as well the results show a good match wherein the percentage difference in the compared results varied from -0.5% to 1.5 %.

4.2.1.2 Verification for the cyclic tests

To verify the present code for cyclic loading, the results showing the influence of the model parameters h_0 and a_d have been taken from Seidalinov (2013) and the similar test have been simulated. Test conditions include six cycles of undrained triaxial loading under a cyclic stress ratio (csr) of 0.35 starting from normally consolidated state. Simulations have been performed with three different combinations of h_0 and a_d, interpretation of the results is as follows,

- $h_0 = \infty$ and $a_d = 0$: By taking the value of $h_0 = \infty$, whenever the stress point is inside the bounding surface, as per equation (3.25), K_p will tend to infinity which renders a zero loading index and thereby no plastic strains are generated. This implies that the bounding surface in this particular situation behaves like a yield surface meaning that plastic strains are produced only the yield surface and inside the yield surface only elastic strains are produced. Hence this explains the reason behind the stress path and stress-strain response retracing back the same path during unloading/reloading parts of the cyclic loading.
- $h_0 = 100$ and $a_d = 0$: Here since h_0 is taken as a finite value and a_d is taken as zero. The value of 'h' remains constant throughout the process of cyclic loading. Since h_0 is a finite value, plastic modulus will be a positive value inside the bounding surface which leads to generation of plastic strains. This in turn leads to evolution of stress path , i.e., in this particular case the reduction of the volumetric stress indicative of a contractive behaviour. A point to be noted would be that the stress path stagnates at $(p/\sigma_c) \approx 0.6$ (OCR ≈ 2), this can be explained by the fact that when $(p/\sigma_c) \approx 0.6$ the image stress projected by the projection center onto the bounding surface lies on the critical state line. When this situation occurs, $M = \eta$, i.e., the rate of increase in plastic volumetric strains will be almost equal to zero (equation (3.7)) implying there is no further development of volumetric stress. It also means that there is only development of plastic deviatoric strains which explains the partial evolution of the stress-strain response compared to the previous case. This can be resolved using a value of $a_d > 0$.
- $h_0 = 100$ and $a_d = 40$: In this case, by assigning a positive finite value to a_d, there is no major change in the generated stress-path. But the stress-strain response evolves. This evolution is due to the dependence of 'h' on the damage parameter a_d. Introduction of the damage parameter leads to evolution of the damage effect d (equation (3.27)) with the rate of plastic deviatoric strain, this leads to reduction in the value of h throughout the process of cyclic loading. This changing value of h effects the plastic modulus and hence results in evolution of the stress-strain curves. A point to be noted here is that the rate of change of plastic volumetric strains is almost zero when $(p/\sigma_c) \approx 0.6$, the whole evolution of axial strains from this point is completely due to the build-up of plastic deviatoric strains.

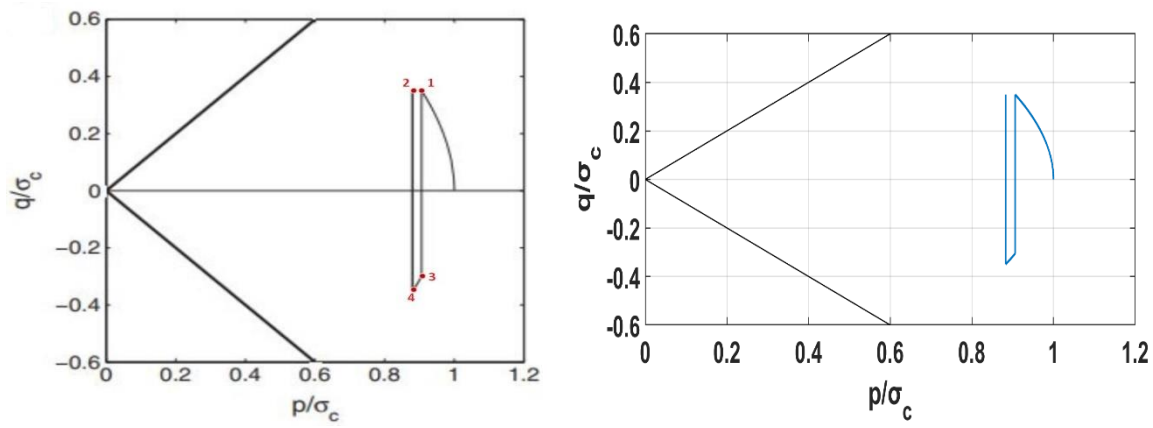

(a) (b)

Figure 4.6 : Normalized stress path a) results from Seidalinov (2013); b) results from computations for h_0 = inf and a_d = 0.

Table 4.7 : Comparison of digitized values vs computational values for varying h_0 = inf and a_d = 0.

s.no	q/σ_c	p/σ_c (Seidalinov 2013)	p/σ_c (computations)	% difference
1	0.35	0.906	0.906	0.00
2	0.35	0.883	0.883	0.00
3	-0.3	0.906	0.906	0.00
4	-0.35	0.882	0.883	-0.11

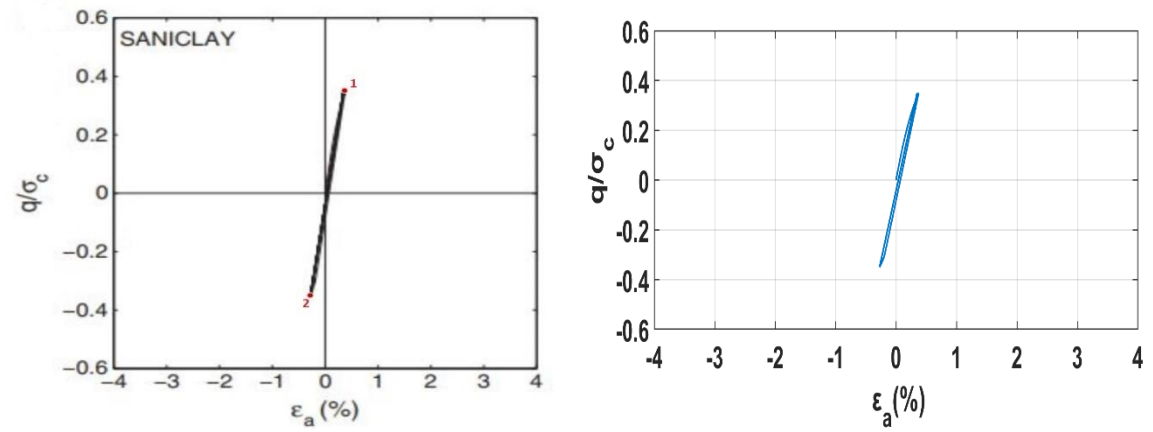

(a) (b)

Figure 4.7 : Normalized stress-strain curves a) results from Seidalinov (2013); b) results from computations for h_0 = inf and a_d = 0.

Table 4.8 : Comparison of digitized values vs computational values for varying h_0 = inf and a_d = 0.

s.no	q/σ_c	ε_a(%) (Seidalinov 2013)	ε_a(%) (computations)	% difference
1	0.35	0.373	0.374	-0.27
2	0.35	-0.277	-0.273	1.44

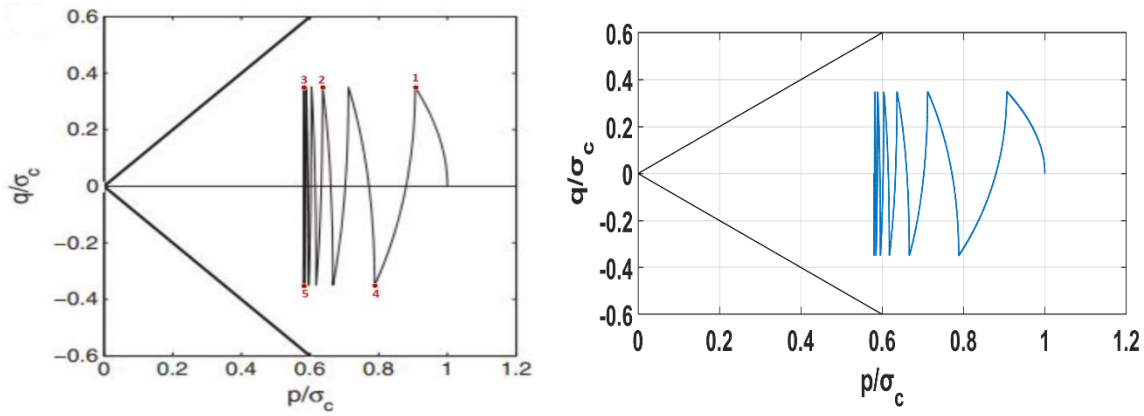

(a) (b)

Figure 4.8 : Normalized stress path a) results from Seidalinov (2013); b) results from computations for $h_0 = 100$ and $a_d = 0$.

Table 4.9 : Comparison of digitized values vs computational values for varying $h_0 = 100$ and $a_d = 0$.

s.no	q/σ_c	p/σ_c (Seidalinov 2013)	p/σ_c (computations)	% difference
1	0.35	0.904	0.906	-0.22
2	0.35	0.635	0.636	-0.16
3	0.35	0.579	0.582	-0.52
4	-0.35	0.786	0.788	-0.25
5	-0.35	0.579	0.579	0.00

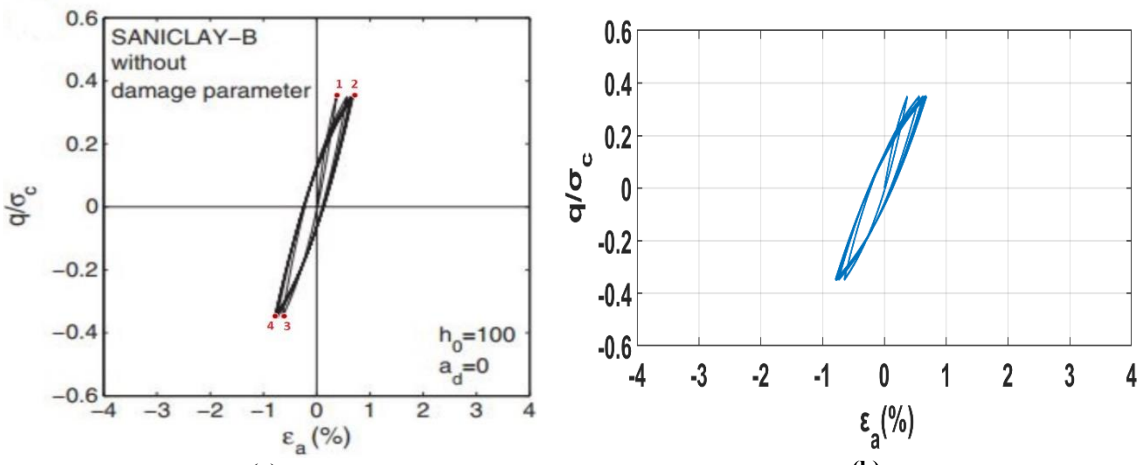

(a) (b)

Figure 4.9 : Normalized stress-strain curves a) results from Seidalinov (2013); b) results from computations for $h_0 = 100$ and $a_d = 0$.

Table 4.10 : Comparison of digitized values vs computational values for varying $h_0 = 100$ and $a_d = 0$.

s.no	q/σ_c	ε_a(%) (Seidalinov 2013)	ε_a(%) (computations)	% difference
1	0.35	0.362	0.374	-3.31
2	0.35	0.696	0.684	1.72
3	-0.35	-0.631	-0.649	-2.85
4	-0.35	-0.797	-0.791	0.75

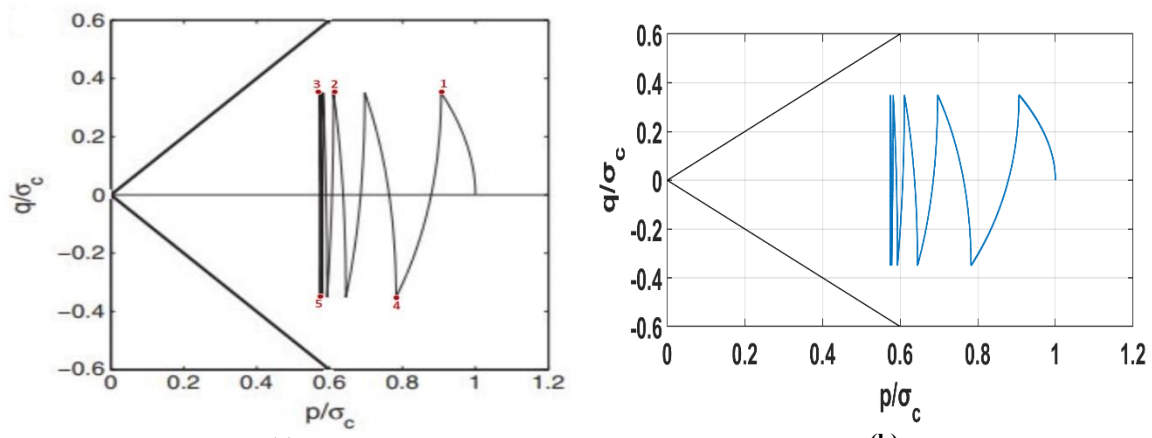

(a) (b)

Figure 4.10 : Normalized stress path a) results from Seidalinov (2013); b) results from computations for $h_0 = 100$ and $a_d = 40$.

Table 4.11 : Comparison of digitized values vs computational values for varying $h_0 = 100$ and $a_d = 40$.

s.no	q/σ_c	p/σ_c (Seidalinov 2013)	p/σ_c (computations)	% difference
1	0.35	0.907	0.906	0.11
2	0.35	0.614	0.611	0.49
3	0.35	0.569	0.575	-1.05
4	-0.35	0.781	0.783	-0.26
5	-0.35	0.573	0.575	-0.35

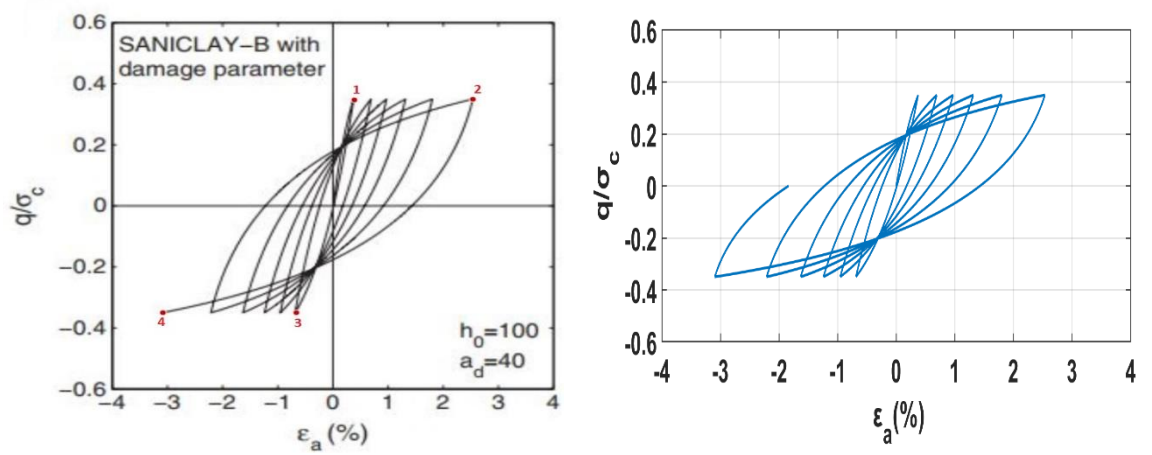

(a) (b)

Figure 4.11 : Normalized stress-strain curves a) results from Seidalinov (2013); b) results from computations for $h_0 = 100$ and $a_d = 40$.

Table 4.12 : Comparison of digitized values vs computational values for varying $h_0 = 100$ and $a_d = 40$.

s.no	q/σ_c	ε_a(%) (Seidalinov 2013)	ε_a(%) (computations)	% difference
1	0.35	0.377	0.374	0.80
2	0.35	2.521	2.536	-0.60
3	-0.35	-0.672	-0.687	-2.23
4	-0.35	-3.085	-3.095	-0.32

As seen from Figure 4.6to Figure 4.11, qualitatively there has been a good match between the results for both the stress path and stress-strain curves. It is quite evident from Table 4.7 to Table 4.12 that quantitatively as well the results show a good match wherein the percentage difference in the compared results varied from -3.5% to 2 %.

4.2.2 Sensitivity analysis of the model parameters

Bounding surface SANICLAY model is an extension of the modified Cam-Clay model. Taking this into account, sensitivity analysis is carried out only on parameters which are an addition to Cam-clay model, i.e., model constants such as Poisson's ratio, compression and swelling index, the critical state ratio's in compression and extension are kept constant. Model parameters tabulated in Table 4.1 along with h_0 = 100 and a_d =40 have been chosen for the subsequent analysis. Any changes in the specific parameters to carry out the sensitivity analysis are discussed in the corresponding subsections.

4.2.2.1 Analysis on the saturation limit of anisotropy 'x'

The saturation limit 'x' of the anisotropy has been varied from 1 to 1000 to check the sensitivity analysis. Though the values recorded in Seidalinov (2012) for different sets of clay were lying between 1 and 2, the sensitivity of the model response was almost ineffective for this range of data. So in order to check the sensitivity an attempt has been made by taking larger values of 'x'.

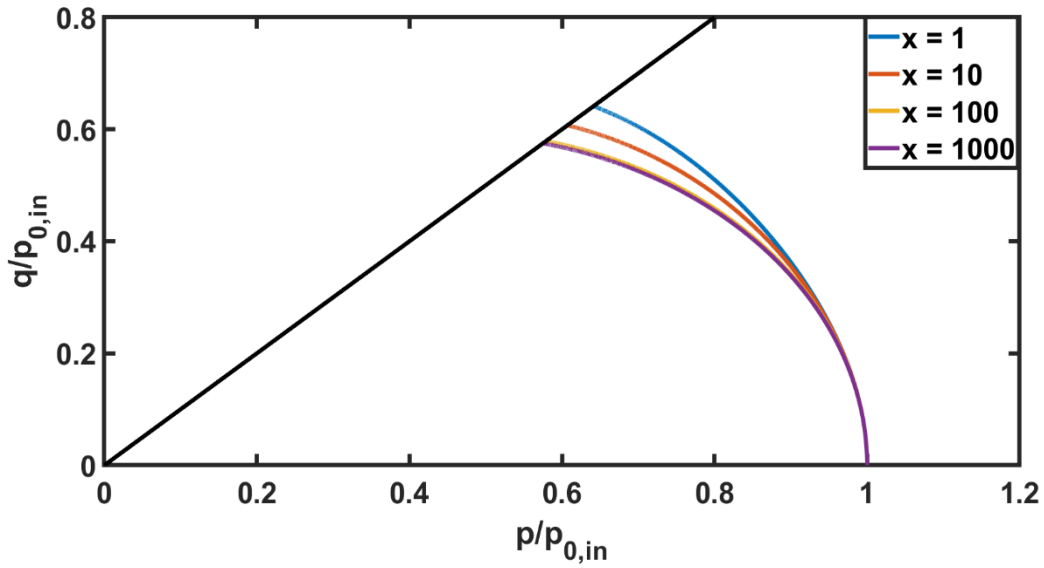

(a)

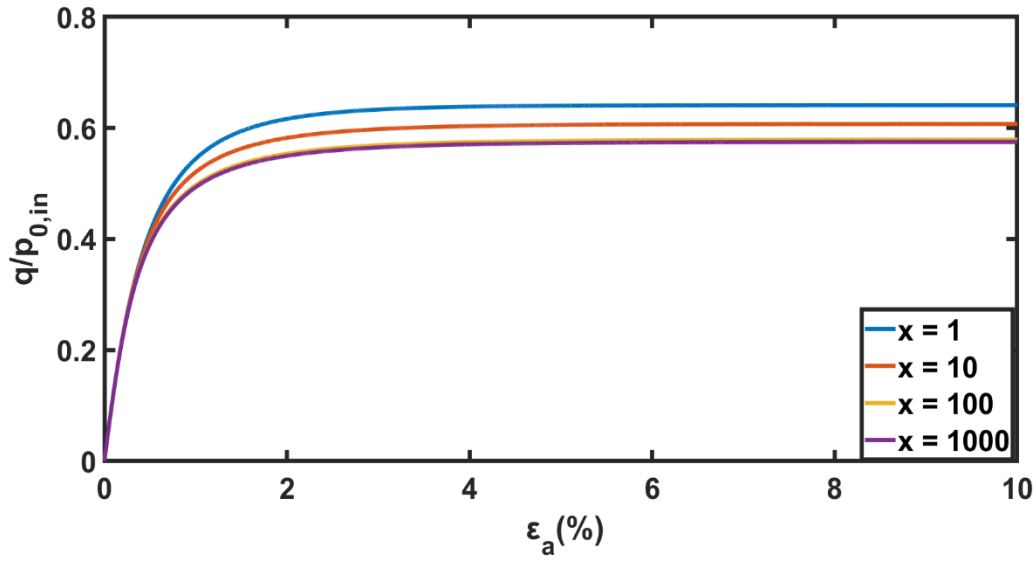

(b)

Figure 4.12 : (a) Stress path and (b) stress-strain response with varying values of 'x'.

Marginal change in the values of stress path and stress-strain response was observed with an increase in value of 'x'. It can be inferred from section 3.4 (equation (3.21)) that 'α' tends towards $\bar{\eta} / x$ for a constant stress ratio($\bar{\eta}$) loading, which means the effect of change in values of 'x' can be better understood under k_0 loading conditions. Since the code implemented in section 4.1 takes into consideration only isotropic loading conditions, sensitivity analysis thus performed might not show significant effect of variation in 'x'.

4.2.2.2 Analysis on 'N' for the evolution of rotational hardening 'α'

Parameter N serves as a bound for the evolution of the rotation hardening variable 'α' and the smaller the value of N compared to M_c the more undrained softening the model predicts during compression. Papadimitriou AG et al., (2005) suggested the limits for N as $M_c > N \geq M_e$ to predict softening only in compression and not in extension. However, in the present analysis the values of N have also be taken to be greater than M_c to check the model performance. In the plots that follows the parameter ζ represents the ratio of M_c/N.

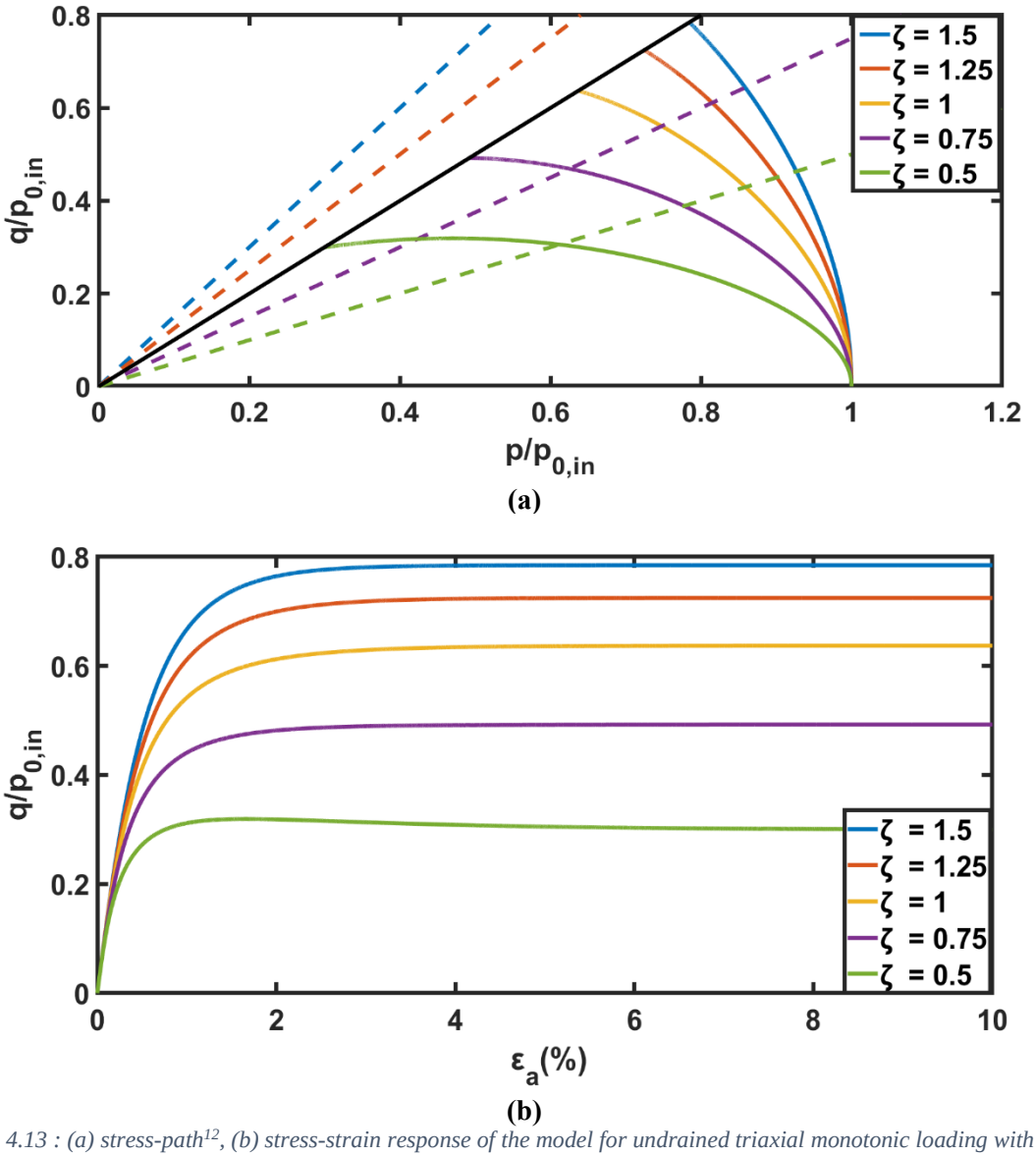

Figure 4.13 : (a) stress-path[12], (b) stress-strain response of the model for undrained triaxial monotonic loading with varying values of ζ.

[12] The black line in the figure is indicative of the critical state line.

It can be observed from Figure 4.13 that with increase in the value of ζ, the ultimate strength of the clay tends to increase. It can also be concluded that for a given value of shear stress, higher accumulation of pore water pressure is observed with reduction of ζ leading to faster reduction in effective volumetric stress. From part (a) of the figure it can be interpreted that the stress path tends to cease on the critical state line, this means that the volumetric strain stops developing. Strains developed over and above 4% axial strains (part (b) of the above figure) are completely due to the development of plastic deviatoric strains. In terms of stiffness, as the value of ζ increases, the model predicts stiffer response of clay.

Seidalinov (2013) performed cyclic loading simulations with a cyclic stress ratio of 0.35 using the data provided in Table 4.1, in order to have consistency in the results produced, the cyclic stress ratio was chosen as 0.35 which eliminates the option of using lower values of N such as 0.5 which resulted in a maximum cyclic stress ratio close to 0.3. As discussed earlier in section 2.1.3, cyclic loading leads to accumulation of pore water pressures and strains. By taking into account the obtained monotonic results in Figure 4.13 and foreseeing a slower rate of evolution of stress path with higher values of ζ, ζ values have been varied from 0.7 to 1.0 which lie well between the limits suggested by Papadimitriou AG et al., (2005).

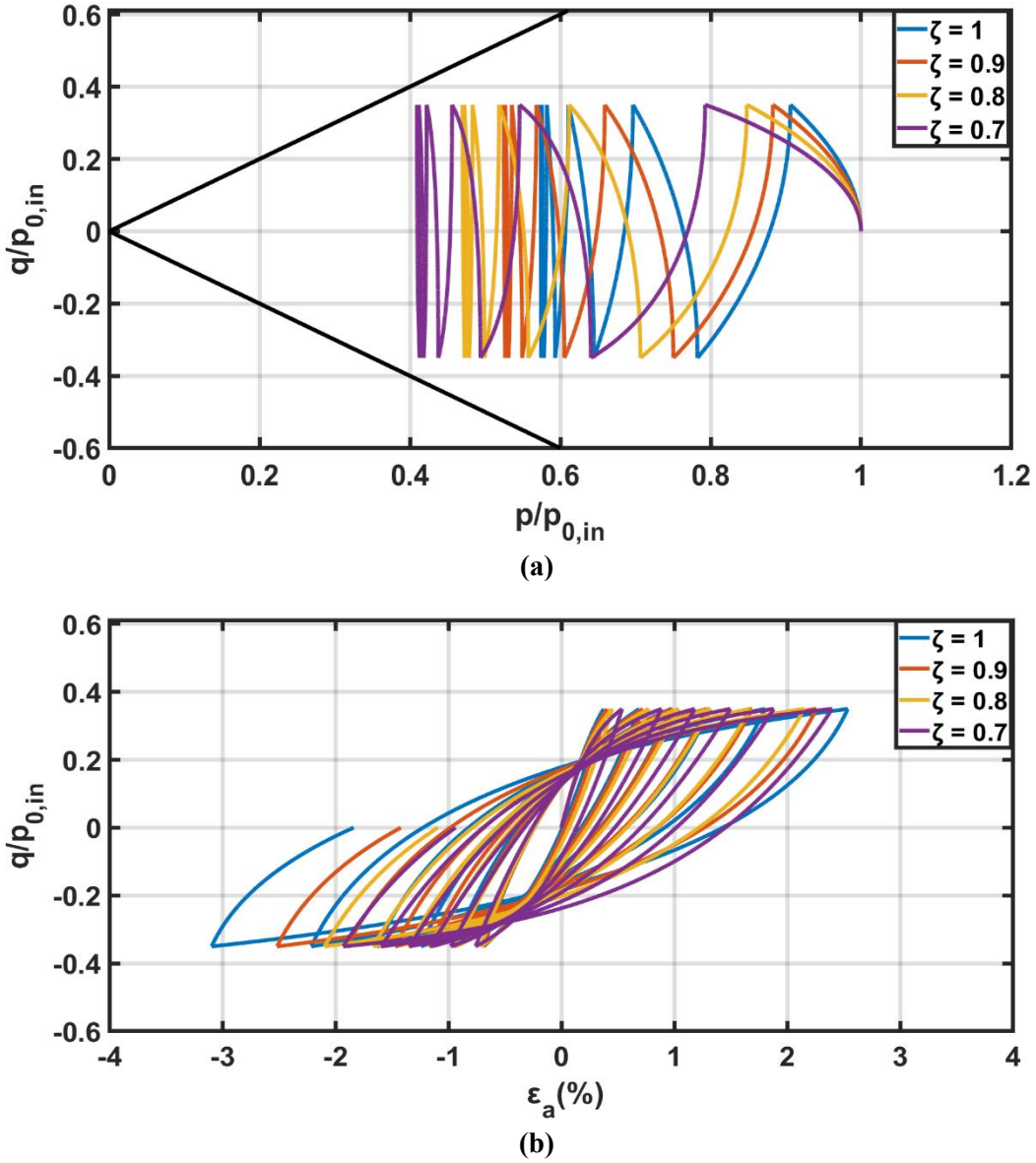

Figure 4.14 : (a) stress-path , (b) stress-strain response of the model for six cycles of undrained triaxial cyclic loading with varying values of ζ.

It is a known concept that under the influence of identical cyclic loading conditions, material with higher strength undergoes lesser degradation in strength than the material with lower strength. The stress path response of the model reaffirms the statement said earlier, where with decrease in ζ (leads to decrease in strength) leads to faster rate of migration of stress path towards the origin. As per literature, accumulation of plastic strains and pore water pressures are directly related (section 2.1.3) but analyzing the results from Figure 4.14, with the decrease in value of ζ, though a higher accumulation of pore water pressure (higher pore water pressure implies lesser volumetric stress) is observed, the developed shear strains are lesser.

An attempt was made to understand such behaviour from definition of loading index and bounding surface plastic modulus in equations (3.23) and (3.24) respectively, which when elaborated gives the following,

$$L = \frac{1}{K_p}\left[\bar{p}\left(N^2 - \bar{\eta}^2\right)\dot{p} + 2\bar{p}\left(\bar{\eta} - \alpha\right)\dot{q} \right] \tag{4.10}$$

$$\overline{K_p} = \left[\bar{p}\left(N^2 - \alpha^2\right)\overline{p_0} + 2\bar{p}\left(\bar{q} - \alpha p_0 \right)\bar{\alpha} \right] \tag{4.11}$$

It is evident form the above equations that the reduction in the value of 'N' leads to decrease in the value of loading index and plastic modulus. The development of the loading index and plastic modulus were plotted against the normalized volumetric stress in Figure 4.15. By visual inspection it can be observed that the values of loading index during final cycles of loading tend to decrease when ζ is changing from 1 to 0.8. Again with further decrease of ζ from0.8 to 0.7, the loading index values tend to increase. A clear increasing or decreasing trend in the loading index is not observed to give a conclusive explanation of development of shear strains as seen in part (b) of Figure 4.14. On the other hand, the peak values of the plastic modulus in part (b) of Figure 4.15 are representative of the stress reversals occurring during the process of cyclic loading. That is, whenever there is a stress reversal, there is a sudden increase in the plastic modulus values which tend to gradually reduce during the evolution of the stress path until there is a next stress reversal. At this stage, even the plot on plastic modulus variation cannot give a conclusive evidence to explain the variation in the development of shear strains as seen in part (b) of Figure 4.14.

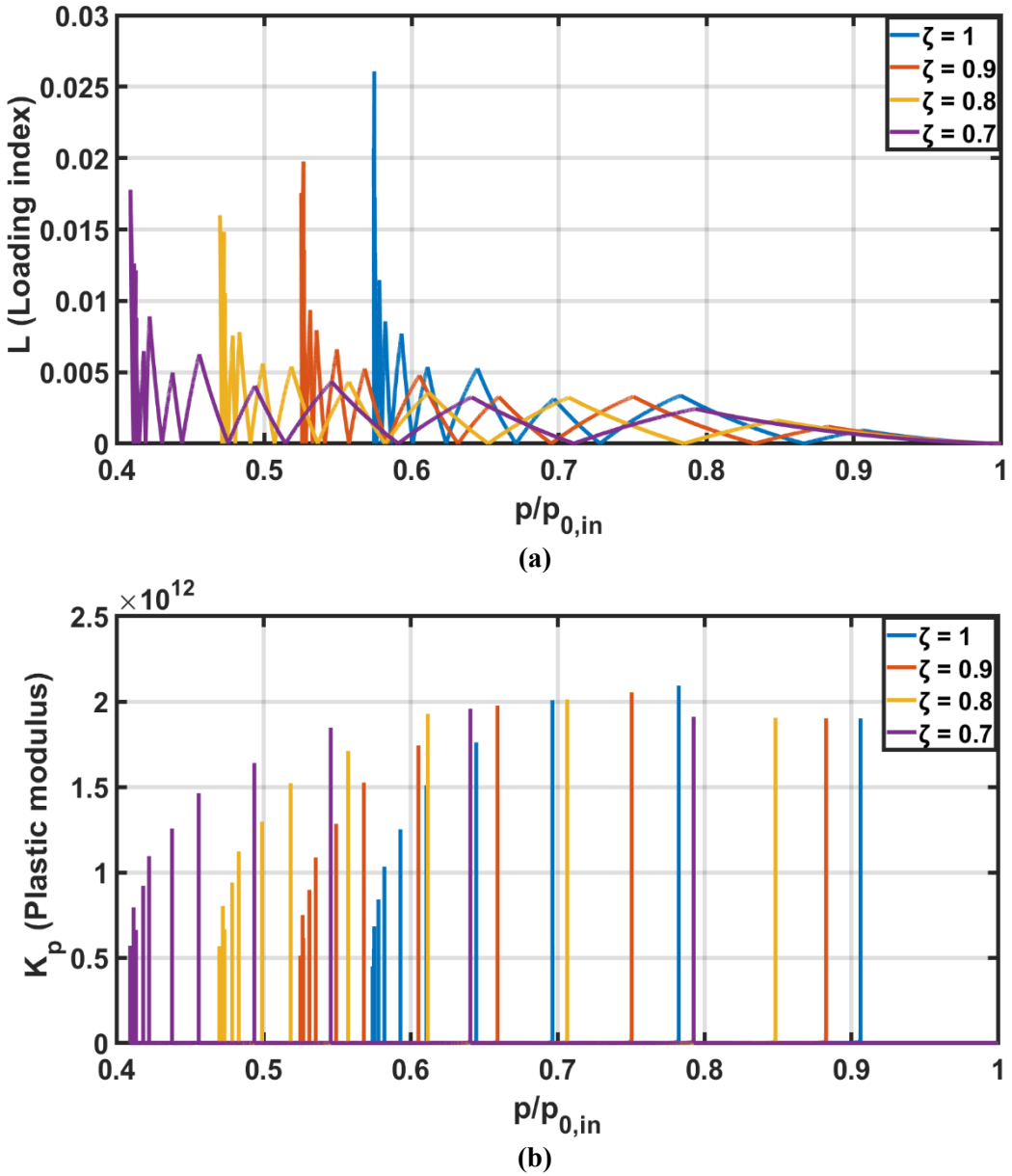

Figure 4.15 : (a) loading index and (b) plastic modulus development with variation of ζ.

4.2.2.3 Analysis on the rate of evolution of anisotropy 'C'

As per Dafalias YF et al., (2006) the value of C generally lies between 3 and 20. By choosing the range of C suggested by Dafalias YF et al., (2006), the change in response of the model in terms of stress-path was very minimal and difficult to interpret the effect of C. In order to understand the influence of C on the model, values ranging between 0 and 100 were chosen. A point to be noted is that when C = 0, during the process of loading/unloading, the orientation of the bounding surface remains fixed with respect to the origin which implies that the model is in effect not able to simulate the stress-induced anisotropy.

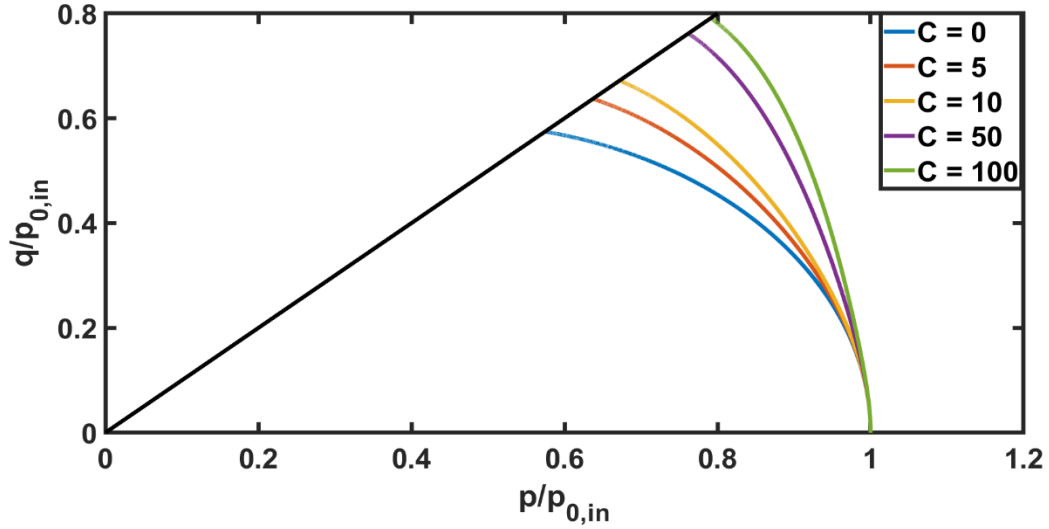

(a)

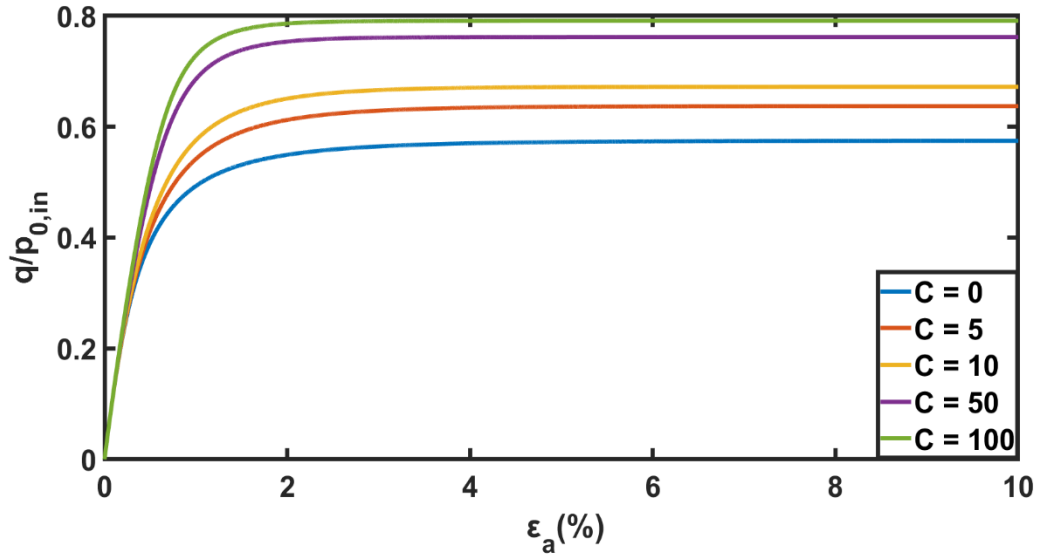

(b)

Figure 4.16 : (a) stress-path , (b) stress-strain response of the model for undrained triaxial monotonic loading with varying values of C.

It can be observed that the increase of C has a similar effect as that of increase in N, where with increase of C, the strength and stiffness of the clay increases. This can be understood from the fact that when C increases, the rate of rotation of the bounding surface increases (equation (3.21)) which in turn leads to increase in the plastic modulus thereby increasing the stiffness of the clay. By analyzing this one step further, it can be understood that the model tends to underestimate the strength of the clay without any rotational hardening (C = 0).

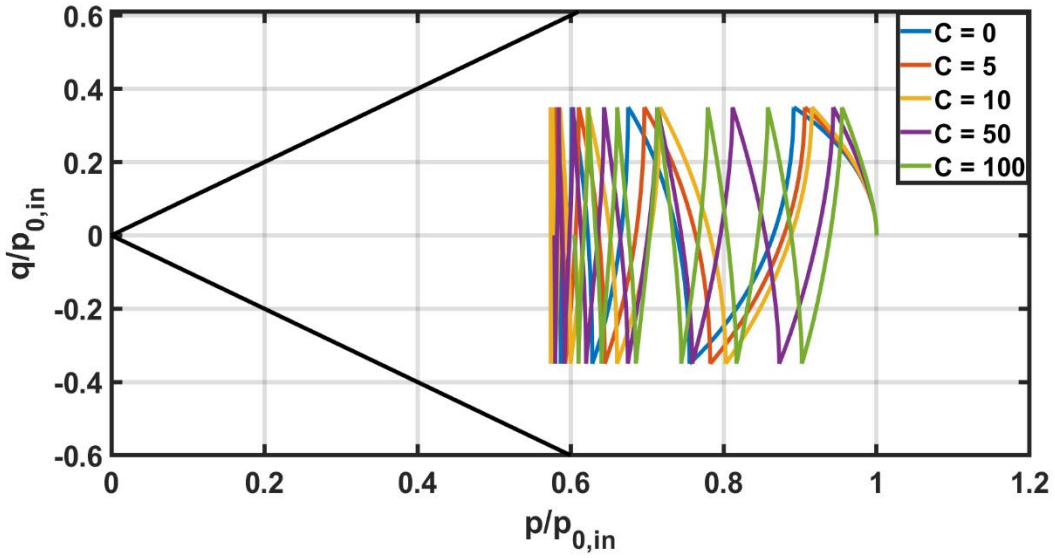

(a)

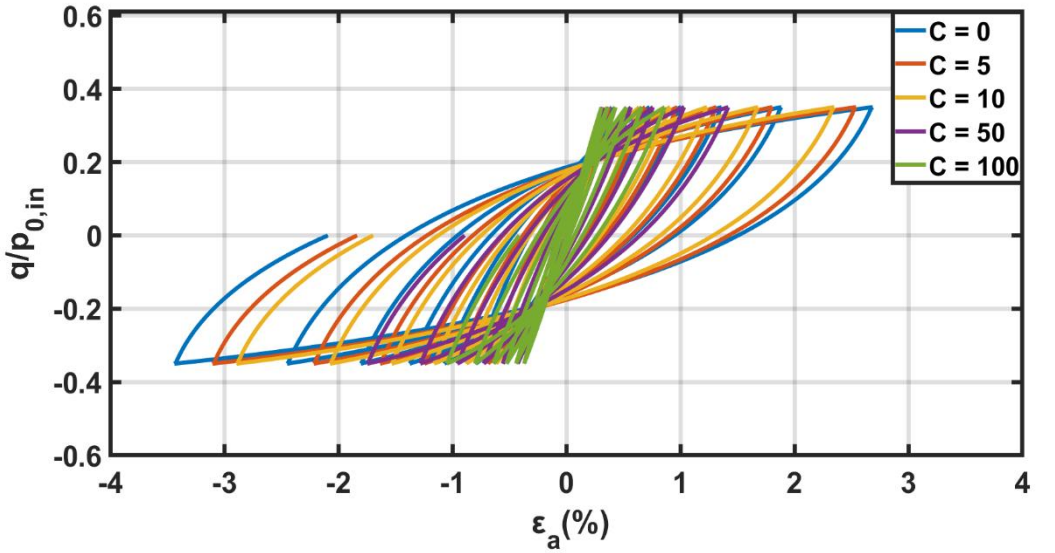

(b)

Figure 4.17 : (a) stress-path , (b) stress-strain response of the model for six cycles of undrained triaxial cyclic loading with varying values of C.

Under the influence of cyclic loading, with increase in the value of C, the rate of migration of the stress path towards origin decreases and also results in lower rate of generation of strains which complies with the literature reviewed in section 2.1.3 that the rate of accumulation of plastic strains and pore water pressures are directly related.

4.2.2.4 Analysis with variation of the shear modulus formulation

For checking the influence of shear modulus on the response of the model, undrained monotonic and cyclic (in this case 10 cycles of loading) triaxial tests were simulated. Constant shear modulus values ranging from 1000 kPa to 25000 kPa have been employed and the obtained results are shown in the figure below. The red dotted line indicates the response of the model with the formulation of shear modulus as per equation (3.4) which is based as per classical elasticity theory with constant Poisson's ratio.

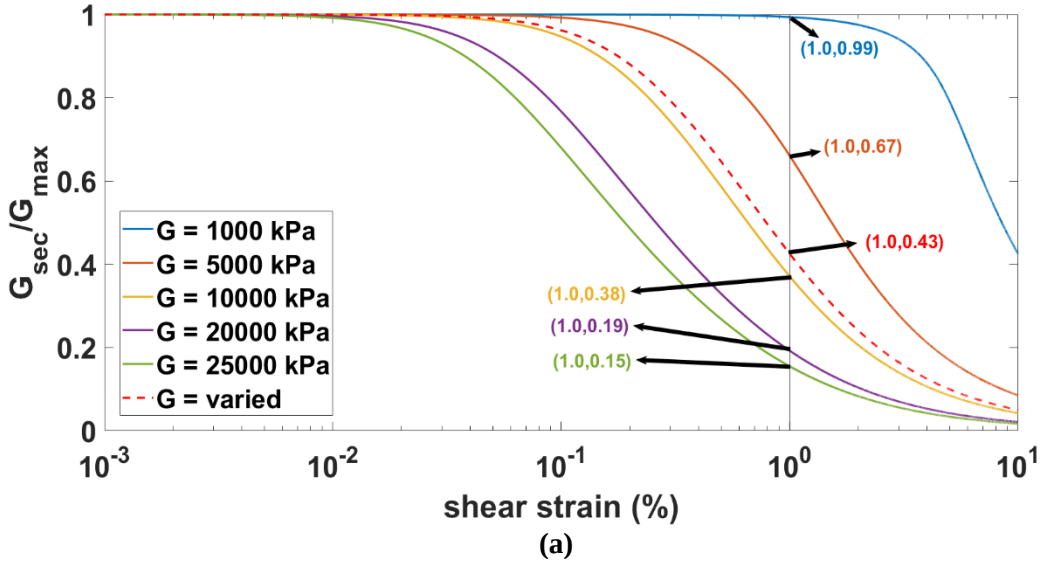

(a)

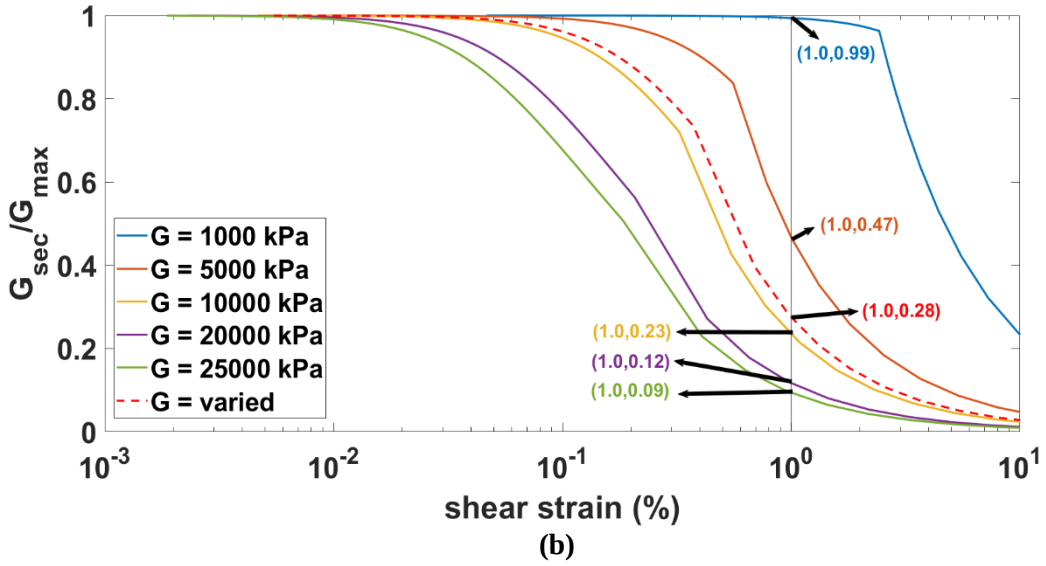

(b)

Figure 4.18 :Shear modulus degradation curves with the shear strain levels, (a) monotonic loading, (b) cyclic loading with 10 cycles of applied load.

The rate of degradation of shear modulus with shear strain decreases with increase in the initial value of the shear modulus. This observation is in accordance with the literature reviewed in section 2.1.1, which points out that cyclic loading induces pore pressure in clays leading to degradation of the soil structure and thereby leading to faster degradation of the shear modulus with shear strain. For the present case the value of the shear modulus (equation (3.4)) used as per classical elasticity theory lies between 5000 and 1000 kPa. It is quite evident from the above graphs that the rate of degradation of the shear modulus is much higher under the influence of cyclic loading than the monotonic as shown with the arrows at 1% shear strain values.

4.2.2.5 Analysis with changing the initial orientation of the bounding surface 'α'

Performing the sensitivity analysis on 'α' means having an initial stress-induced anisotropy in the clay. Sensitivity analysis is performed on 'α' with the initial preconsolidation pressure (p_0) of 200 kPa. In order to have consistency in comparison of the results, the initial stress point is chosen at (133.33,0) which represents an over consolidation ratio of 1.5 such that even with initial rotation of the bounding surface, the chosen stress point lies on or inside the bounding surface.

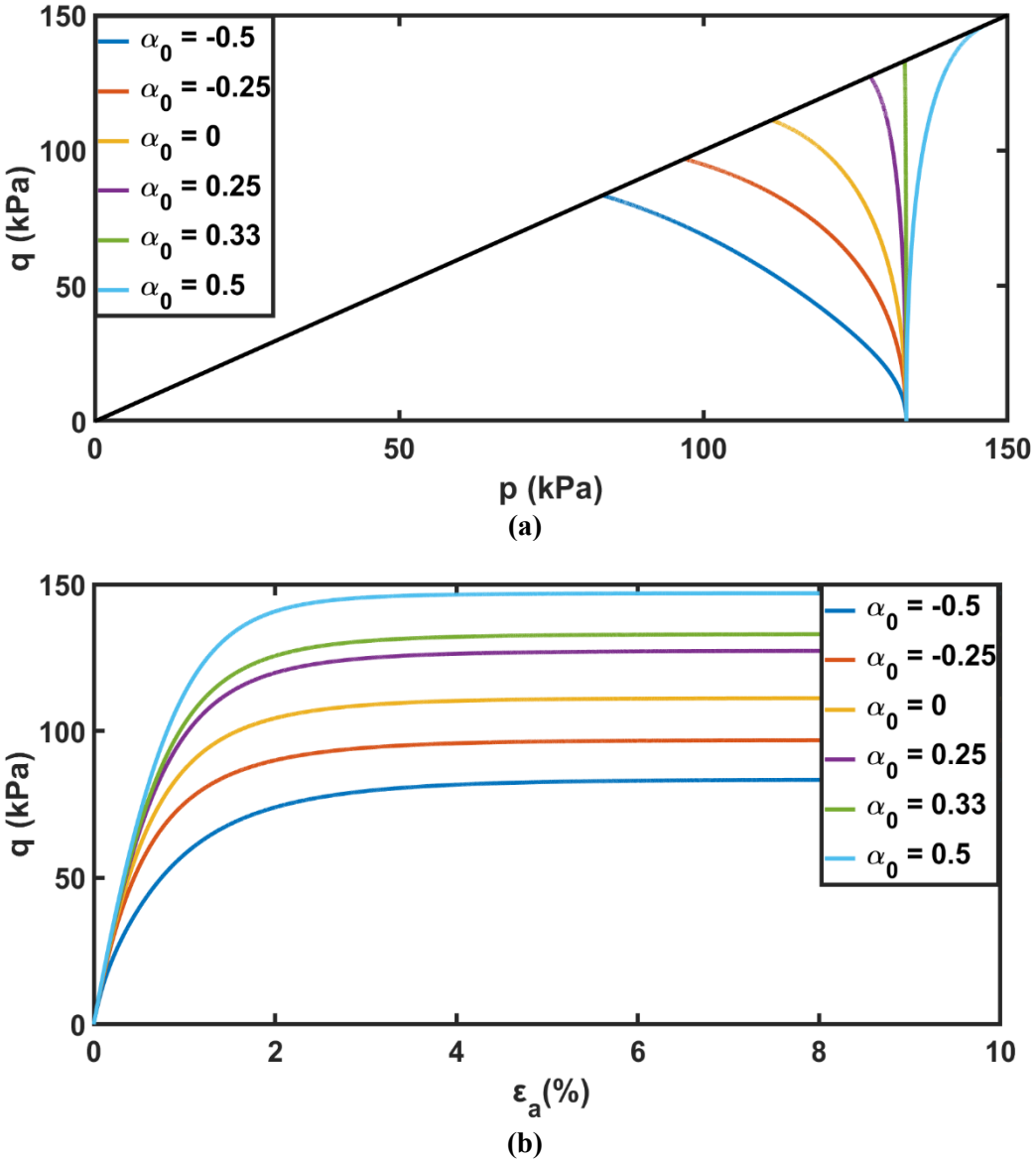

Figure 4.19 : Sensitivity analysis on initial value of 'α' for undrained monotonic loading, (a) stress-path, (b) stress-strain response of the model.

Increasing the value of 'α' from '-0.5' to '0.5' leads to decrease in ultimate strength of the clay. Though the initial OCR is chosen to be 1.5, there is a gradual change of material response from a decrease in the volumetric stress to an increase in the volumetric stress. This is suggestive of the material response changing from a contractive to a dilative state. The special case when 'α' is equal to 0.33, the stress path is a constant volumetric stress curve which happens because the image stress projected onto the bounding surface lies on the critical state line and no further volumetric strains are produced in this case, thereby the bounding surface too stops evolving. In terms of stiffness response, from part (b) of Figure 4.19 it is evident that the stiffness of the clay increases with increase in 'α'. The respective rotation of the bounding surface with evolution of stress path is presented in Appendix-IV.

4.3 Summary

This chapter presented the procedure for implementing the constitutive model in MATLAB. Thus implemented code has been verified against the computational results presented in Seidalinov (2012,2013). Subjected to isotropic consolidation, sensitivity analysis was performed on the specific model constants pertaining to rotational hardening of the bounding surface. It was found that increasing

the value of the parameters such as bound for evolution of anisotropy (N), rate of evolution of anisotropy (C), initial orientation of the bounding surface (α_0) tend to increase the strength and stiffness response of the model. Particularly by increasing the initial orientation of the bounding, the response of the model gradually changed from contractive to a dilative state. Furthermore, when comparing the sensitivity analysis by increasing the shear modulus, the model fairly justified the concept of higher rate of degradation of shear modulus with increase of shear strains. Along the similar lines, the model also predicted higher degradation of shear modulus in the case of cyclic loading as compared to monotonic loading.

Chapter 5 : Validation of the model with experimental results on kaolin clay

This chapter discusses the validation of the model with the experimental results for kaolin clay database from Wichtmann (2018). Firstly the calibration of the model parameters is carried out following the stepwise procedures suggested by Seidalinov (2012). Since the kaolin samples used in the testing procedures have been reconstituted, the parameters affecting the structuration have been set to the destructured values i.e initial isotropic structuration factor (S_i) is set to '1' and the rate of destructuration 'k_i' is set to '0'. Other model parameters and their respective determination has been sequentially described below.

Compression index (λ) and swelling index (κ) : From the oedometer test provided in Wichtmann (2018), λ and κ have been found to be 0.223 and 0.045 respectively.

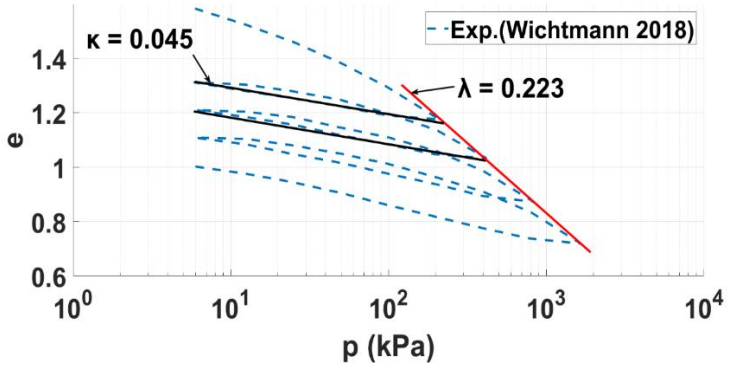

Figure 5.1 : Void ratio versus axial stress graph showcasing the compression and swelling index.

Poisson's ratio (ν) : Calibration of ν is generally based upon K_0-consolidation test followed by K_0-unloading stress path. In the present case due to the lack of such experimental data, ν = 0.33 has been taken from Tafili & Triantafyllidis (2018) which used the data from Wichtmann (2018) in their research.

Critical state ratio in compression (M_c) and extension (M_e) : Monotonic undrained triaxial compression and extension tests are needed to find the values of M_c and M_e. Since the data for undrained triaxial extension test is not available, the figures showing the failure lines in monotonic compression and extension test have been used as a reference to find the critical state ratios. To do that, the data has been digitalized using WebPlotDigitizer (2019) and the corresponding value of M_c and M_e have been found to be 1.0 and 0.73 respectively.

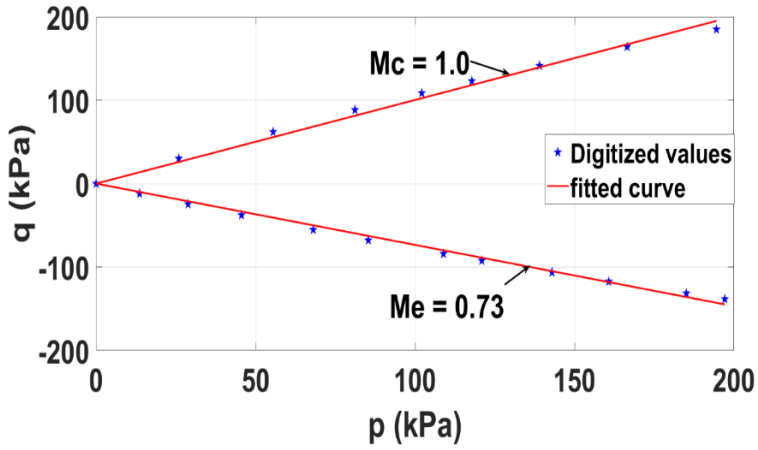

Figure 5.2 : Critical state values in compression and extension by fitting the curve based on digitized values of data from Wichtmann (2018).

The critical state friction angle in compression (φ_c) shall be used for the calibration of 'x', which is found to be 25.37^0 as per equation (5.1).

$$M_c = \frac{6\sin(\varphi_c)}{3-\sin(\varphi_c)} \tag{5.1}$$

Peak stress ratio on bounding surface (N) : Calibration of N would require the availability of undrained triaxial extension test on K_0-consolidated clay, but such data is not available. So N is calibrated along with the rotational hardening parameter 'C' below.

Saturation limit of anisotropy (x) : Calibration of x[13] is based on the formulation provided by Dafalias et al., (2006), for the case of K_0-loading path as follows,

$$x = \frac{2\eta_{k_0}\varepsilon\left(1-\frac{\kappa}{\lambda}\right)}{B\varepsilon\eta_{k_0}{}^3+\eta_{k_0}{}^2+\left[2\left(1-\frac{\kappa}{\lambda}\right)-BM_c{}^2\right]\varepsilon\eta_{k_0}-M_c{}^2}; B=-\frac{2(1+\nu)}{9(1-2\nu)}\frac{\kappa}{\lambda} \tag{5.2}$$

Where, $\eta_{k_0}=3(1-K_0)/(1+2K_0)$ and K_0 is the earth pressure coefficient at rest obtained from Jacky's equation as $K_0=1-\sin(\varphi)$. ε here is the ratio of total strain rate obtained by dividing the total volumetric strain rate to the total deviatoric strain rate as $\varepsilon=\dot{\varepsilon}_v/\dot{\varepsilon}_q$. The value of ε is 3/2 for K_0-loading path. By substituting the values of $\lambda = 0.223$, $\kappa = 0.045$, $\nu = 0.33$, $M_c = 1.0$, $\varphi = \varphi_c = 25.37^0$, the value η_{k_0} is found to be 0.6 and that of x[14] from equation (5.2) is 1.6.

Rate of evolution of anisotropy (C) : Calibration of C is usually based on the undrained triaxial extension test on K_0-consolidated clay, in the absence of which undrained triaxial compression test on isotropically consolidated clay is used. Prior presence of other parameters is required for the calibration of C. Since it was already discussed that N has to be calibrated in tandem with C, the dual calibration of C and N together is shown in Figure 5.3. A point to be noted is that the range of C is between 3-20 as per Dafalias et al., (2006). In case of N, the lesser the value of N compared to M_c the higher the amount of softening reproduced by the model. In order that softening is only produced during compression but not in extension, Papadimitriou et al., (2005) suggested the limits for N as $M_c > N \geq M_e$. In the data sets provided in Seidalinov (2012), the value of N was chosen to be lesser than M_c and M_e when there is lack of experimental data to calibrate 'N'.

[13] There is a misprint in the formulation of 'x' in Seidalinov (2012)
[14] This constant x is an increasing function of K_0

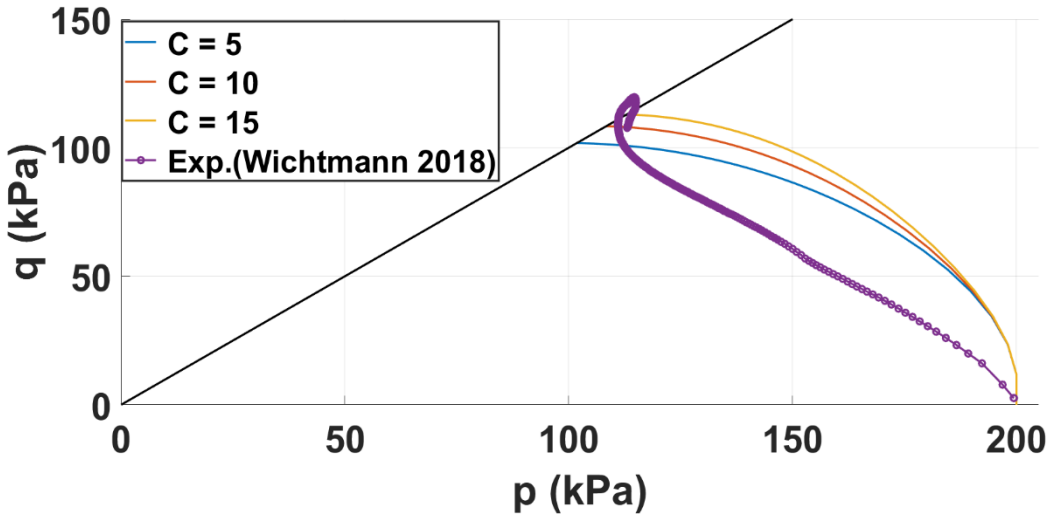

(a) Stress-path with N = 0.75.

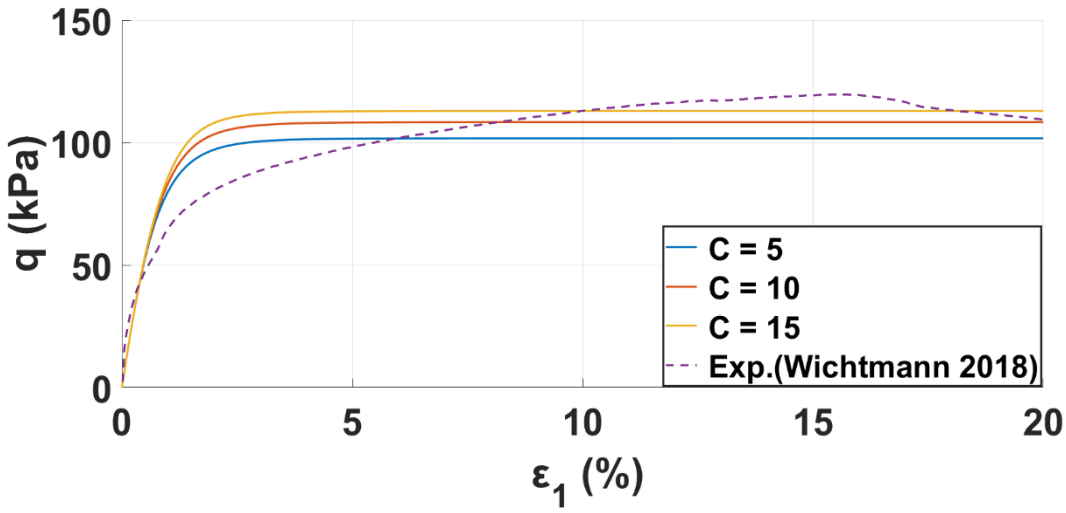

(b) Stress-strain response with N = 0.75.

Figure 5.3 : Calibration of N and C parameters based on the data from Wichtmann (2018).

Based on the knowledge of sensitivity analysis performed on C and N parameters in section 4.2.2, N parameter has been varied from 1.0 to 0.6 and C parameter has been varied from 5-150 to check for the model performance in reproducing the experimental results. An overview of the obtained stress-path and stress-strain response with different values of C and N are presented in Appendix-II. It has been observed that the model was not able to reproduce the experimental stress path. Instead, the stiffness response of the model is comparatively higher than that of the experimentally observed results. After looking at various permutations and combinations of C and N, C = 5-15 and N = 0.75 gave a reasonable match of the results qualitatively as seen from Figure 5.3. By considering these values, a further attempt to calibrate the parameter was done by changing the initial stress-induced anisotropy (α_0) within the model.

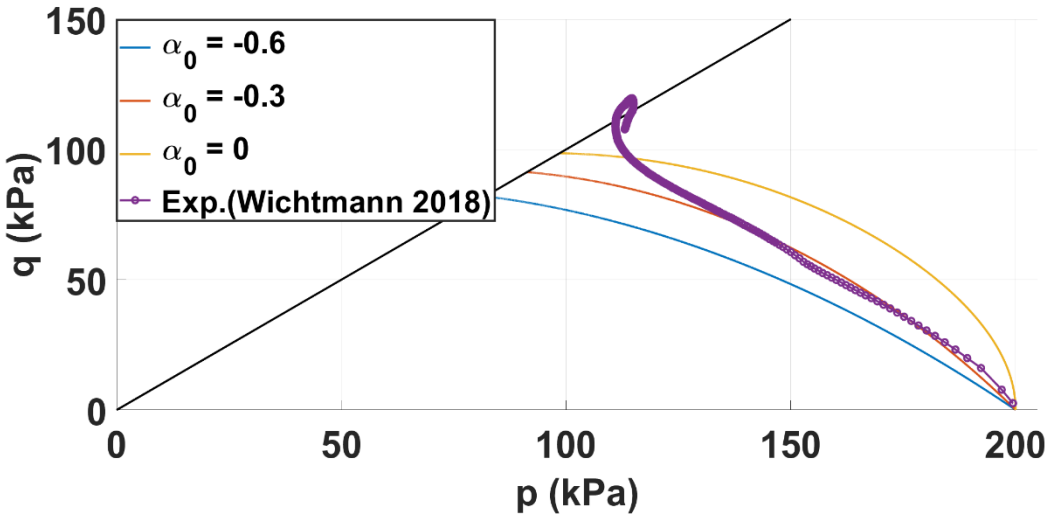

(a) Stress-path with N = 0.75 and C = 5.

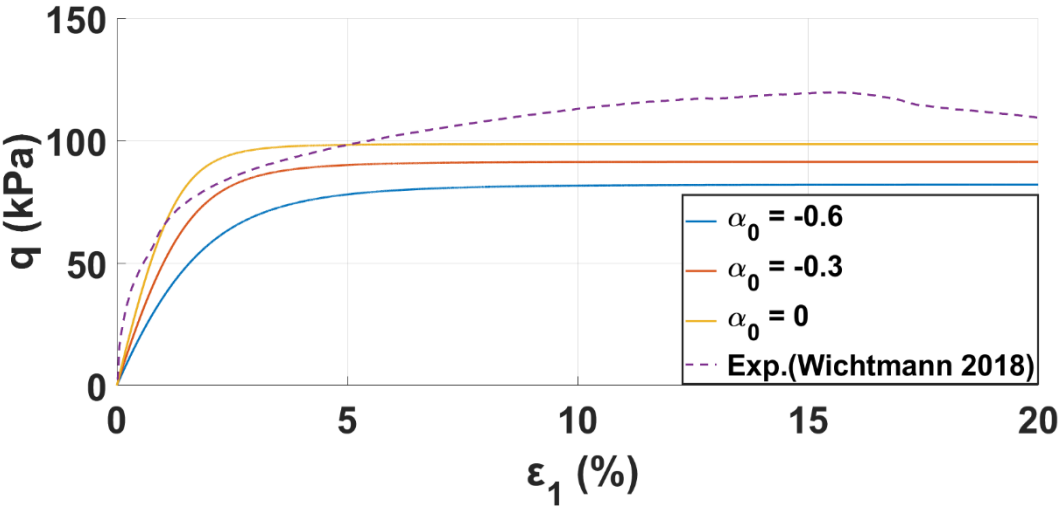

(b) Stress-strain response with N = 0.75 and C = 5.

Figure 5.4 : Calibration of the initial stress-induced anisotropy in the model.

Even by changing the initial stress-induced anisotropy, a comprehensible match of the experimental results was not reproduced by the model. Yet, it can be observed from Figure 5.4 that with N = 0.75, C = 5 and α_0 = -0.3, there was a reasonable match on the stress path till a deviatoric stress level of 75 kPa and a comparable stress-strain response till an axial strain level of 3%. With a higher value of initial stress-induced anisotropy, the model resulted in a much softer response. Similarly, with a lower value of initial stress-induced anisotropy, model gave a stiffer response. So based on the analysis thus performed, the aforementioned parameters are chosen for further analysis.

By analyzing the experimental stress path of the kaolin clay it can be deduced that right from the onset of loading, there is coupling between volumetric and deviatoric strains. So reproducing such behaviour could be only be possible by having the dependence of stress path on both the volumetric and deviatoric strains right from the commencement of the loading. The possible physical meaning behind such behaviour is the presence of anisotropy in the kaolin clay. Such intrinsic anisotropy of the kaolin clay due to its geological history is termed as inherent or fabric anisotropy (Graham & Houlsby, 1983; Anandarajah & Kuganenthira, 1995).

In the present model formulations, at the beginning of the loading the stress path is governed by the isotropic elastic stiffness matrix as seen in equation (4.3). In order for the model to reproduce the experimental stress path results as seen in part (a) of Figure 5.3 and Figure 5.4, this elastic stiffness matrix must be modified. The modified elastic stiffness matrix in order to account for the fabric anisotropy as suggested by Graham & Houlsby, (1983) is as follows,

$$\begin{Bmatrix} \dot{p} \\ \dot{q} \end{Bmatrix} = \begin{bmatrix} K^* & J \\ J & 3G^* \end{bmatrix} \begin{Bmatrix} \dot{\varepsilon}_v^e \\ \dot{\varepsilon}_q^e \end{Bmatrix} \tag{5.3}$$

Compared to the isotropic stiffness matrix as seen in equation (4.3), K^*,G^*, J are the modifications introduced to account for anisotropic behaviour. By incorporating such fabric anisotropy in the elastic stiffness matrix, Tafili & Triantafyllidis (2018) were able to successfully reproduce the behaviour of kaolin clay (Wichtmann 2018) under monotonic loading conditions.

Initial hardening parameter (h_0) : The 'h_0' parameter is calibrated based on the initial cycles of loading. So for this purpose, first three cycles of undrained cyclic triaxial tests with a cyclic shear stress of 70 kPa, pre consolidation pressure of 200 kPa has been simulated.

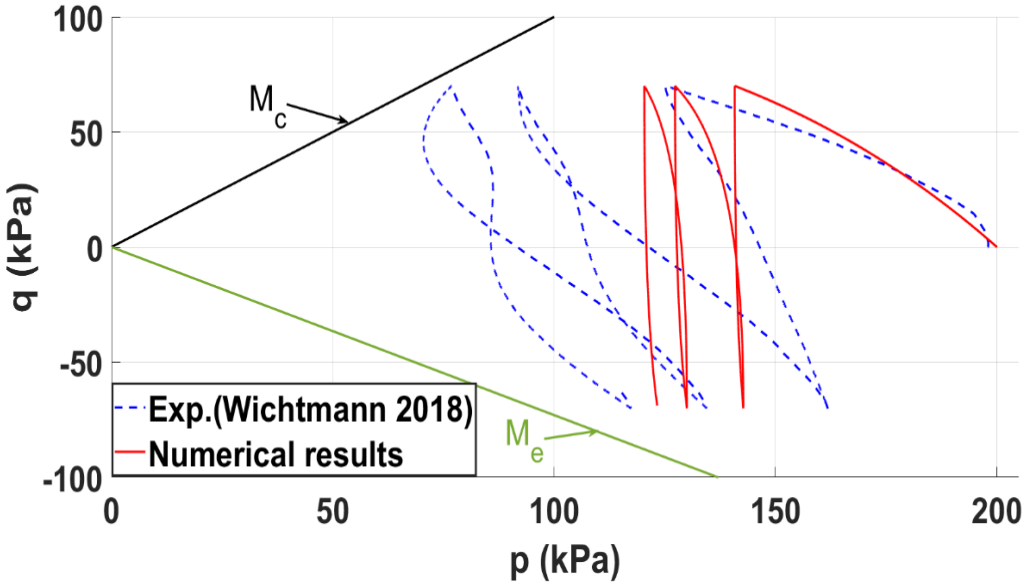

Figure 5.5 : Development of stress path with an initial stress-induced anisotropy(α_0 = -0.3) and h0 = 100.

It can be observed from Figure 5.5 that, when the increment of stress is directed towards the critical state line in extension (M_e), there is nominal change in the development of volumetric stress. On the contrary there is considerable development of stress path when the stress path is directed towards the critical state line in compression (M_c). To interpret such response of the model, a closer look at the evolution of the bounding surface and the definition of the stiffness is required. Firstly due to an initial stress-induced anisotropy in the model, the bounding surface is tilted towards the M_e line. During the first quarter cycle of loading the bounding surface mildly rotates owing to the evolution laws as seen from section 3.4. Due to this reason even at the end of the first quarter cycle of loading the bounding surface is still titled towards the M_e line. To explain the development of the stress-path, it is important to look at the definition of stiffness in the model (section 3.5) which is related to the Euclidian distance between current stress point and the image point. Since the bounding surface is titled towards the M_e line, when the stress increment is directed towards the M_e line (second and third quarter cycles of loading), the Euclidian distance is relatively small leading to lesser development of strains and stresses.

On the contrary when the stress increment is directed towards the M_c line (fourth and fifth quarter cycles of loading), the Euclidian distance is relatively big leading to higher development of strains and stresses. Such response of the model continues for the subsequent cycles of loading which do not reproduce the experimental behaviour of the kaolin clay qualitatively.

In order to avoid such improper development of stress-path and stress-strain response, it was decided to set the initial value of stress-induced anisotropy to zero and subsequently C = 10 and N = 0.75 were chosen for further analysis based on the results matched at the critical state as seen in Figure 5.3. By doing so, for the present analysis it is taken into consideration that the model seems to over-predict volumetric stress for major part of the stress-path traversed.

A trial and error method has been followed to arrive at a 'h_0' value of 100.

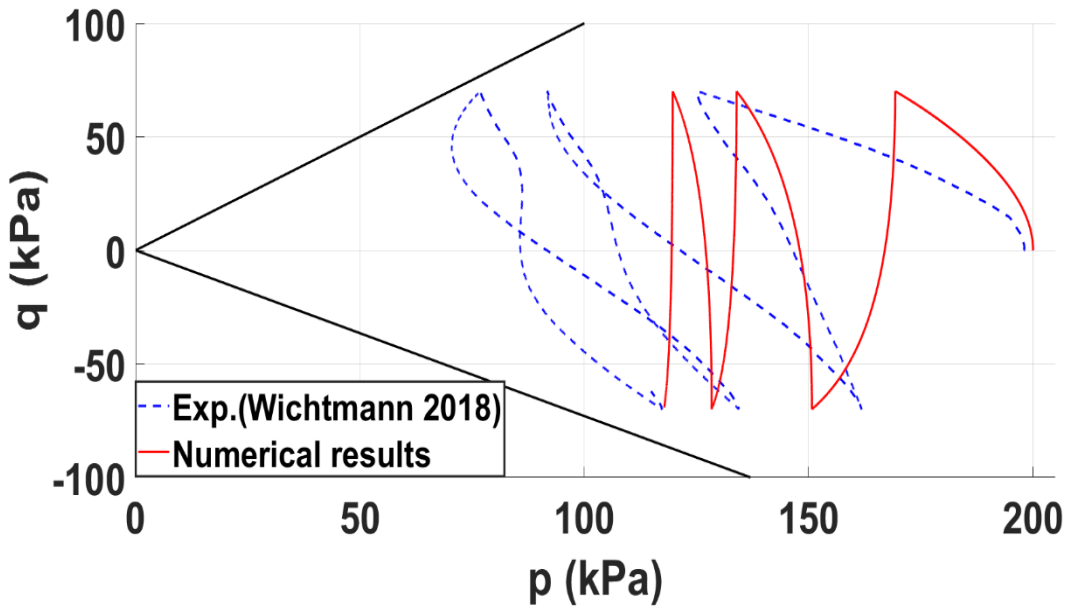

Figure 5.6 : Calibration of h_0 value by using experimental data for the first three cycles of undrained cyclic triaxial loading

The stress path from the experimental results are inclined towards the critical state line in compression which has a comparatively higher value (M_c = 1.0) than the critical state value in extension (M_c = 0.73). From Figure 5.6 it can be observed that only on the extension side of the stress space, the results are a close match whereas the results on the compression side of the stress space have been highly compromised while calibrating the value of 'h_0'. Reason for this compromise is attributed to the way of calibration of 'C' and 'N' parameters in which a major compromise on the stress development in observed.

Rate of damage evolution (a_d) : Once the 'h_0' parameter is calibrated, 'a_d' parameter can be calibrated in a similar trial and error procedure but this time using a stress-strain response.

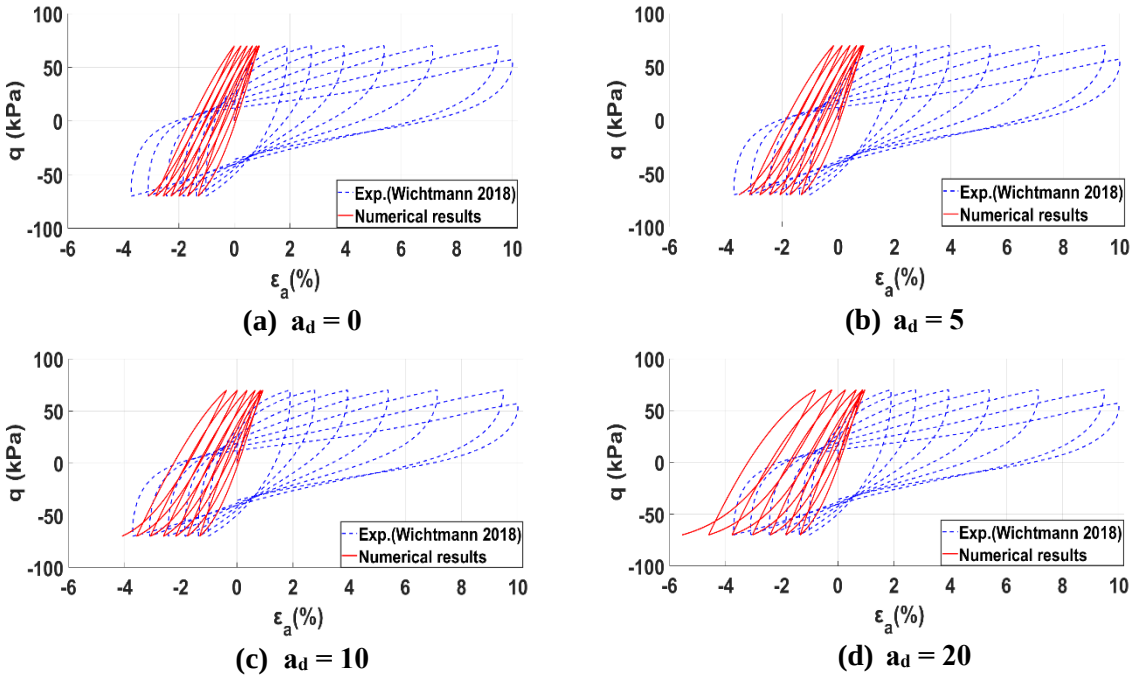

Figure 5.7 : Calibration of a_d parameter based on experimental data for undrained cyclic triaxial loading

Clearly the results obtained from Figure 5.7 do not show any kind of qualitative match with the experimental stress-strain response. Moreover with the increase of 'a_d' parameter, the stress-strain response tends to favor the negative axial strain direction (extension side). So for the computations hereafter, the value of 'a_d' is chosen to be 5 based on the proximity of the peak values of numerical and experimental results on the negative axial strain direction.

A bias in the development of plastic strains towards the extension side of the model is observed. This might be because of the way in which the stiffness is defined in the model. The soil stiffness in the model is related to the distance between the current stress state and the image stress on the bounding surface. Since the critical stress ratio in extension (M_e) is smaller than the critical stress ratio in compression (M_c), under the same stress level there is unbalance between the strains generated in compression and extension. This is the reason behind accumulation of strains on the extension side. One other reason for the higher accumulation of the plastic strains in the extension side is because once the plastic volumetric strains stop accumulating, the rotation of the bounding surface stops. Thus stopped bounding surface is not exactly symmetric with respect to the volumetric stress axis but might be skewed on either side which means that there is some constant stress-induced anisotropy present in the model. For this reason the development of the shear strains can tend to be biased.

The ratio of M_c/ M_e in the present data set is close to 1.37, but in all the data sets provided in Seidalinov (2012), the ratio of the critical state lines in compression to extension were close to unity. This can explain the reason why there has not been any significant bias in the stress-strain response reported by Seidalinov (2012). This can mean that a change is the flow rule might help in better prediction of the stress strain response.

Based on the calibration of the parameters, the finalized parameters for the kaolin clay from the database provided by Wichtmann (2018) are listed out in Table 5.1.

Table 5.1 : model parameters for reconstituted kaolin clay (Wichtmann 2018)

Category	Model constant	Symbol	value
Elasticity	Swelling index	κ	0.045
	Poisson's ratio	ν	0.33
Critical state	Compression index	λ	0.223
	Critical state ratio in triaxial compression	M_c	1
	Critical state ratio in triaxial extension	M_e	0.73
Bounding surface	Peak stress ratio on bounding surface	N	0.75
	Initial hardening parameter	h_0	100
	Rate of damage evolution	a_d	5
Rotational hardening	Rate of evolution of anisotropy	C	10
	Saturation limit of anisotropy	x	1.6
Destructuration	Rate of destructuration	k_i	0

With the obtained parameters, the model is validated for the cyclic loading of kaolin clay under the influence of stress amplitude, initial pressure, over consolidation ratio (OCR) and strain controlled loading. In section 4.2.1.2, stagnation of the stress path with increase in number of loading cycles is observed (OCR ≈ 2), taking this into account, validation has been carried out on limited number of cycles of loading which will be specified in the respective sections below.

5.1 Stress cycles – Variation of amplitude of loading

Wichtmann T, (2018) performed the undrained cyclic triaxial tests with an initial mean pressure of 200 kPa and stress amplitudes varying between 30-70 kPa. In the present analysis, stress amplitudes of 50,60 and 70 kPa have been chosen wherein the number of cycles for failure in these cases did not exceed 35. In order to capture the behaviour of the kaolin clay in the initial cycles of loading and also foreseeing that the stress path in the model will stagnated after a certain number of cycles, 10 cycles of loading[15] was chosen to be appropriate for validating the results.

[15] In case of 70 kPa stress amplitude, data was available for only 7 cycles of loading.

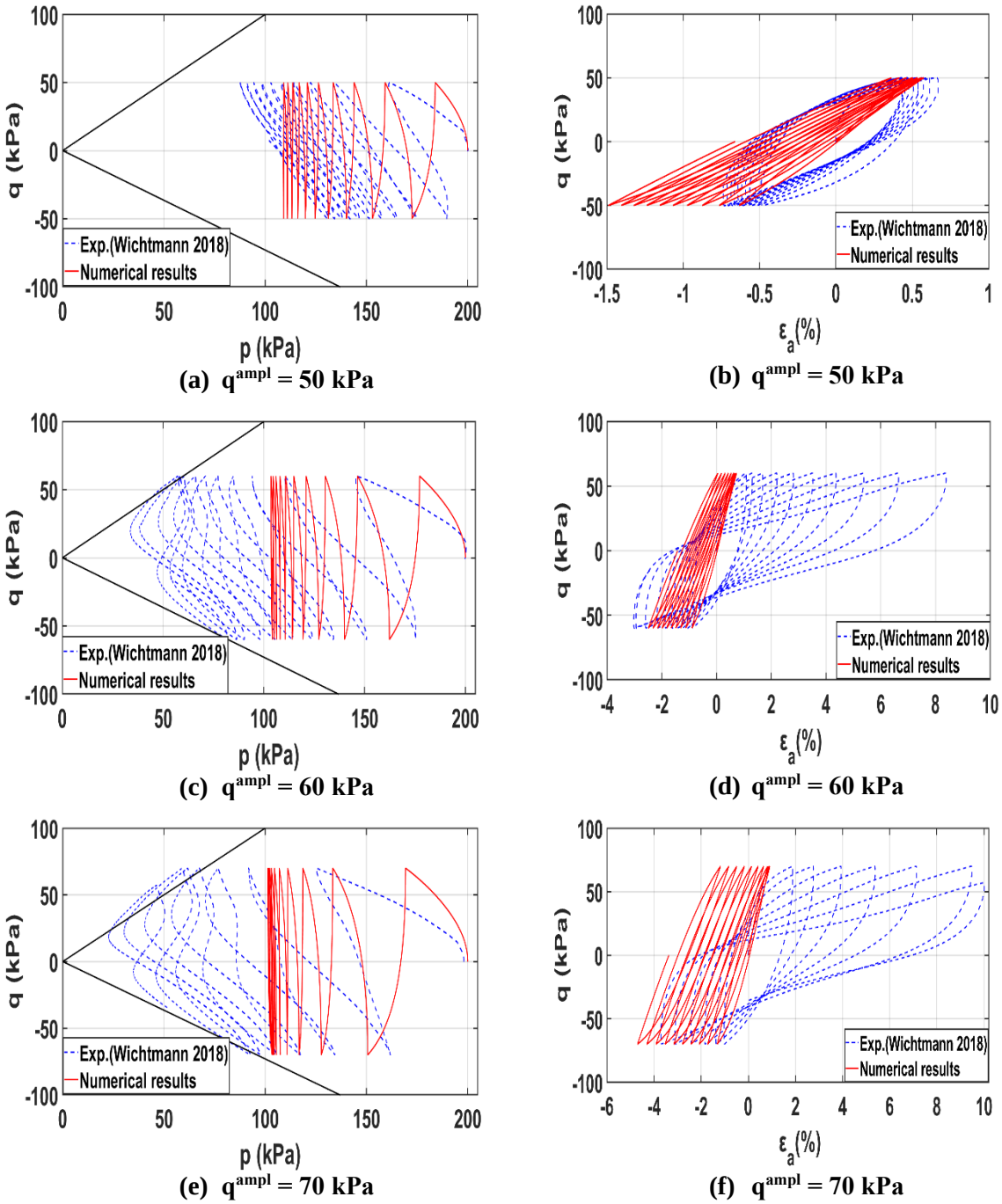

Figure 5.8 : Comparison of model and experimental results for varying cyclic stress amplitude (csa). (a-b) csa = 50 kPa, (c-d) csa = 60 kPa, (e-f) csa = 70 kPa.

The experimental stress-paths from Figure 5.8 parts (a), (c) and (e) suggests that with increase in stress amplitude, there is faster accumulation of pore water pressure leading to rapid decrease in the volumetric stress and thereby leading to early failure of the kaolin clay with lesser number of loading cycles. In terms of strain development as seen from parts (b), (d) and (f) of Figure 5.8, when the stress levels in the clay reached the critical state lines, higher axial strains start accumulating.

The model can qualitatively capture the faster accumulation of the pore water pressure and development of volumetric stress with increase in the stress amplitude. But due to the limitation of the model, stress path freezes close to 100 kPa volumetric stress and the failure state is not reached.

Freezing of the stress path at an OCR ≈ 2 was touched upon in section 4.2. It is well understood by Seidalinov (2012) that the cause of such stagnation is the non-development of plastic volumetric strains.

This further prevents the evolution of the bounding surface. Analyzing it a step further, it can be understood that even though the plastic volumetric strains stop evolving, the plastic deviatoric strains continue to evolve. Researchers in the past (Wheeler et al., 2003; Karstunen & Koskinen, 2008) have attributed the development of anisotropy not only on plastic volumetric strains, but also on plastic deviatoric strains. If the evolution of bounding surface is dependent on both the plastic volumetric and plastic deviatoric strains, there might be a possibility for evolution of the bounding surface even when the plastic volumetric strains stop evolving. This can in turn lead to further development of the stress path.

Model performance is further evaluated by plotting the strain contour diagrams. For this purpose, double amplitude shear stain has been chosen as a base for plotting the results. Reason being, when the clay material is subjected to one full cycle of loading, double amplitude shear strain represents the complete behaviour of the response of the clay whereas choosing single amplitude shear strain might lead to missing out on important features of clay behaviour.

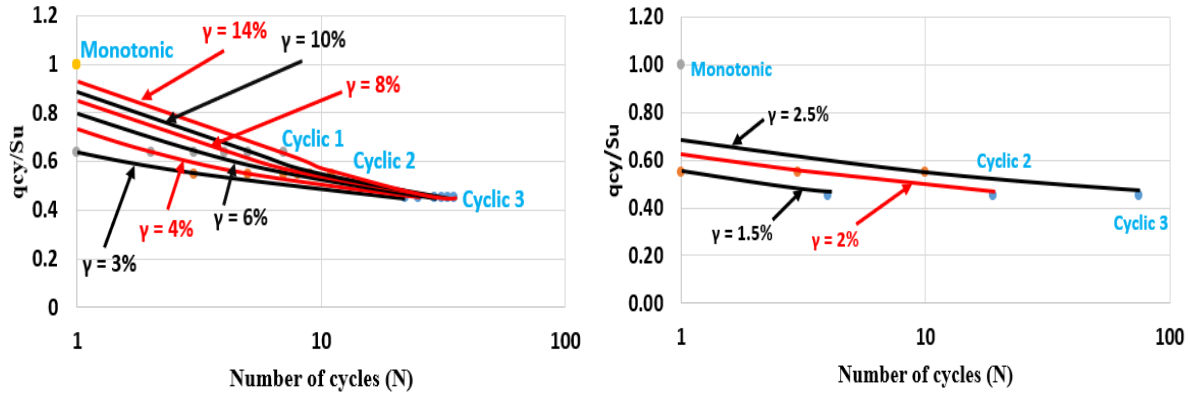

Figure 5.9 : Strain contour diagrams for a) experimental observations (Wichtmann 2018), b) numerical results

Based on the aforementioned explanation, double amplitude shear strain contour diagrams have been generated for the present analysis. As seen from Figure 5.9, part (a) shows the resulting plot from the experimental data provided by Wichtmann (2018) where the strain values in the contour diagrams ranged from 3-14 % and have seen a convergence close to 30-35 cycles of loading. In the case of model performance, since 10 cycles of loading were not sufficient to plot and check the results, only for the purpose of plotting strain contour diagrams, the simulations have been run for close to 80 cycles of loading. Thus obtained results are plot in part (b) of the above figure, it can be seen that the values of shear strain ranged from 1.5-2.5 % and apparently the strain contour diagrams did not converge even at 70 cycles of loading. Such outcome by the model represents the inadequacy in development of strains.

5.2 Stress cycles - Variation of the initial pressure

Wichtmann 2018 performed the experimentation on different initial pressures varying from 50-300 kPa, with a cyclic stress ratio of 0.2. In the present analysis computations have been carried out for initial pressures of 75, 125 and 150 kPa with the cyclic stress amplitude of 15, 25 and 30 kPa respectively for which the maximum cycles of loading for failure is around 140. For other initial mean pressures around 400-1000 cycles of loading were required to reach the failure. Since the chosen constitutive model has a limitation in the development of stress path, choosing the case where lower number of cycles of loading are required to reach failure will give a better prospective to understand the model behaviour. Considering the model performance, computations have been carried out for the first 20 cycles of loading.

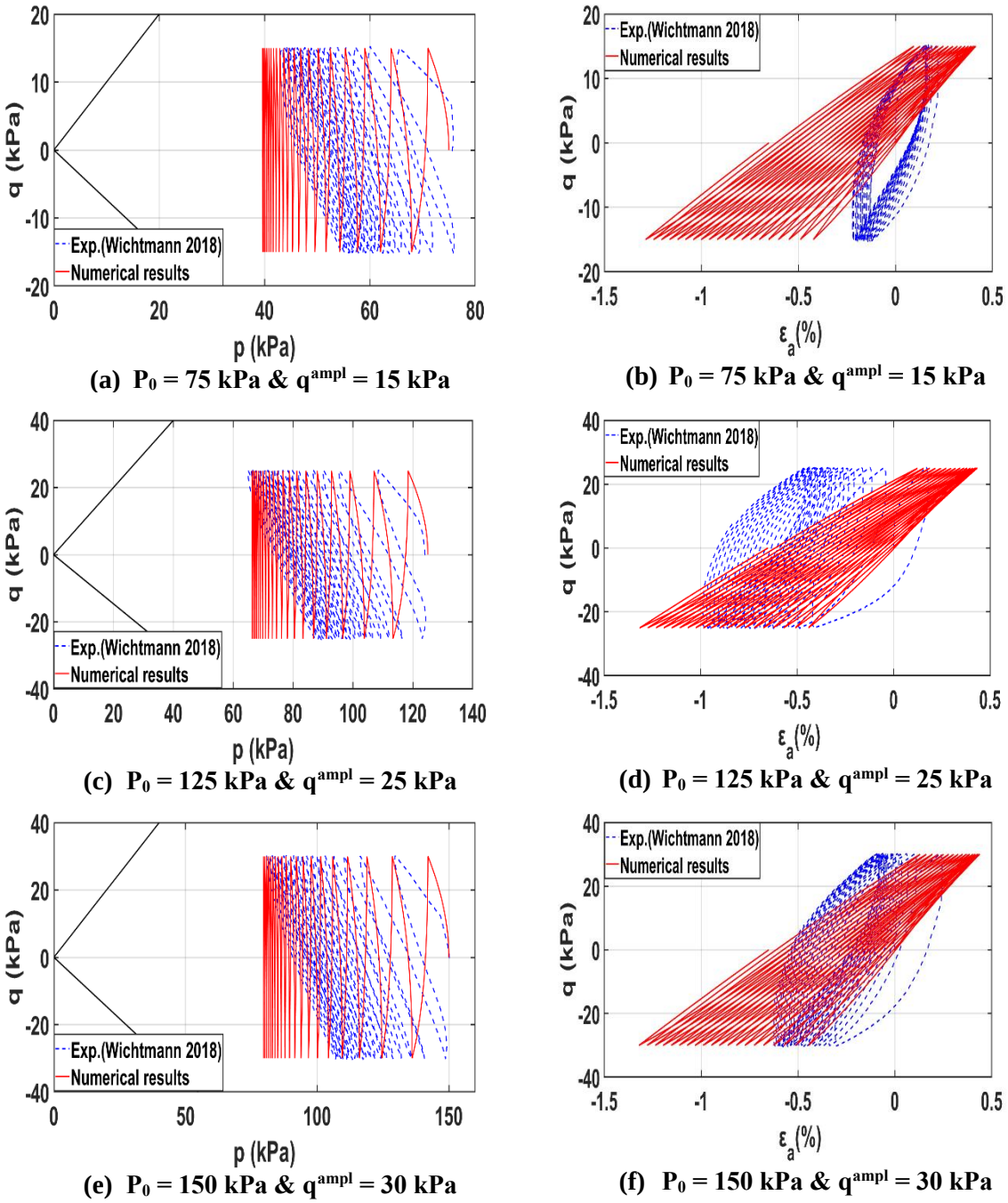

(a) P_0 = 75 kPa & q^{ampl} = 15 kPa **(b) P_0 = 75 kPa & q^{ampl} = 15 kPa**

(c) P_0 = 125 kPa & q^{ampl} = 25 kPa **(d) P_0 = 125 kPa & q^{ampl} = 25 kPa**

(e) P_0 = 150 kPa & q^{ampl} = 30 kPa **(f) P_0 = 150 kPa & q^{ampl} = 30 kPa**

Figure 5.10 : Comparison of model and experimental results for varying initial pressure (p_0). (a-b) p_0 = 75 kPa, (c-d) p_0 = 125 kPa, (e-f) p_0 = 150 kPa.

The experimental results when plotted in their entirety till they reach the failure (Appendix-III) show that the development of the shear strains is relatively spread across either sides of the zero strain axis. Particularly during the final cycles of loading when the stress path of kaolin clay reaches closer to the critical state lines, due to occurrence of dilation, higher values of the shear strains are developed. But when only the initial 20 cycles of loading is considered as in the present case, predominantly negative strains are developed.

The model predicts a much faster degradation of the of the stress path with decrease in the initial mean pressure as seen in part (a) of the above figure. Due to the nature of the model, though it predicts the accumulation of the negative strains, an overestimation of these values is quite evident seen from Figure 5.10 part (b), (d) and (f).

5.3 Stress cycles - Variation of OCR

Experimental analysis carried out by Wichtmann (2018) considered three distinct OCR's namely 1.5, 2.0 and 2.5. These simulations have been carried out with an initial pressure of 100 kPa and cyclic stress ratio of 0.3. In order to have a consistency in comparison of the results, experiments with normally consolidated sample starting from initial pressure of 100 kPa and cyclic stress ratio of 0.2[16] was chosen. Simulations have been carried out for first 20 cycles of loading.

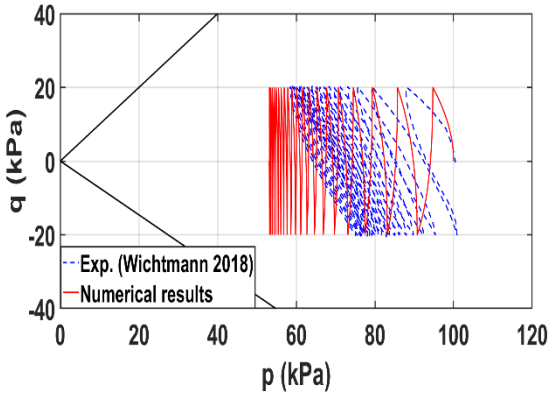

(a) OCR = 1.0

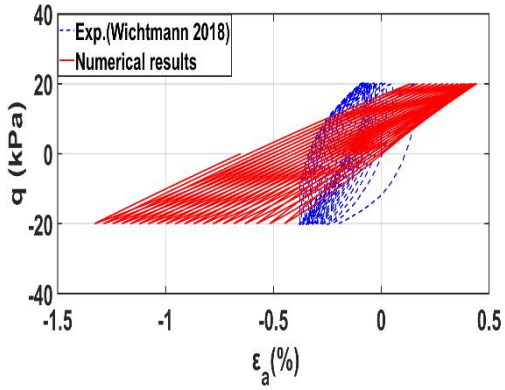

(b) OCR = 1.0

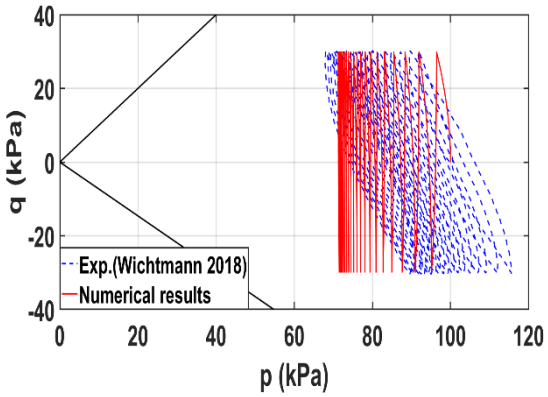

(c) OCR = 1.5

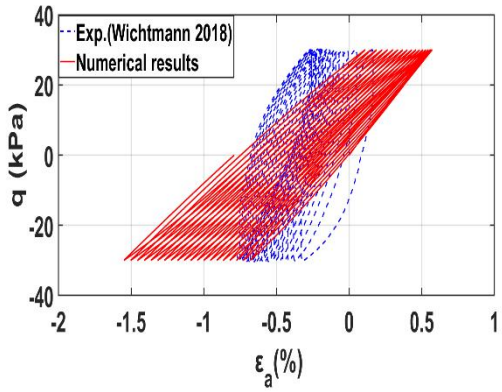

(d) OCR = 1.5

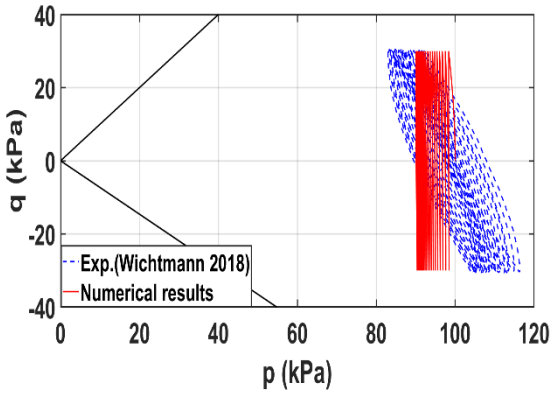

(e) OCR = 2.0

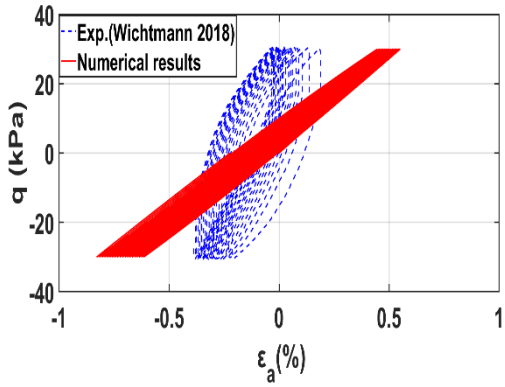

(f) OCR = 2.0

[16] Data for cyclic loading with initial pressure of 100 kPa and cyclic stress ratio of 0.3 was not available. Hence, the best available data was chosen for the comparison purpose.

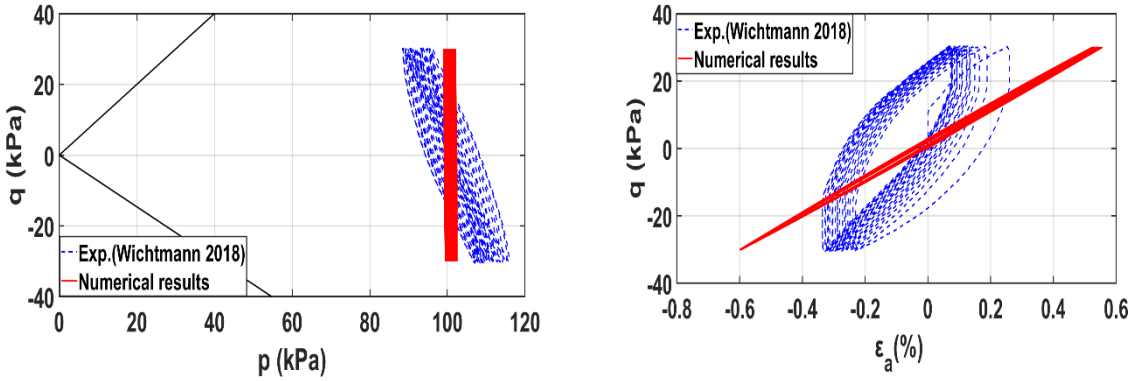

(g) OCR = 2.5 **(h) OCR = 2.5**

Figure 5.11 : Comparison of model and experimental results for varying over consolidation ratios (OCR). (a-b) OCR = 1.0, (c-d) OCR = 1.5, (e-f) OCR = 2.0, (g-h) OCR = 2.5.

As reported by Wichtmann (2018), the response initially overconsolidated (OCR > 1) kaolin clay during the first cycle of loading is completely dilative thereafter all the stress cycles followed a contractive stress-path meaning the evolution of the stress-path is directed towards the origin. For a normally consolidated (OCR = 1) kaolin clay shown in part (a) and (b) of the above figure, a complete contractive stress path is observed from the initial cycle of loading. Also with increase in OCR, the strain development tends to decrease for the chosen cases as seen in above figure. Development of the stress-strain for the normally consolidated clay cannot be compared to the higher OCR stress-strain responses because of the lower cyclic stress ratio in normally consolidated clay.

With decrease in OCR, higher relaxation of the stress path is observed from the model which is evident from the case of normally consolidated kaolin clay. For OCR equal to 1.5 and 2, the response of the model was completely contractive from the first cycle of loading as opposed to the experimental results. In the case where OCR is 2.5, model response was a bit different in the sense that only during the first quarter cycle of loading the response was contractive as shown in Figure 5.12(blue arrows indicate the direction of the stress path during the first cycle of loading), but the consequent cycles of loading have shown a completely dilative response where the direction of the stress path evolution is directed away from the origin. In terms of strain development, the model was qualitatively able to predict the decrease in strain accumulation with the increase in OCR. The reason behind such a stress path development is understood to be because of the evolution laws of the model which are dependent on the critical state ratios (M_c and M_e). It has been reported by Seidalinov (2012) that the stagnation of the stress path occurs when the projected image stress lies on the critical state line. So when the initial stress point is at a overconsolidated state (in this case OCR = 2.5), the stagnation of the stress path is attracted towards the direction where the image stress is more likely to lie on the critical state line. In this case, M_e is smaller than M_c, thereby when the stress increment is directed towards M_c line the stress path will traverse towards origin leading to a compressive behaviour. On the contrary when the stress increment is directed towards the M_e line, the stress path will traverse away from the origin leading to a dilative behaviour.

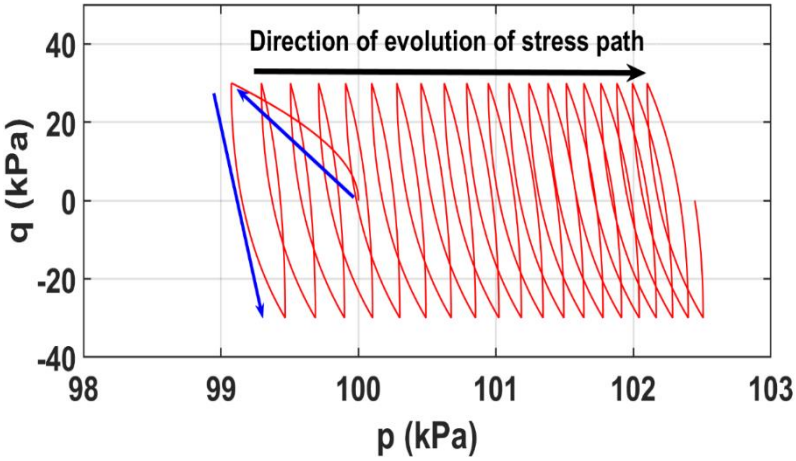

Figure 5.12 : Magnified view of the stress path for OCR = 2.5

Elaborating on the explanation given in the previous paragraph, detailed understanding of the development of the compressive and dilative stress path can be understood from the Figure 5.13. Here an illustration is shown with M_c less than M_e in the stress space. Points 'A' and 'B' represent the intersection of the bounding surface with the critical state lines in compression and extension respectively, when the image stress lies on one of these points, the rate of increase in plastic volumetric strain will become zero and thus the bounding surface stops evolving. Now considering the point X, when the stress increment is directed towards M_c line, the development of the stress path will be attracted towards point A, implying a decrease in volumetric stress (compressive behaviour). Similarly trend is expected to occur when the stress increment is directed towards M_e line . But in the case of stress path originating from point Y, when the stress increment is directed towards M_e line, the stress path will be attracted towards point B, leading to an increase in the volumetric stress (dilative behaviour). Finally considering the case of stress path originating from point Z, stress increment directed towards both the M_c and M_e will produce an increase in the volumetric stress which is essentially a dilative behaviour.

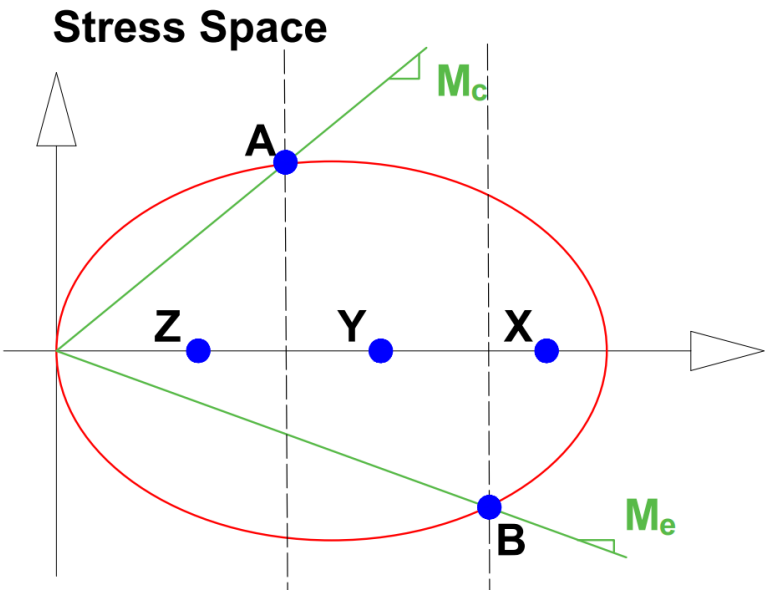

Figure 5.13 : Model figure for illustration of evolution of stress path with the location of initial stress point.

5.4 Strain cycles – Variation of amplitude of strains

Model performance under the influence of different strain amplitudes of loading is analyzed by taking into consideration the experimental observations for three different single amplitude strain namely 1%, 2% and 5%.

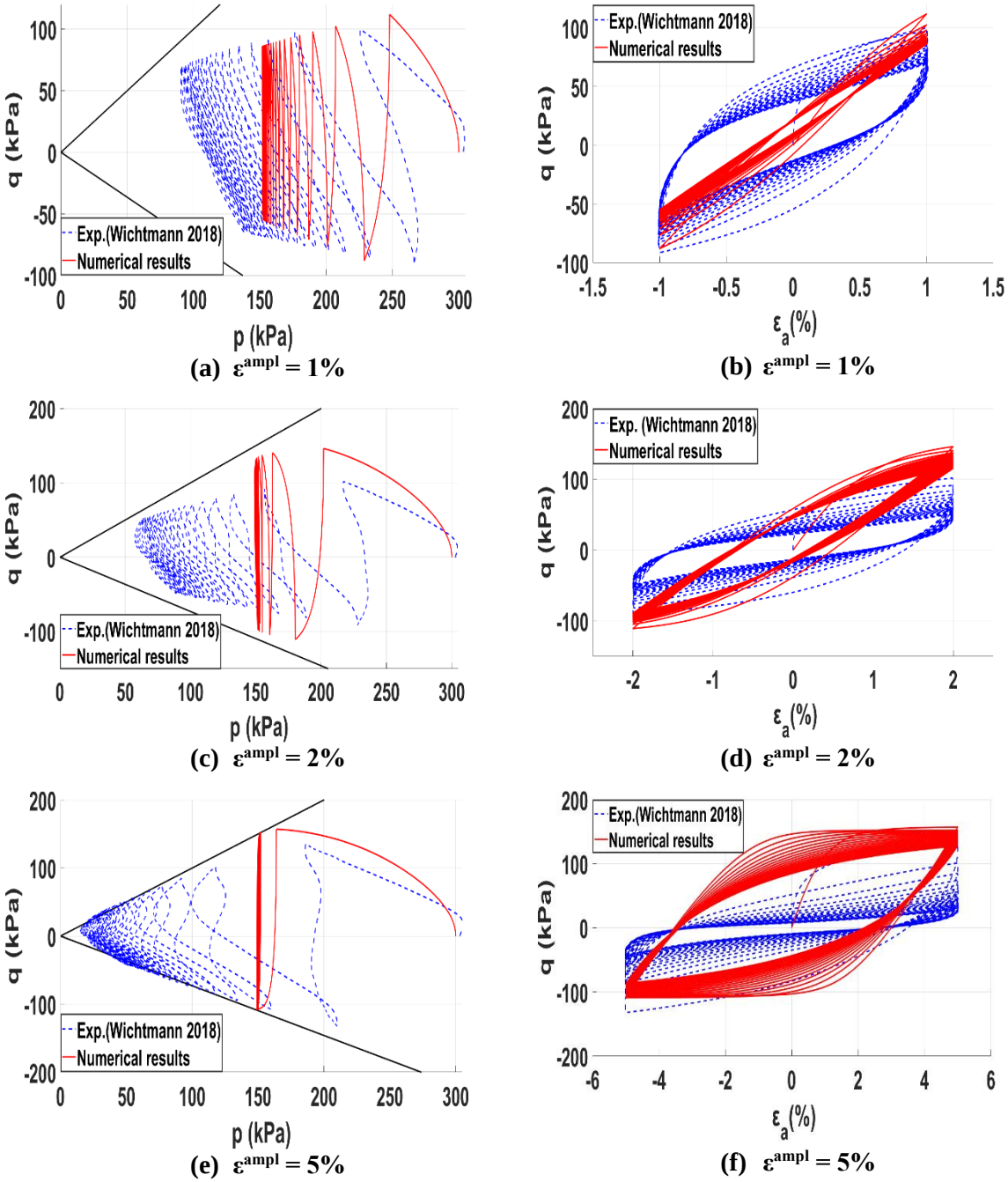

Figure 5.14 : Comparison of model and experimental results for varying strain amplitudes (ε_a). (a-b) ε_a = 1%, (c-d) ε_a = 2%, (e-f) ε_a = 5%

Experimental results reveal that with increase in the amplitude of strain, much lower number of loading cycles are required to reach the failure. Also when considering the behaviour of the kaolin clay in the first 20 cycles of loading as shown in Figure 5.14, the stress path at 5% strain amplitude reached the critical state lines faster while the stress-path with that of 1% and 2% strain amplitude lie well away from the critical state lines. In terms of strain development, with increase in the amplitude of shear strain, the hysteretic damping represented by the area under the hysteresis loop increases.

Numerical results show that the model can qualitatively capture the faster accumulation of pore water pressure and therefore the relaxation of the stress path with increase in the strain amplitude. A point to be noted is that in all the simulated numerical results, the stress path freezes when the OCR ≈ 2 i.e in this case when the volumetric stress is 150 kPa. Increasing in the hysteretic damping with increase in the amplitude of the shear strain was well captured qualitatively by the model.

5.5 Summary

This chapter presents the validation results of the chosen constitutive model against the experimental data on the kaolin clay from Wichtmann (2018). During the process of calibrating the model constants it was observed that stress path of the normally consolidated kaolin clay under the monotonic loading conditions was not reproduced by the model. The reason behind such response of the model has been attributed to the non-consideration of fabric anisotropy in the model formulations. Owing to such performance the model was assessed qualitatively. When the model is subjected to different initial conditions, if not all, certain aspects of the experimental behaviour were qualitatively captured by the model. These include faster rate of accumulation of pore water pressure with increase in the amplitude of cyclic loading, reduction in the rate of development of strains with increase in OCR values, increase in the hysteretic damping with increase in the amplitude of strains. However, with change of OCR there were differences in the development of stress path. Also contrasting results were observed with regard to the development of the stress-strain response with change of amplitude of cyclic loading and initial pressure.

Chapter 6 : Conclusions and recommendations

The research carried out during the course of this study was aimed at investigating the performance of bounding surface SANICLAY model on reproducing the behaviour of kaolin clay under different initial loading conditions. To realize the aforementioned goals the model has been implemented in MATLAB and tested during the course of this study. Following the obtained results and the corresponding discussions in previous chapters, conclusions regarding the ability of model in reproducing the experimental behaviour are presented here. This is followed by the potential recommendations for future research.

6.1 Conclusions

A parametric analysis performed on the model constants revealed the sensitivity of model to parameters such as bound for evolution of the anisotropy (N), rate of evolution of the anisotropy (C) and initial rotation of the bounding surface (α_0) when subjected to isotropic consolidation followed by shearing. The strength and stiffness response of the model increases with increase of the aforementioned parameters. Also the model was able to capture the higher rate of degradation of the shear modulus in the case of cyclic loading as compared to monotonic loading.

Validation of the model against the experimental data on kaolin clay (Wichtmann 2018) gave substantial information to comment on the capabilities and limitations of the model. Firstly, calibration of the initial model parameters revealed that the experimental curvature of the effective stress path of the kaolin clay was not reproduced by the model. Although the combination of different initial parameters along with change of initial stress-induced anisotropy of the model was used to attain reasonable fit under the monotonic loading conditions, the prediction of the cyclic stress path was compromised to a great extent.

Under the influence different initial conditions, the model was able to qualitatively predict some aspects of cyclic behaviour of the kaolin clay. Key findings include the faster rate of accumulation of pore water pressure with increase in the amplitude of cyclic loading, development of lower rate of strains with increase in the OCR values, capturing of higher hysteretic damping with increase of the amplitude of strains.

The model was able to qualitatively predict the development of stress path for normal consolidated clays and lightly overconsolidated clays but for the case of clays with OCR greater then 2.5, contrasting development of stress path was observed. An illustration of this can be seen in Figure 5.12 where the stress path was predominantly dilative in nature whereas the experimental stress path suggested a contractive response as reported by Wichtmann (2018). The reason behind such development is attributed to the definition of the rotational hardening law which is dependent on the critical stress ratios (M_c and M_e).

Strain development was not accurately captured by the model with change of amplitude of cyclic loading and initial pressure. It was observed that higher negative axial strains are generated with increase in number of cycles of loading. Such bias in the development of strains is attributed to the definition of stiffness in the model which is dependent on the distance between the current stress state and its image on the bounding surface. Since the critical state value in extension is smaller than that in the compression, lower stiffness is produced when the stress path is directed towards M_e line leading to generation of higher strains.

6.2 Recommendations

This thesis attempts at validating the bounding surface SANICLAY model with the experimental data on kaolin clay (Wichtmann 2018). Though it was not possible to validate the model quantitatively, the qualitative results have shown promise in reproducing the behaviour of kaolin unto a reasonable extent under specific loading conditions. However, the conclusions listed in this thesis provides opportunities for continuation of the research. Recommendations for the future research are presented in this section.

The present research has shown the limitations of the model in reproducing behaviour of the clays with fabric anisotropy. Such behaviour can be reproduced by modifying the elastic stiffness matrix in the model along the lines of Graham & Houlsby (1983) by having a dependence of the development of stress path on both volumetric and deviatoric strains right from the onset of loading. In other words, having a non-zero off diagonal elements in the elastic stiffness matrix as seen in equation (5.3).

During the process of cyclic loading, when the projected image stress lies on the critical state line, the development of the plastic volumetric strains ceases thereby leading to freezing of the both the bounding surface and the stress path. Coupling both the plastic volumetric and plastic deviatoric strains for the evolution of the bounding surface could be a possible solution for further development of the stress path.

In the scope of research carried out in this thesis, experimental results for one specific clay were used to validate the model. Future research can potentially focus on different clay materials to get a greater insight into the capabilities of the model. In addition, it is recommended to test the model performance in the principle stress space. For example, during the shearing process in direct simple shear test, the orientation of the principle stress directions keep changing, so validating the model performance in the principle stress space can give a detailed picture of the model performance.

Bibliography

Anandarajah, A., & Kuganenthira, N. (1995). Some aspects of fabric anisotropy of soil. *Géotechnique*, *45*(1), 69-81. doi: 10.1680/geot.1995.45.1.69

Andersen, K., Pool, J., & Brown, S. (1980). Cyclic and static laboratory tests on drammen clay. *International Journal Of Rock Mechanics And Mining Sciences & Geomechanics* Abstracts, 18(1), 4. doi: 10.1016/0148-9062(81)90316-8

Azzouz, A. S., Malek, A. M., & Baligh, M. M. (1989). Cyclic behavior of clays in undrained simple shear. *Journal of Geotechnical Engineering*, *115*(5), 637-657.

Bardet, J. & Choucair, W. (1991), 'Linearized integration technique for incremental constitutive equations', *International Journal for Numerical and Analytical Methods in Geomechanics* 15(1), 1-19.

Bea, R. G., Wright, S. G., Sircar, P., & Niedorode, W. F. (1983). "Wave-induced slides in South Pass Block 70, Mississippi Delta." . *Journal of Geotechnical Engineering*, ASCE, 109(4), 499-529.

Boulanger, R. W., & Idriss, I. M. (2006). Liquefaction Susceptibility Criteria for Silts and Clays. *Journal of Geotechnical and Geoenvironmental Engineering*, 132(11), 1413–1426. https://doi.org/10.1061/(asce)1090-0241(2006)132:11(1413)

Brinkgreve, R. (2017), Behaviour of soils and rocks. Lecture notes, TU Delft.

Brinkgreve, R.B.J. & Vermeer, P.A. (1997). Plaxis finite element code for soil and rock analysis-Version 7", Balkema, Rotterdam.

Dafalias, Y. (1986). Bounding Surface Plasticity I: Mathematical Foundation and Hypoplasticity . *Journal Of Engineering Mechanics*, *112*(9), 966-987. doi: 10.1061/ (asce)0733 -9399(1986) 112:9(966)

Dafalias, Y., & Herrmann, L. (1986). Bounding Surface Plasticity. II: Application to Isotropic Cohesive Soils. *Journal Of Engineering Mechanics*, *112*(12), 1263-1291. doi: 10.1061/(asce)0733-9399(1986)112:12(1263)

Anandarajah, A., & Dafalias, Y. (1986). Bounding Surface Plasticity. III: Application to Anisotropic Cohesive Soils. *Journal Of Engineering Mechanics*, *112*(12), 1292-1318. doi: 10.1061/(asce)0733-9399(1986)112:12(1292)

Dafalias YF, Manzari MT, Papadimitriou AG. (2006). SANICLAY: simple anisotropic clay plasticity model. *International Journal for Numerical and Analytical Methods in Geomechanics*, 30(12):1231–1257.

Dafalias, Y., & Popov, E. (1975). A model of nonlinearly hardening materials for complex loading. *Acta Mechanica*, *21*(3), 173-192. doi: 10.1007/bf01181053

Dobry, R. & Vucetic, M. (1987). State-of-the-art report: Dynamic properties and response of soft clay deposits. Proc., *International Symposium on Geotechnical Engineering of Soft Soils*, Mexico City, M. J. Mendoza and L. Montanez, Vol. 2, Sociedad Mexicana de Mecanica de Suelos, Mexico City, 51–87.

Gajo, A., & Muir Wood, D. (2001). A new approach to anisotropic, bounding surface plasticity : general formulation and simulations of natural and reconstituted clay behaviour. *International Journal For Numerical And Analytical Methods In Geomechanics*, 25(3), 207-241. doi: 10.1002/nag.126.

Graham, J. & G. Houlsby (1983). Anisotropic elasticity of a natural clay. Géotechnique 33(2), 165–180.

Hyde, A., & Ward, S. (1986). The effect of cyclic loading on the undrained shear strength of a silty clay. *Marine Geotechnology*, 6(3), 299-314. doi: 10.1080/10641198609388192.

Hyodo, M., Yamamoto, Y., & Sugiyama, M. (1994). Undrained cyclic behaviour of normally consolidated clay subjected to initial static shear stress (Marine Clay). *Soils and Foundations*, 1–11.

Idriss IM, Dobry R, Singh RD. (1978). Nonlinear behavior of soft clays during cyclic loading. *Journal of Geotechnical Engineering*;104(12):1427e47.

Iwan, W.D., 1967. On a class of models for the yielding behavior of continuous and composite systems. *Journal of Applied Mechanics*, ASME 34, 612–617

Kagawa, T. (1992). Moduli and Damping Factors of Soft Marine Clays. *Journal Of Geotechnical Engineering*, *118*(9), 1360-1375. doi: 10.1061/(asce)0733-9410(1992)118:9(1360)

Karstunen, M., & Koskinen, M. (2008). Plastic anisotropy of soft reconstituted clays. *Canadian Geotechnical Journal*, *45*(3), 314-328. doi: 10.1139/t07-073

Krieg, R. (1975). A Practical Two Surface Plasticity Theory. *Journal Of Applied Mechanics*, *42*(3), 641-646. doi: 10.1115/1.3423656.

Lefebvre, G., & LeBoeuf, D. (1987). Rate Effects And Cyclic Loading of Sensitive Clays. *Journal Of Geotechnical Engineering*, 113(5), 476-489. doi: 10.1061/(asce)0733-9410(1987)113:5(476)

Li, L. L., Dan, H. B., & Wang, L. Z. (2011). Undrained behavior of natural marine clay under cyclic loading. *Ocean Engineering*, 38(16), 1792–1805. https://doi.org/10.1016/j.oceaneng.2011.09.004

Liang, R., & Ma, F. (1992). Anisotropic Plasticity Model for Undrained Cyclic Behavior of Clays. I: Theory. *Journal Of Geotechnical Engineering*, *118*(2), 229-245. doi: 10.1061/(asce)0733-9410(1992)118:2(229).

Lings, M., Pennington, D., & Nash, D. (2000). Anisotropic stiffness parameters and their measurement in a stiff natural clay. *Géotechnique*, *50*(2), 109-125. doi: 10.1680/geot.2000.50.2.109.

Manzari, M., & Nour, M. (1997). On implicit integration of bounding surface plasticity models. *Computers & Structures*, *63*(3), 385-395. doi: 10.1016/s0045-7949(96)00373-2.

Mendoza, M. J., & Prince, J. (1986). "Preliminary report on the earthquake of September 19,1985, and its effects on structures and foundations in Mexico City." *Geotechnical News*, 4(1), 20-29.

Morimoto, R,, Nakamura, K., Tsuneishi, Y., Ossaka, J., & Tsunoda, N. (1967). "Landslides in the epicentral area of the Matsushiro earthquake swarm." *Bulletin of the Earthquake Research Institute* 45(2), 241-263.

Mortezaie, A., & Vucetic, M. (2013). Effect of Frequency and Vertical Stress on Cyclic Degradation and Pore Water Pressure in Clay in the NGI Simple Shear Device. *Journal Of Geotechnical And Geoenvironmental Engineering*, 139(10), 1727-1737. doi: 10.1061/(asce)gt.1943-5606.0000922

Mróz, Z. (1967). On the description of anisotropic workhardening. *Journal Of The Mechanics And Physics Of Solids*, 15(3), 163-175. doi: 10.1016/0022-5096(67)90030-0

Mroz, Z., Norris, V., & Zienkiewicz, O. (1978). An anisotropic hardening model for soils and its application to cyclic loading. *International Journal For Numerical And Analytical Methods In Geomechanics*, *2*(3), 203-221. doi: 10.1002/nag.1610020303

Ohara, S., & Matsuda, H. (1988). Study on the settlement of saturated clay layer induced by cyclic shear. *Soils And Foundations*, 28(3), 103-113. doi: 10.3208/sandf1972.28.3_103

Okur, D., & Ansal, A. (2007). Stiffness degradation of natural fine grained soils during cyclic loading. *Soil Dynamics And Earthquake Engineering*, *27*(9), 843-854. doi: 10.1016/j.soildyn.2007.01.005

Papadimitriou AG, Manzari MT, Dafalias YF. (2005).Calibration of a simple anisotropic plasticity model for soft clays. Proceedings, GeoFrontiers Conference of ASCE, January 24–26, Austin, TX, Geotechnical Special Publication 128, 415–424.

Prévost, J. (1977). Mathematical modelling of monotonic and cyclic undrained clay behaviour. *International Journal For Numerical And Analytical Methods In Geomechanics*, 1(2), 195-216. doi: 10.1002/nag.1610010206

Rouainia, M., & Muir wood, D. (2000). A kinematic hardening constitutive model for natural clays with loss of structure. *Géotechnique*, *50*(2), 153-164. doi: 10.1680/geot.2000.50.2.153

Roscoe, K.H. & Burland, J.B. (1968) On the generalised stress-strain behaviour of 'wet' clay, in: J. Heyman, F. Leckie (Eds.), Engineering plasticity, *Cambridge University Press*, Cambridge, 535-609

Roscoe, K. & Poorooshasb, H. (1963), 'A theoretical and experimental study of strains in triaxial compression tests on normally consolidated clays', *Geotechnique* **13**(1), 12-38.

Roscoe, K., Schofield, A. & Wroth, C. (1958), 'On the yielding of soils', *Geotechnique* **8**(1), 22-53.

Roscoe, K. H. & Schofield, A. N. (1963). Mechanical behaviour of an idealised 'wet' clay. Proc. 2nd *European Conference on Soil Mechanics*, Wiesbaden 1, pp. 47-54.

Schanz, T., Vermeer, P. A., & Bonnier, P. G. (1999). The hardening soil model: formulation and verification. *Beyond 2000 in computational geotechnics*, 281-296.

Seidalinov G., & Taiebat, M. (2013). Bounding surface SANICLAY plasticity model for cyclic clay behavior. *International Journal For Numerical And Analytical Methods In Geomechanics*, *38*(7), 702-724. doi: 10.1002/nag.2229

Seidalinov G. (2012). A simple anisotropic bounding surface plasticity model for cyclic response of clays, The University of British Columbia, Vancouver, Canada.

Wheeler, S., Näätänen, A., Karstunen, M., & Lojander, M. (2003). An anisotropic elastoplastic model for soft clays. *Canadian Geotechnical Journal*, *40*(2), 403-418. doi: 10.1139/t02-119.

Tafili.M & Triantafyllidis, Th. (2018). On constitutive modelling of anisotropic viscous and non-viscous soft soils. 9th *European Conference on Numerical Methods in Geotechnical Engineering*, Cardoso et al. (Eds). Taylor & Francis Group, London, ISBN 978-1-138-33198-3:481-486

Vermeer, P. A., & Neher, H. P. (1999). "A soft soil model that accounts for creep." *Proceedings of the International Symposium Beyond 2000 in Computational Geotechnics*: 10 years of PLAXIS International, Balkema, Rotterdam, Netherlands, 249–261.

Vucetic M, Dobry R. (1988) "Degradation of marine clays under cyclic loading". *Journal of Geotechnical Engineering*, ASCE, Vol.114, No.2, pp 133-149.

Vucetic, M., & Dobry, R. (1991). Effect of Soil Plasticity on Cyclic Response. *Journal Of Geotechnical Engineering*, 117(1), 89-107. doi: 10.1061/(asce)0733-9410(1991)117:1(89)

WebPlotDigitizer - Extract data from plots, images, and maps. (2019). Retrieved 4 September 2019, from https://automeris.io/WebPlotDigitizer/

Wichtmann T., & Triantafyllidis, T. (2018). Monotonic and cyclic tests on kaolin: a database for the development, calibration and verification of constitutive models for cohesive soils with focus to cyclic loading. *Acta Geotechnica*, 13(5), 1103–1128. https://doi.org/10.1007/s11440-017-0588-3

Wichtmann T., (2018) http://www.torsten-wichtmann.de/ Homepage.

Wilson, N., & Greenwood, J. (1974). Pore Pressures and Strains after Repeated Loading of Saturated Clay: *Canadian Geotechnical Journal*, 12(4), 545-546. doi: 10.1139/t75-066

Wood, D.M. (1991). Soil behaviour and critical state soil mechanics. Cambridge: Cambridge University press.

Yasuhara K, Hirao K, Hyde (1992). Effects of cyclic loading on undrained strength and compressibility of clay. *Soils and Foundations*;32(1):100e16.

Yu, H., Khong, C., & Wang, J. (2007). A unified plasticity model for cyclic behaviour of clay and sand. *Mechanics Research Communications*, *34*(2), 97-114. doi: 10.1016/j.mechrescom.2006.06.010

Zergoun, M., & Vaid, Y. (1994). Effective stress response of clay to undrained cyclic loading. *Canadian Geotechnical Journal*, 31(5), 714-727. doi: 10.1139/t94-083.

Zhou, J., & Gong, X. (2001). Strain degradation of saturated clay under cyclic loading. *Canadian Geotechnical Journal*, 38(1), 208-212. doi: 10.1139/cgj-38-1-208

Appendices

Appendix-I

Derivation of coefficients for computing the similarity ratio

The bounding surface equation of the Saniclay model is given by,

$$F=\left(\bar{q}-\bar{p}\alpha\right)^2-\left(N^2-\alpha^2\right)\bar{p}\left(p_0-\bar{p}\right)=0 \tag{1}$$

The corresponding equations of the image stress in terms of the current stress state (p,q), projection center (p_c,q_c) and the similarity ratio b is given by,

$$\bar{p}=\left(p_c+b\left(p-p_c\right)\right),\quad \bar{q}=q_c+b\left(q-q_c\right) \tag{2}$$

By substituting equation (2) in equation (1), the similarity ratio can be obtained.

$$F=\left(\bar{q}-\bar{p}\alpha\right)^2-\left(N^2-\alpha^2\right)\bar{p}\left(p_0-\bar{p}\right)=Ab^2+Bb+C \tag{3}$$

Foreseeing plenty of numerical quantities which might arrive by substituting the images stress equations into equation (3), it has been decided to solve the equation in parts to arrive at the solution easily. Considering the first part of equation (3),

$$\begin{aligned}\left(\bar{q}-\alpha\bar{p}\right)^2&=\bar{q}^2+\alpha^2\bar{p}^2-2\alpha\bar{q}\bar{p}\\&=A_1b^2+B_1b+C_1\end{aligned} \tag{4}$$

Now substituting equation (2) in equation (4) and sequentially expanding the quadratic equation gives the following flow of equations,

$$
\begin{aligned}
& \left(q_c + b\left(q - q_c\right)\right)^2 + \alpha^2\left(p_c + b\left(p - p_c\right)\right)^2 - 2\alpha\left(q_c + b\left(q - q_c\right)\right)\left(p_c + b\left(p - p_c\right)\right) \\
\Rightarrow \quad & q_c{}^2 + b^2\left(q - q_c\right)^2 + 2bq_c\left(q - q_c\right) \\
& + \alpha^2 p_c{}^2 + \alpha^2 b^2\left(p - p_c\right)^2 + 2\alpha^2 b p_c\left(p - p_c\right) \\
& - 2\alpha q_c p_c - 2\alpha b^2\left(q - q_c\right)\left(p - p_c\right) - 2\alpha b\left(p_c\left(q - q_c\right) + q_c\left(p - p_c\right)\right) \\
\Rightarrow \quad & q_c{}^2 + \alpha^2 p_c{}^2 - 2\alpha q_c p_c \\
& + b^2\left(\left(q - q_c\right)^2 + \alpha^2\left(p - p_c\right)^2 - 2\alpha\left(q - q_c\right)\left(p - p_c\right)\right) \\
& + 2b\left(q_c\left(q - q_c\right) + \alpha^2 p_c\left(p - p_c\right) - \alpha\left(p_c\left(q - q_c\right) + q_c\left(p - p_c\right)\right)\right) \\
\Rightarrow \quad & \left(q_c - \alpha p_c\right)^2 + b^2\left(\left(q - q_c\right) - \alpha\left(p - p_c\right)\right)^2 \\
& + 2b\left(\left(q - q_c\right)\left(q_c - \alpha p_c\right) - \alpha\left(p - p_c\right)\left(q_c - \alpha p_c\right)\right) \\
\Rightarrow \quad & \left(q_c - \alpha p_c\right)^2 + b^2\left(\left(q - q_c\right) - \alpha\left(p - p_c\right)\right)^2 \\
& + 2b\left(\left(q - \alpha p\right) - \left(q_c - \alpha p_c\right)\right)\left(q_c - \alpha p_c\right)
\end{aligned}
$$

Which gives the coefficients of 'b' in the quadratic equation in (4) as follows,

$$
\begin{aligned}
A_1 &= \left(\left(q - q_c\right) - \alpha\left(p - p_c\right)\right)^2 \\
B_1 &= 2\left(\left(q - \alpha p\right) - \left(q_c - \alpha p_c\right)\right)\left(q_c - \alpha p_c\right) \\
C_1 &= \left(q_c - \alpha p_c\right)^2
\end{aligned}
\tag{5}
$$

Now considering the second part of equation (3),

$$
\begin{aligned}
-\bar{p}\left(p_0 - \bar{p}\right) &= \bar{p}^2 - \bar{p}p_0 \\
&= A_c b^2 + B_2 b + C_2
\end{aligned}
\tag{6}
$$

Following the similar procedure as in case of the first part of the equation (3) here by substituting equation (2) in equation (6) gives rise to,

$$
\begin{aligned}
& \left(p_c + b\left(p - p_c\right)\right)^2 - \left(p_c + b\left(p - p_c\right)\right)p_0 \\
\Rightarrow \quad & p_c{}^2 + b^2\left(p - p_c\right)^2 + 2bp_c\left(p - p_c\right) - p_c p_0 - bp_0\left(p - p_c\right) \\
\Rightarrow \quad & b^2\left(p - p_c\right)^2 + b\left(2p_c\left(p - p_c\right) - p_0\left(p - p_c\right)\right) + p_c{}^2 - p_0 p_c
\end{aligned}
$$

Now the coefficients of 'b' in the quadratic equation (6) are given by,

$$
\begin{aligned}
A_2 &= \left(p - p_c\right)^2 \\
B_2 &= \left(2p_c\left(p - p_c\right) - p_0\left(p - p_c\right)\right) \\
C_2 &= p_c\left(p_c - p_0\right)
\end{aligned}
\tag{7}
$$

Combining equations (4), (5), (6) and (7) and substituting in equation (3) gives the coefficients of the quadratic equation containing the similarity ratio ‘b’ as follows,

$$A = \frac{A_1}{\left(N^2 - \alpha^2\right)} + A_2$$
$$B = \frac{B_1}{\left(N^2 - \alpha^2\right)} + B_2 \qquad (8)$$
$$C = \frac{C_1}{\left(N^2 - \alpha^2\right)} + C_2$$

Appendix-II

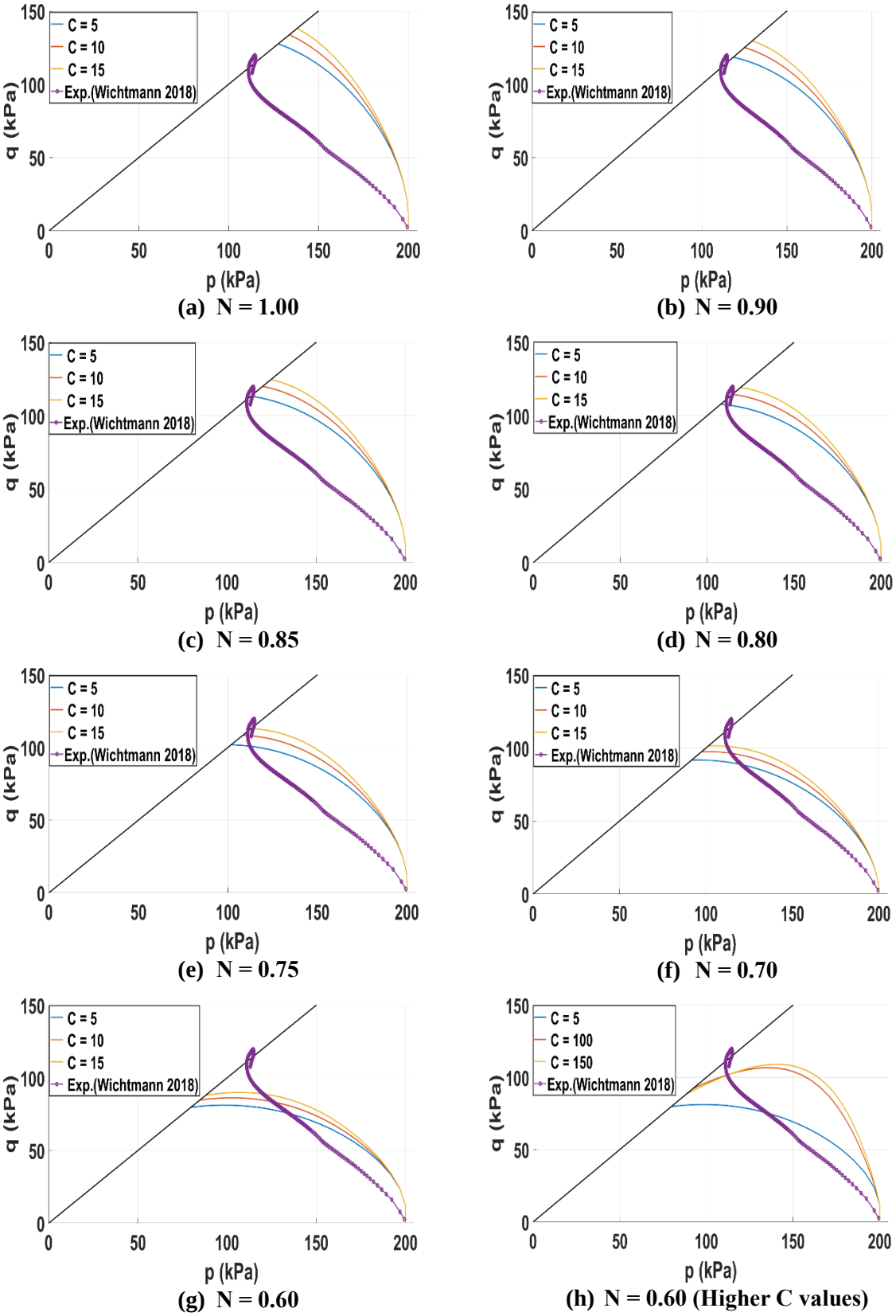

Figure 0.1 : Calibration of N and C parameters based on the stress path data from experiments.

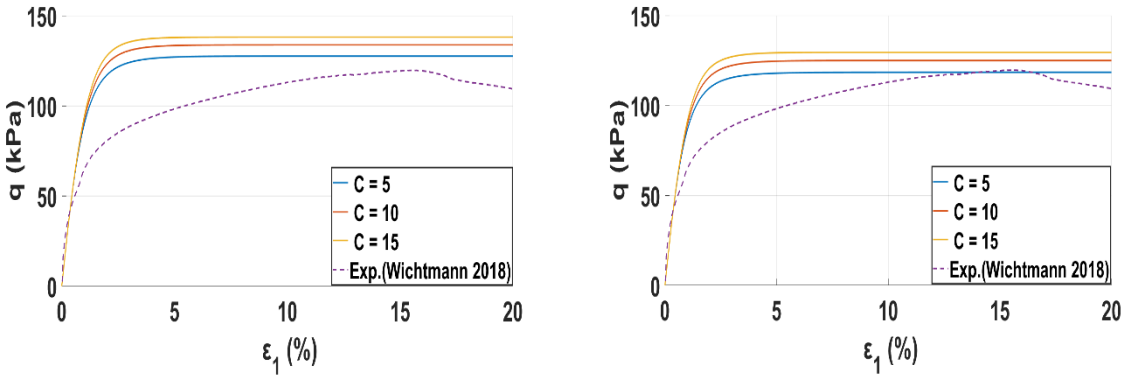

(a) N = 1.00 (b) N = 0.90

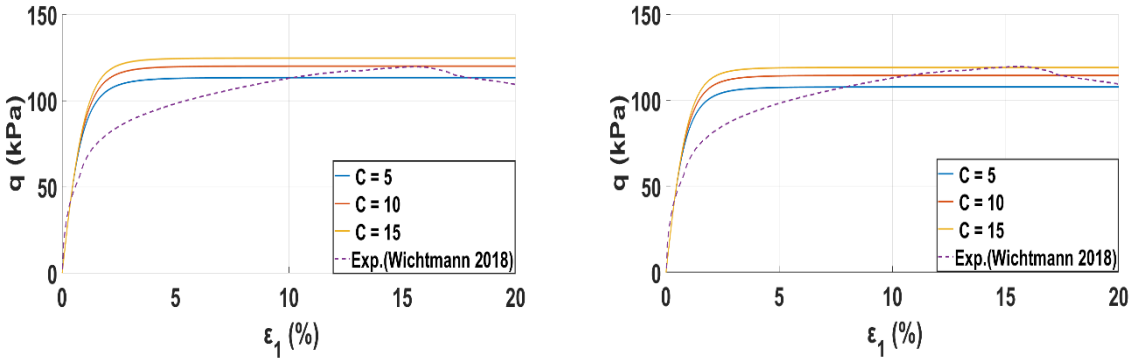

(c) N = 0.85 (d) N = 0.80

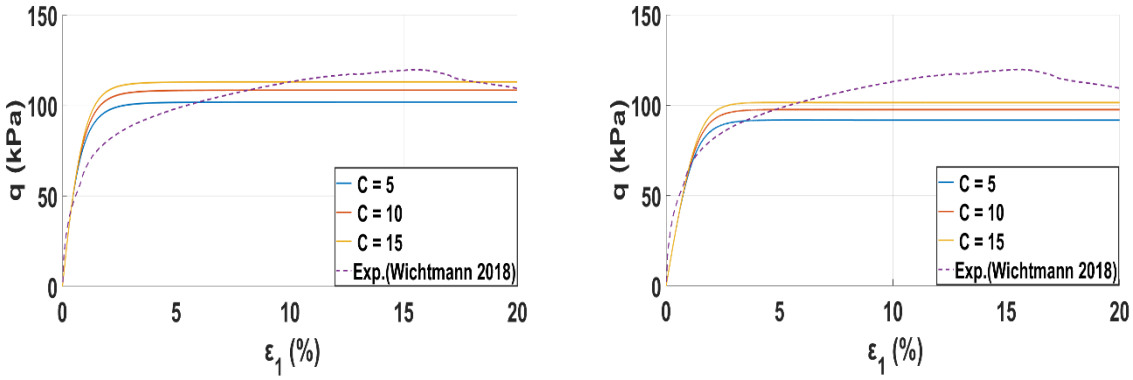

(e) N = 0.75 (f) N = 0.70

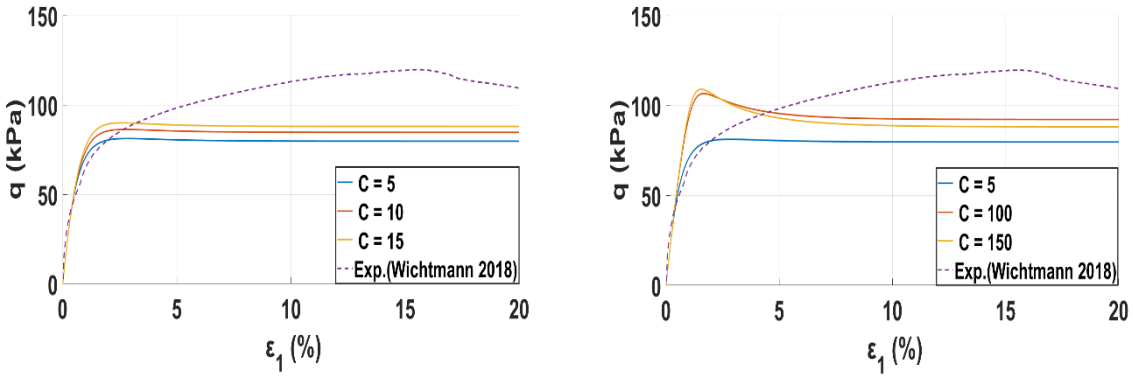

(g) N = 0.60 (h) N = 0.60 (Higher C values)

Figure 0.2 : Calibration of N and C parameters based on the stress-strain response from experiments (Wichtmann 2018).

Appendix-III

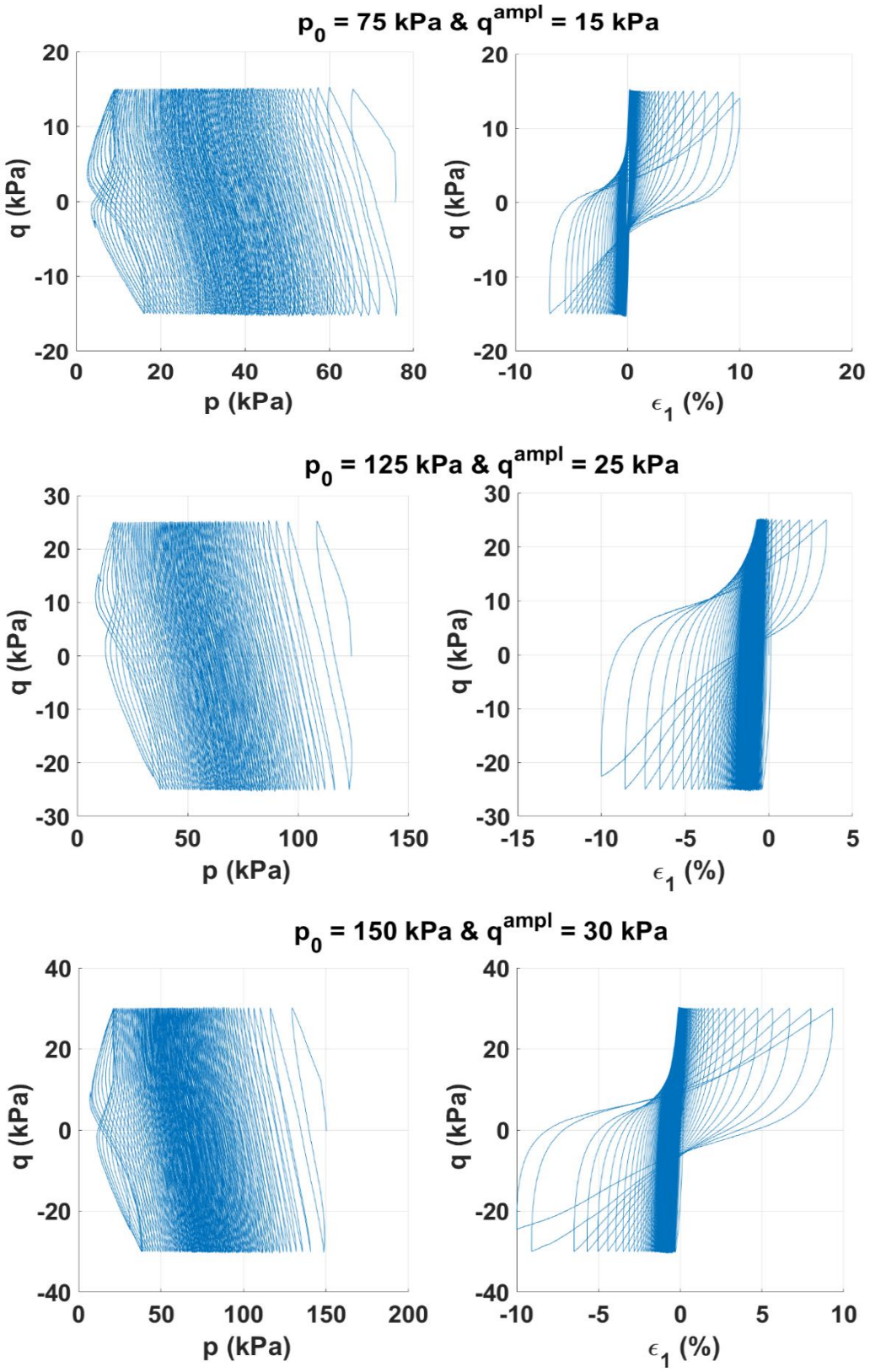

Figure 0.3 : Experimental results with variation of the initial pressure from Wichtmann (2018)

Appendix-IV

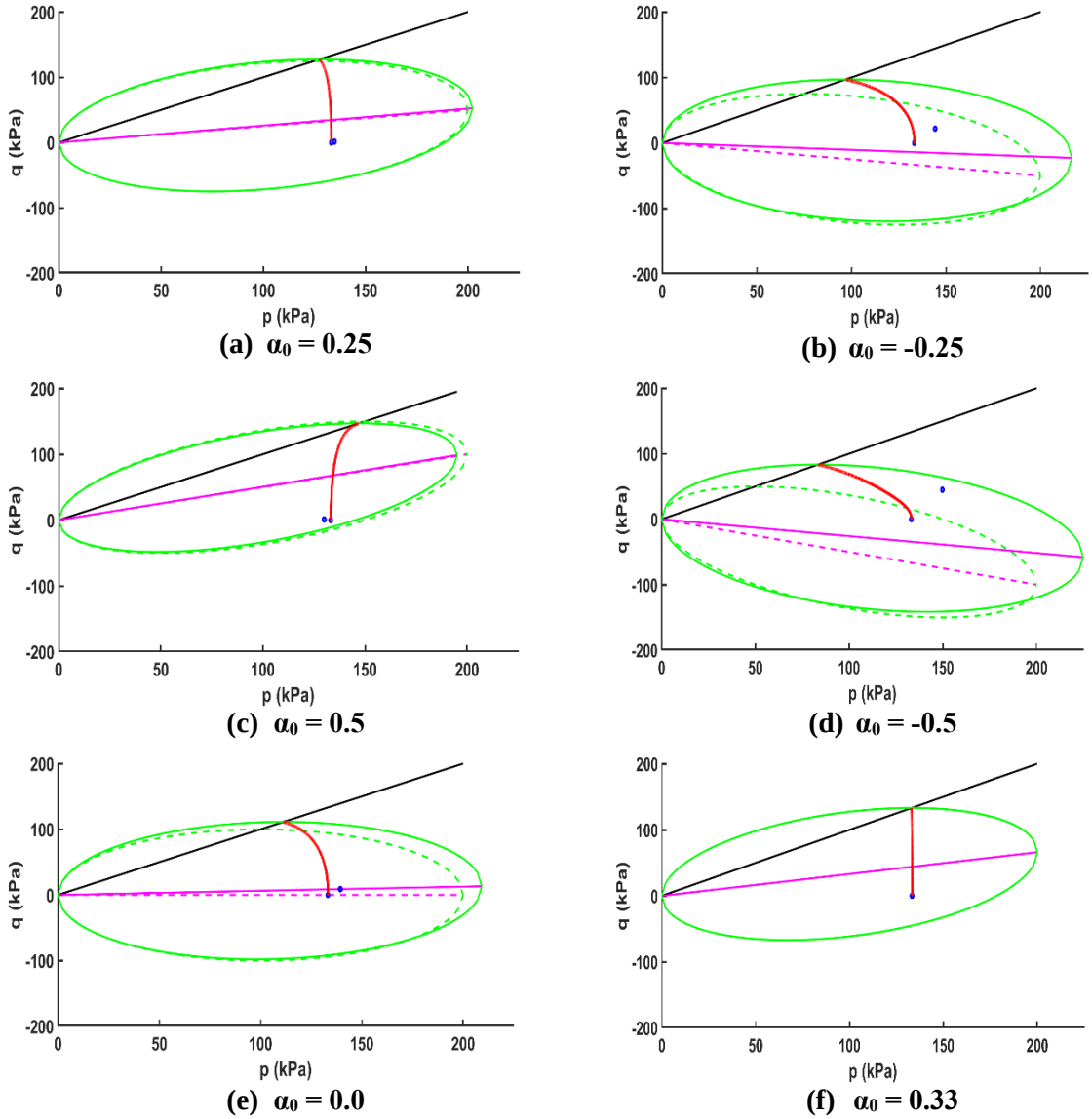

Figure 0.4 : Rotation of the bounding surface with evolution of the stress path. (dotted lines are indicative of the initial position, green surface is the bounding surface, magenta lines are the rotational hardening lines)